MESOSCALE INVESTIGATION OF CONSTITUTIVE BEHAVIOUR OF HCP METALS BASED ON FULL-FIELD IN SITU STRAIN MEASUREMENT

by

NIMA ŞAFAK

M.S., Mechanical Engineering, Boğaziçi University, 2013

Submitted to the Institute for Graduate Studies in
Science and Engineering in partial fulfillment of
the requirements for the degree of
Doctor of Philosophy

Graduate Program in Mechanical Engineering
Boğaziçi University

2023

ACKNOWLEDGEMENTS

I would like to express my sincere gratitude to my advisor Assoc. Prof. C. Can Aydıner for the invaluable support during my Ph.D. study and related research, for his patience, motivation, and immense knowledge. His guidance and constructive feedback have shaped the direction of this research and strengthened my academic growth. I could not have imagined having a better advisor and mentor for my Ph.D. study.

I am also grateful to Prof. Kutay Orakçal, Assoc. Prof. C. Ercan Gürses, Prof. Erdem Alaca, Assist. Prof. Sertan Alkan and Dr. Mustafa Umut Özcan for their insightful comments and encouragement, but also for the vital guidance which incent me to widen my research from various perspectives.

My sincere thanks also go to my colleagues at Mechanics of Advanced Material laboratory at Boğaziçi University. It was a great pleasure to work, collaborate, discuss, and share with a group of talented and enthusiastic researchers.

I extend my appreciation to my friends for their unwavering support, encouragement, and understanding throughout this journey. Their belief in me and their willingness to listen and provide assistance have been a constant source of motivation.

I would like to dedicate this thesis to special people, my beloved mother, my wonderful father, my benevolent sister, my supporting brother and, to the love of my life, Shirin. With your non-ending support, you have made me stronger and better than I could have ever imagined. I love you to the moon and back.

This work is partially supported by the Scientific and Technological Research Council of Turkey, TÜBİTAK, Grant No:114M215.

ABSTRACT

MESOSCALE INVESTIGATION OF CONSTITUTIVE BEHAVIOUR OF HCP METALS BASED ON FULL-FIELD IN SITU STRAIN MEASUREMENT

Hexagonal close-packed (HCP) metals have received extensive attention from research and industrial communities for their exceptional properties. Among these HCP metals, Magnesium is the lightest and the most intriguing one. Its deformation incorporates significant twinning that depends heavily on microstructure and loading conditions. For this study, a common Mg alloy (AZ31) is considered with multiple crystallographic textures to aid the fundamental understanding of its deformation. This is predominantly an experimental effort with a novel in-situ digital image correlation (DIC) technique that provides deformation quantification with granular resolution over macroscopic fields. Further, samples are subjected to cyclic to study spatial aspects of strain accommodation via twinning, detwinning and slip plasticity. Shear band formation and progression due to the bursts of twins is quantitatively detailed and it is demonstrated that unlike twinning, detwinning is a nearly homogeneous phenomenon. Further tension after detwinning forces the material to plasticity. Another load reversal to compression pushes the material back into twinning regime but with reduced shear band compactness. It is also shown that the Lüders-like bands form with lower strain content in extruded samples compared to rolled samples that also show extreme plastic anisotropy. An open source spatially-resolved crystal plasticity solver (DAMASK) is used to test the fidelity level of basic constitutive models when confronted with twin coordination and detwinning. Two sets of representative volume elements (RVEs) are produced for both textures. In both cases, the simulated plastic deformation occurs earlier with considerable hardening at the twin plateau deviating from the near perfectly-plastic experimental results. The model is found to be incapable of predicting the strain compactness and intense anisotropy of the rolled sample shear bands. It is also not geared to model detwinning, highlighting the need for more advanced models if the goal is to attain high fidelity in micro-scale fields.

ÖZET

HSP METALLERİN BÜNYE DAVRANIŞININ TAM SAHA YERİNDE GERİNİM ÖLÇÜMLERİYLE ARA ÖLÇEK İNCELEMESİ

Hegzagonel sıkı paket yapı (HSP) metaller, olağandışı özellikleri nedeniyle araştırma ve endüstri topluluklarından geniş çaplı ilgi görmektedir. HSP metaller arasında, Magnezyum en hafif ve en ilginç olanıdır. Magnezyumun deformasyonunda, mikroyapı ve yükleme koşullarına ağır bağımlılık gösteren ikizlenme mekanizması önemli ölçüde rol alır. Bu çalışmada, malzeme davranışının temel bir anlatımına ulaşmak üzere farklı mikroyapılarda elde edilebilen yaygın bir Magnezyum alaşımı (AZ31) seçilmiş. Bunun için, makroskobik alanlarda kristal çözünürlüğü sağlayan ileri bir dijital imge korelasyonu (DIC) tekniği ile yük altında veri toplanmıştır ve tezin en önemli bilimsel katkıları deneyseldir. Deneylerde hem haddelenmiş hem ekstrüzyonlu numuneler döngüsel yüke tabi tutulmuştur. Çok taneli yapı üzerinde yayılan eşgüdümlü şekil değiştirme desenleri ara ölçekte yüksek çözünürlüklü imge korelasyonu ile ortaya konmaktadır. Basma altında biribirini tetikleyen ani ikizlenme yayılımının oluşturduğu kayma bantları ve bunların ilerlemesi tartışılmış ve ikizlenmenin aksine, ikizlenme tersiniminin neredeyse homojen bir şekilde gerçekleştiği gösterilmiştir. Çekme yükü daha da arttırldığında ise kayma mekanizmaları devreye girmektedir. Numune tekrar basıldığındaysa ikizlenme bantları, sıkılıkları önemli ölçüde azalarak, geri gelmiştir. Tekstür karşılaştırmasında, ekstrüzyonlu numunede haddelenmiş numuneye göre Lüders bantlarının daha düşük gerinim içeriği ile oluştuğu ortaya konmaktadır. Tezde, ikizlenme koordinasyonu ve ikiz tersinimi olgularının basit kristal akma modelleri tarafından ne seviyede öngörülebildiğini incelemek için açık kaynaklı bir çok taneli yapı yazılımı (DAMASK) ele alınmıştır. Numuneler için ikizlenme rejimindeki akma, deneysel sonuçlarda görünen pekleşmesiz eğriden saparak önemli bir pekleşme ile daha erken meydana gelmektedir. Modelin, haddelenmiş numundeki kayma bandı oluşumunu ve her iki mikroyapıda da ikiz tersinimi tahmin etmek için yetersiz olduğu görülmüştür. Dolayısıyla Magnezyum alaşımlarında şekil değiştirmesini gerçekçi bir şekilde öngörmek için daha ileri modeller gerektiği ortaya konmuştur.

TABLE OF CONTENTS

ACKNOWLEDGEMENTS iii
ABSTRACT iv
ÖZET v
LIST OF FIGURES vii
LIST OF TABLES xiv
LIST OF SYMBOLS xv
LIST OF ACRONYMS / ABBREVIATIONS xvi
1. INTRODUCTION 1
1.1. Motivation 1
1.2. Objectives and Scope 2
1.3. Thesis Outline 4
2. BACKGROUND AND LITERATURE REVIEW 6
2.1. HCP Deformation 6
2.2. Multi-Scale DIC Studies Over HCPs 8
2.3. Crystal Plasticity Investigations of Hcps 10
3. MATERIALS AND METHODS 13
3.1. Sample Preparation 13
3.2. Experimental Setup 16
3.3. DIC Implementation 18
3.4. CPFE Implementation 21
4. RESULTS AND DISCUSSION 30
4.1. Experimental Results 30
4.2. Numerical Results 65
4.3. Experiment-Model Comparison 70s
5. CONCLUSION 80
6. FUTURE WORKS 82
REFERENCES 83
APPENDIX 96

LIST OF FIGURES

Figure 2.1. Basal, prismatic, pyramidal <a>, 1st and 2nd order pyramidal <c+a>, tensile and compressive twin deformation micromechanism depicted on Mg HCP crystal. The slip/twin plane crosses the atoms colored in blue. The corresponding slip mechanisms and its propagation direction is shown by yellow solid line and a black arrow respectively. 7

Figure 3.1. Sketch of the Mg AZ31 specimen with 3x3 mm^2 gage cross-section (a), definition of different surfaces and sample coordinate system for rolled (b) and extruded (c) samples; the primary micro-DIC measurement is conducted on the top surface while macro-DIC is conducted on both top and side surfaces. 14

Figure 3.2. Reconstructed pole figure of rolled (a) and extruded (b) bulk Mg AZ31. . 15

Figure 3.3. Illustration of raw bulk sample form after wrought processes; extrusion (a) and rolling (b). HCP unit cell re-orientation due to these wrought processes and its projection on pole figure sphere for (c) extrusion; transversely distributed HCP crystals around ED and (d) rolling processes; alignment of HCP crystals c-axis with normal direction of the bulk plate. 15

Figure 3.4. Elements of the measurement setup. 17

Figure 3.5. Macro-DIC images of sample. (a) top surface in focus, (b) side surface in focus over the 45° mirror. 18

Figure 3.6. Depiction of the micro-DIC area scan with one of the 5 Megapixel frames exemplified in the full-field for rolled (a) and extruded (b) samples. 19

Figure 4.1. Engineering stress-strain curve of the compression-tension-compression cycle obtained using the finely-spaced macro-DIC data. Load points that correspond to micro-DIC area-scans are indicated with letters. 31

Figure 4.2. (a-j) Macro-DIC axial strain maps for top and side surfaces, presented side by side for load points a-j shown on Figure 4.1. An aid for 3-D visualization is provided for point a. 32

Figure 4.3. Combination micro-DIC maps for axial strain at load points a-j 33

Figure 4.4. Combination micro-DIC maps for in plane strain components (ε_{xx}, ε_{yy}, ε_{xy}) and infinitesimal rotation (ω_{xy}) for (a) point β, (b) point f, and (c) point i. 35

Figure 4.5. Kinematic depiction of simple shear in the x-y plane in terms of infinitesimal strain and rotation components (ω_{xy}) for (a) ±45°compressive and (b) ± θ tensile structures in conjunction with the utilized blue (−), red (+) colorbar. The colors of the sheared elements pertain to ω_{xy}. 36

Figure 4.6. Incremental strain/rotation maps that single out deformation from (a) point g to h, (b) point h to i, (c) from point f to g (for only axial strain); (d) binary map of chosen points for the second-wave tensile twin driven bands in stage $h - i$ (part b). Part (c) contains a sketch of the considered increments over the cycle. 37

Figure 4.7. Axial strain histograms (a) at the two points (d, i) where strain averages are nominally null, (b) at points f, g, h, i. 38

Figure 4.8. Selected-area SEM micrographs in the first twin plateau with (a) 800x, and (b). 40

Figure 4.9. Incremental strain maps for stages a-β and β - χ. b Strain histograms for points a, β,χ,b in the overall field, c exclusively over the band populations. d Histograms of the second wave h-i stage bands put in perspective of the first wave bands at point β, (e) Histograms that depict strain recovery over stage c-d. 41

Figure 4.10. Zoom-in map of infinitesimal rotation inside a rectangular region of interest (a) over stage h-i (rectangle indicated on Figure 4.6), (b) at point h, (c) at point f. The contour plot is overlaid over the combined micrographs. 44

Figure 4.11. (a) Macro-DIC and (b) combination micro-DIC axial strain maps at $\varepsilon_{yy} \cong$ -0.5%. A 150x150 $\mu m2$ region is zoomed in to show the crystalline scale resolution of the micro-DIC map at effective strains of (c) $\varepsilon_{yy} \cong 0.5\%$, (e) $\varepsilon_{yy} \cong 1.2\%$, and (f) $\varepsilon_{yy} \cong 2\%$. The strain contours are shown with a level of transparency of the reference image of this locality whose bare form is provided in (d). 49

Figure 4.12. (a-l) Micro-DIC combination axial strain maps for load points a-l marked on the stress-strain curve on the bottom right. 51

Figure 4.13. Standard deviation of transverse and axial strains ($\delta\varepsilon_{xx}$, $\delta\varepsilon_{yy}$) derived from full-field combination micro-DIC maps plotted against the average axial strain ε_{yy} 53

Figure 4.14. (l-q) Micro-DIC combination axial strain maps for load points l-q marked on the stress-strain curve. Comparative axial strain histograms for pints l and q are provided on the left-top where f stands for percent frequency.... 55

Figure 4.15. Micrographs of a small (70x70 μm^2) region of interest at (a) the reference(undeformed) state, (b) point h at the end of the twin plateau, (c) point l at the end of detwinning. The most obvious twin contrast that

formed at point h is marked with arrows. Some other traces are marked with triangles. All these traces disappear in part (c). 56

Figure 4.16. For the extruded sample of the study, combination micro-DIC strain maps for (a) point a (full-field average -0.42%), (b) point b (-0.59%), (c) strains accommodated in the a-b interval. 59

Figure 4.17. For the complementary rolled sample, combination micro-DIC strain maps for (a) point a, (b) point b, (c) strains accommodated in the a-b interval. Macroscopic strains for both points and the stress level of the twin plateau are shown on the right. 59

Figure 4.18. Incremental strain maps over the first twin plateau that describe strain accommodation between load points (a) c and d, (b) d and e, (c) e and f, (d) f and g, (e) g and h. See Figure 4.12 for the location of these points on the stress-strain curve as well as their absolute strain maps. 60

Figure 4.19. Unit cells that sketch the major elements of (a) rolling, and (b) extrusion textures. The operative (highest resolved shear) 10121011 tensile twin system pair is indicated in each unit cell. Note twinning is unipolar and these systems only operate under compressive stress (σ) along (a) RD and (b) ED. This σ-sense is indicated with arrows in the illustrations. 61

Figure 4.20. (a,b) For the extruded material of the study (a) ε_{yy} and (b) ε_{xx} histograms for load interval a-b, and load points c, f, and h over the twin plateau. The data population belongs to the material points in the band expansion zone in Figure 4.16(c). (c,d) The limiting histograms in part (a) put in perspective of the rolled-material characteristic histogram in twin-driven bands (see Figure 4.17). 64

Figure 4.21. Orientation maps of the prepared representative spectral analysis volume (rolled texture) in terms of the cosine of the angle between crystal c-axis

[0001] and (a) x-axis (ND), (b) y-axis (TD), (c) z-axis (RD). A value of 1 means alignment and 0 means orthogonality. 67

Figure 4.22. DAMASK results: Stress-strain curve for rolled RVE subjected to 2% compression along z-direction (RD) and measured over (TD). 68

Figure 4.23. DAMASK analysis for rolled RVE and axial stress σ_{zz}. maps at macroscopic strains of (a) -0.8, (b) -1.2, (c) -1.6, (d) -2%. 68

Figure 4.24. Orientation maps of the prepared representative spectral analysis volume (extruded texture) in terms of the cosine of the angle between crystal c-axis [0001] and (a) x-axis (ND), (b) y-axis (TD), (c) z-axis (RD). A value of 1 means alignment and 0 means orthogonality..... 69

Figure 4.25. DAMASK results: Stress-strain curve for extruded RVE subjected to 2% compression along z-direction (RD) and measured over (TD). 69

Figure 4.26. DAMASK analysis: extruded RVE and axial stress σ_{zz}. maps at macroscopic strains of (a) -0.8, (b) -1.2, (c) -1.6, (d) -2%. 70

Figure 4.27. DAMASK analysis: effective Poisson's ratio for rolled RVE. (a) ν_{xz}, and (b) ν_{yz}..... 71

Figure 4.28. DAMASK analysis: effective Poisson's ratio for extruded RVE. (a) ν_{xz}, and (b) ν_{yz}. 72

Figure 4.29. DAMASK results: (a) twin shear activity per twin mechanism and (b) accumulative twin shear for rolled RVE. 72

Figure 4.30. DAMASK results: (a) twin shear activity per twin mechanism and (b) accumulative twin shear for extruded RVE. 73

Figure 4.31. DAMASK results: $\varepsilon_{xx}$and ε_{zz} strain histograms at macroscopic strains of (a) Rolled and (b) Extruded RVEs at ε_{zz} = 0.8,1.2, 1.6 and -2%. 73

Figure 4.32. DAMASK results: (a) tensile twin and (b) basal slip resistance at $\varepsilon_{zz} =$ 2% average strain compared to the (c) accumulated strain in rolled RVE. 74

Figure 4.33. DAMASK results: (a) tensile twin and (b) basal slip resistance at ε_{zz}= 2% average strain compared to the (c) accumulated strain in extruded RVE. . 74

Figure 4.34. Twin shear per tensile twin variants for rolled RVE at ε_{zz} = 2% strain. (a) 11011102, (b) 10111012, (c) 01110112, (d) 11011102, (e) 10111102, (f) 01110112, (g) accumulated shear by all tensile twin variants, (h) strain map ε_{zz}..... 75

Figure 4.35. Twin shear per tensile twin variants for extruded RVE at ε_{zz} = 2% strain. (a) 11011102, (b) 10111012, (c) 01110112, (d) 11011102, (e) 10111102, (f) 01110112, (g) accumulated shear by all tensile twin variants, (h) strain map ε_{zz}..... 76

Figure 4.36. Experimentally constructed stress-strain curve compared to numerical estimation: (a) rolled RVE simulation predicts higher stress level compared to experimental result and (b) extruded RVE simulation underpredicts stress level. 76

Figure 4.37. Experimental and numerical comparison of C-T-C stress strain curves for rolled (a) and extruded (b) samples. Tensile twin shear activity per variant under cyclic load for rolled (c) and extruded (d) RVEs. Total twin shear for rolled (e) and extruded (b) RVEs. 77

Figure A.1. Determination of DAMASK coordinate system (correlation of DAMASK coordinate directions compared to HCP crystal axes for ideal rolled texture with all crystals c-axis || ND). 97

Figure A.2. (a) Configuration file example and (b) loadcase definition for 2% compression along y direction. 98

Figure A.3. Parameter sensitivity study on ideal rolled texture under cyclic load..... 99

Figure A.4. Scripts used to create configuration file, run the simulation and post-process the results. 100

Figure A.5. Creating IPF results in DAMASK. Results are visualized in ParaViwe... 101

LIST OF TABLES

Table 4.1. Average transverse and axial strains (ε_{zz} , ε_{yy}), apparent Poisson's ratio ($\nu = -\varepsilon_{xx}/\varepsilon_{yy}$), standard deviations of transverse and axial strains ($\delta\varepsilon_{xx}$, $\delta\varepsilon_{yy}$) derived from the full micro-DIC combination fields for load points a-l in Figure 4.12. 53

Table 4.2. Average transverse and axial strains (ε_{xx} , ε_{yy}), apparent Poisson's ratio ($\nu = -\varepsilon_{xx}/\varepsilon_{yy}$), standard deviations of transverse and axial strains ($\delta\varepsilon_{xx}$, $\delta\varepsilon_{yy}$) derived from the full micro-DIC combination fields for load points l-q. All strain quantities shown in percentages. 55

Table 4.3. Elastic and plastic parameters implemented in constitutive equations in section 3.4 for modeling HCP Mg. data are obtained from [28]..... 66

Table 4.4. Slip and twin variants included in numerical simulation. 66

LIST OF SYMBOLS

C	Stiffness tensor
f	Twin volume fraction
F	Deformation Gradient
$\mathcal{H}$	Heaviside function
h_0	Initial hardening parameter
h_∞	Upper bound for hardening parameter
L	Velocity gradient
n	Normal plane vector
N_g	Number of microstructural constituents
P	First Piola-Kirchhoff stress
S	Second Piola-Kirchhoff stress
sgn	Sign function
s	Slip direction vector
u	Displacement in x direction
v	Displacement in y direction
γ	Shear
$\dot{\gamma}$	Rate of shear
δ	Standard deviation
ε	Strain
ξ_{sl}	Slip resistance
ξ_{tw}	twin resistance
ν	Poison's ratio
ρ	Density
σ	Cauchy stress
τ	Shear stress
ϕ	Orientation angle in Bunge notation
ω	Rotation component of strain

LIST OF ACRONYMS / ABBREVIATIONS

2D	Two dimensional
3D	Three dimensional
CAD	Computer-Aided Design
CCD	Charge-Coupled Device
CCW	Counterclockwise
CPFE	Crystal Plasticity Finite Elements
CRSS	Critical Resolved Shear Stress
C-T-C	Compression-Tension-Compression
CTW	Contraction Twinning
CW	Clockwise
DAMASK	Düsseldorf Advanced Material Simulation Kit
DIC	Digital Image Correlation
DRX	Dynamic recrystallization
DTW	Double Twinning
EBSD	Electron Backscatter Diffraction
ED	Extrusion Direction
EDM	Electrical Discharge Machining
FDM	Finite Difference Method
FEA	Finite Element Analysis
FE-CP	Finite Element Crystal Plasticity
FEM	Finite Element Method
FFT	Fast Fourier Transform
FVM	Finite Volume Method
FW-TTD	First Wave Tensile Twin Driven
GRIM	Grain Interaction Model
HCP	Hexagonal Close-Packed
MD	Molecular Dynamics
Mg	Magnesium
ND	Normal Direction

ODF	Orientation Distribution Function
PDE	Partial Differential Equation
RD	Rolling Direction
ROI	Region of Interest
RVE	Representative Volume Element
SEM	Scanning Electron Microscope
SM-CP	Spectral Method Crystal Plasticity
SMDIC	Scanning Microscopic DIC
SW-TTD	Second Wave Tensile Twin Driven
TD	Transverse Direction
TTD	Tensile Twin Driven
VPSC	Visco-Plastic Self Consistent

1. INTRODUCTION

1.1. Motivation

Hexagonal close-packed (HCP) metals like Titanium, Magnesium and Zirconium find significant utilization in engineering. The particular niche of Titanium and Magnesium alloys is high specific strength in structural applications. While Titanium alloys are well established and heavily utilized in e.g., aerospace industry, Magnesium alloys present heavier challenges (a more idiosyncratic HCP deformation that includes a heavy realization of the peculiar mechanical twinning phenomenon) and are thus chosen as the model materials considered in this thesis.

Magnesium alloys are in fact the lightest structural metals ($\rho \sim 1.7\ g/cm^3$), approximately two-thirds that of aluminum and one-quarter that of steel. This makes them a very attractive material class for applications where weight reduction is critical, such as in the aerospace and automotive industries [1]. With the high strength to weight ratio of magnesium, this metal is widely used in the manufacturing of electronic devices, medical equipment, and power tools [2]. Showing excellent thermal conductivity, this material is also used where heat dissipation is the case such as heat sinks and electronic components. Finally, magnesium is an environmentally friendly metallic material, that is, without any degradation in its original properties, magnesium could be recycled for later applications.

With all the excellent properties mentioned, magnesium alloys are the subject of an intense, multi-scale research activity, driven by the demand to increase their engineering utility. A significant aspect of effort is to meet the challenges posed by the complicated mechanical behavior and sharp plastic anisotropy of the hexagonal-close-packed Magnesium crystal. This is typified by large differences among the activation ease of its slip systems (basal, prismatic, pyramidal) and profuse activity of deformation twinning (especially the $10\bar{1}2$ tensile twin) [3,4]. The unipolar activity of the latter leads to load-path dependence in mechanical behavior [5], an effect that is particularly severe for wrought Magnesium components that possess sharp crystallographic textures [6]. Notably, both

rolled and extruded materials exhibit heavy tension-compression asymmetry that manifests in the sigmoidal shape of the *cyclic* stress-strain curves [5], [7-9].

1.2. Objectives and Scope

With the variety and complexity of micromechanical constituents, universally-valid predictions of Magnesium behavior uniquely demand micromechanical approaches that construct the mechanical behavior of the polycrystalline aggregate from its constituents. The intricacy of these modeling efforts (both mean-field [4],[10] and full-field [11–13]) have increased in time, particularly regarding the implementation of twinning and detwinning. Currently, some of the latest full-field simulations target high fidelity reproduction of strain distributions at the local (inter/intra-granular) length-scales [11],[14], rather than the traditional goal of meeting the aggregate average. The complementary advance in experimental mechanics that can potentially validate/calibrate local predictions has been the development of spatially-resolved strain measurement at microstructural scales [15–19]. Independent of the model-validation aspect, these measurements also provide an incisive look at the damage formation in these materials since material damage is innately linked to the degree and nature of strain localization in the measured distributions.

While a degree of strain localization is intrinsic to the crystallite-scale deformation of any polycrystalline aggregate [20], Magnesium alloys are also prone to exhibit the more distinct and challenging material behavior that progresses strain heterogeneity to the macroscopic scale: the spatially-coordinated propagation of local strains [15]. This is especially prominent on the load paths where deformation twinning is dominant and autocatalytic twinning [21,22](crudely, twinning in one crystallite triggering twinning in its neighbor) operates as the spatial coordination mechanism. With the clustered advances of twinning events, the overall size of the resulting *Lüders-like* [22,23] bands approach the millimeter scale in this regime.

Hence, the broad lines of these bands can be detected with the ordinary resolution of macroscopic DIC (macro-DIC) [24],[27]. Macro-DIC fields, however, can essentially be regarded as a moving average over crystallite-scale strain fields, and obviously, the quantitative specifics of crystallite-scale strain distributions are lost. More concretely,

whether a particular macro-DIC value pertains to spatially frequent localization structures with intermediate micro-strains or spatially-sparse structures with severe micro-strains is not known, though the physical implications of the two are very different. If, on the contrary, microscopy is used to properly characterize the local strains, the outlook on the overall advance of the bands is typically sacrificed, due to the usual compromise between spatial resolution and field coverage.

In the experimental wing of this thesis, a quantitative investigation of the local strain fields with subgranular resolution while maintaining sample-scale coverage is conducted via a novel, large-field scanning microscopic DIC method (coined "SMDIC" here). The method is applied to both rolled and extruded Magnesium AZ31 samples, which is the fundamental material parametrization in this thesis. Kapan et al. [25] have previously shown that extrusion texture entails milder twin-propagation-based localization in comparison to the rolled at macro-DIC strain resolution. As carefully noted, however, macroscopic fields do not identify the quantitative/spatial specifics of the underlying intergranular localization meshes.) A full-field coverage (typically encompassing on the order of 10^5 grains) depict the intergranular strain networks with immense statistical significance, while also keeping track of the macroscopic twin-propagation bands in the entire field for both samples. Two more outstanding features of the applied technique are particularly critical value for investigating Magnesium deformation, namely, in-situ measurement and load application over a non-monotonic path. Thus, the described full-field strain mapping has been repeated at closely-spaced load points, first detailing the progression of the Lüders-like bands. This coincides with applying compression in the rolled/extrusion directions (RD/ED) to stimulate profuse twinning. Then the load is reversed to tension, stimulating, and monitoring the recovery of the strains that were incurred over the twin plateau and then introducing a measure of remnant plasticity. Finally, the spatial features of strain accommodation over a second twin plateau are considered by compressing the sample after this history.

To sum up the experimental (and the dominant) wing of this thesis, Magnesium deformation is analyzed in extreme detail (with microscopic resolution and macroscopic coverage to lay out strain networks) for two microstructures (rolled and extrusion texture) and over a cyclic loading path that is designed to focus on twinning and detwinning

phenomena as well as slip plasticity elements that are activated in the load sense twinning is unfavorable.

From the modeling standpoint, the thesis will consider the results from a well-known crystal plasticity package called DAMASK (Düsseldorf Advanced Material Simulation Kit [28] that has a Magnesium material class with constitutive behavior composed of the combined operation of slip and twin mechanisms. DAMASK implements spatially resolved analysis (with RVEs containing realistic grain neighborhoods) but uses a spectral method (rather than finite elements) to achieve considerable time savings in the analysis. Thus, DAMASK has been a reasonable choice for conducting analysis without the need for high performance computing. Here, we will test the adequacy of DAMASK Magnesium simulations (comparing its results with the grain-scale DIC data) for both textures and over the non-monotonic (reversed) load paths.

1.3. Thesis Outline

The background and main literature elements of this thesis are provided in Section 2. This section starts with the basics of HCP deformation and continues with a broad review of experimental techniques that are used to elucidate it. Then, the specialized literature on multiscale DIC studies on HCPs are provided 2.2. Finally, numerical studies with crystal plasticity constitutive models for HCP materials are considered in Section 2.3.

The methodology (experimental and numerical) is described in Section 3. Details of sample preparation (for rolled and extruded samples) and the setup used for experimental investigations are provided in Sections 3.1 and 3.2 respectively. Details of the specific high-resolution DIC implementation is discussed in section 3.3. Here, in addition to the basic DIC algorithm, the area scanning implementation and post-processing tools to identify deformation (i.e., strain localization) features over the full field is described. Details of the crystal plasticity spectral analysis approach that is implemented in this thesis for a numerical comparison with the DIC data are reviewed in Section 3.4.

Experimental and numerical results for rolled and extruded samples are reported in Sections 4.1 and 4.2, respectively. They are then compared in Section 4.3 to present the

fidelity/adequacy level of DAMASK predictions against actual material fields. Conclusion is provided in Section 5, followed by future work statement in Section 6.

2. BACKGROUND AND LITERATURE REVIEW

2.1. HCP Deformation

2.1.1. Micro-Mechanisms of HCP Deformation

Various slip systems are responsible to provide at least five independent deformation mechanisms needed for plastic deformation in ductile material. In general, basal <a> slip is reported as the easiest deformation mechanism in Mg alloys due to the lowest critical resolved shear stress among deformation mechanisms. Together with prismatic slip <a>, the minimum requirement of plastic deformation in HCP crystal is not fully satisfied [4],[29,30]. More specifically, when deformation along c-axis of Mg crystal is forced, slip systems are unable to yield enough dislocation, triggering the activation of unipolar tensile twin; retaining second lowest CRSS [4],[29-32]. When basal <a> and tensile twin become saturated or are not favored, harder mechanisms such as prismatic <a> slip, pyramidal <c+a> slip, $\{10\bar{1}1\}$ contraction twinning (CTW), $\{10\bar{1}1\}$ – $\{10\bar{1}2\}$ double twinning (DTW), grain boundary shear or sliding modes become alternatively operational [33],[35]. Most relevant deformation micromechanisms in Mg are illustrated in Figure 2.1.

2.1.2. Mechanical Twinning

Mechanical twinning refers to the formation of twin boundaries, where a region of the material undergoes a shear deformation to change its crystallographic orientation with respect to the surrounding material. Twinning is initiated by the motion of partial dislocations on specific crystallographic planes and in specific directions. This leads to the formation of a twin boundary, which separates the parent and twinned regions. The twin boundary is characterized by a mirror reflection of the crystal lattice across the boundary plane. Mechanical twinning involves a shear deformation along the twinning plane and direction accommodating plastic strain in the material, leading to increased ductility.

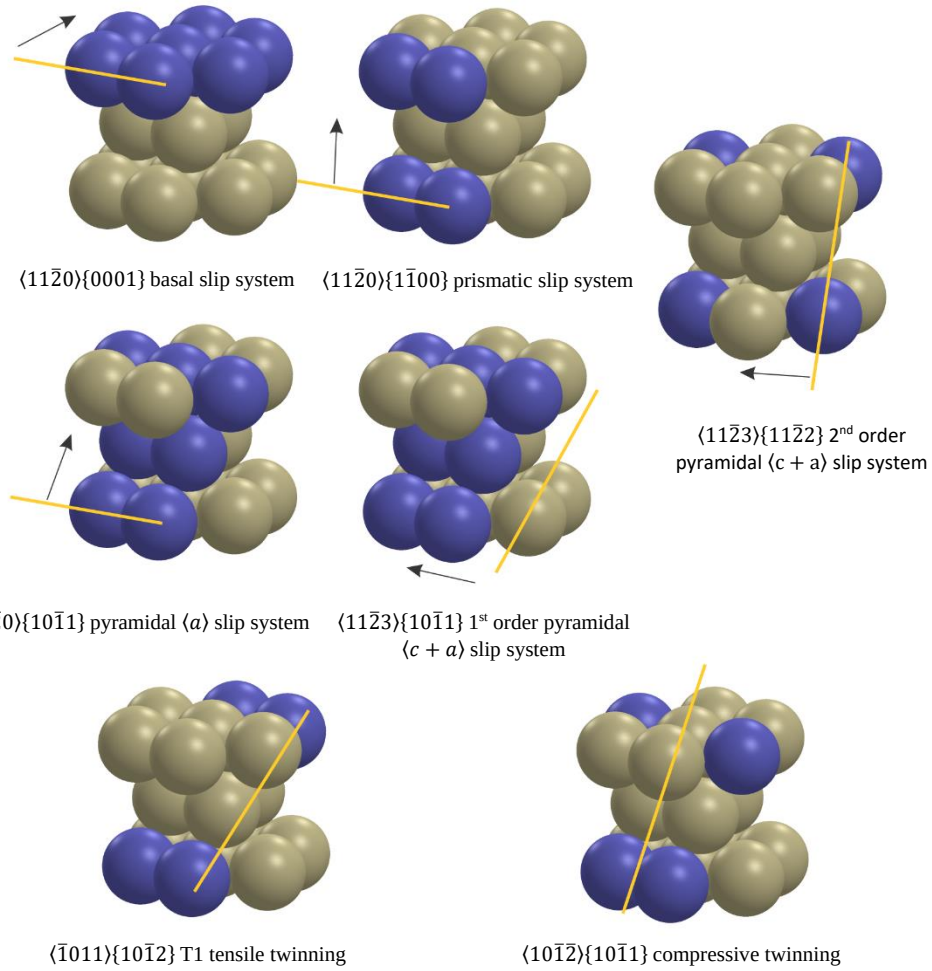

Figure 2.1. Basal, prismatic, pyramidal <a>, 1st and 2nd order pyramidal <c+a>, tensile and compressive twin deformation micromechanism depicted on Mg HCP crystal. The slip/twin plane crosses the atoms colored in blue. The corresponding slip mechanisms and its propagation direction is shown by yellow solid line and a black arrow respectively.

The mechanical twinning in magnesium is influenced by various factors, including temperature, strain rate, crystallographic orientation, and presence of alloying elements. These factors affect the propensity and extent of twinning, as well as the resulting mechanical properties of the material. Understanding and controlling the mechanical twinning behavior in magnesium is of great interest in the field of materials science and engineering, as it can impact the design and performance of magnesium-based alloys in various applications.

Wrought Magnesium exhibits extreme plastic anisotropy and load path dependence [5,6], [36,37] due to a combination of sharp crystallographic textures [38], vast differences among activation ease of slip/twin micromechanisms [39,40] and profuse activity of the tensile twin [30]. In cyclic loading of both extruded and rolled materials, the stress-strain behavior shows notable asymmetry since the unipolar tensile twin dominates strain accommodation only in one sense of the load [7],[36,37],[41-43],[45].

2.1.3. Experimental Investigations on HCP Deformation

The micromechanisms (basal, prism, pyramidal slip systems; tensile and compressive twins) show various levels of activity that is specific to each crystallographic texture and load path [32],[35],[45,46]. These levels have been commonly quantified by training polycrystal models with volume-averaged experimental results [e.g., average strains [10],[39],[47], stress-strain gradient [48], anisotropy ratio [49,50], orientation-resolved bulk diffraction [4],[31,32],[51-56] that by-definition discount the spatial distribution of strain. Among the experimental studies that are utilizing different measurement methods, several are directing the spatial coordination of twin EBSD [12],[22],[57-60] while the others benefit from Diffraction (neutron and x-ray) [31],[57], [61,62], acoustic emission [63] or microscopy [64] techniques.

2.2. Multi-Scale DIC Studies Over HCPs

Accounting for the heterogeneity in microstructural strain accommodation, however, bears fundamental significance for the mechanical behavior of polycrystals. First, there is the obvious connection between strain localization and material failure noted for Magnesium alloys over monotonic [19], [65-67] and cyclic load paths [37], [68-69]. Second, higher-fidelity models that can represent distributions are necessary for advancing our predictive ability. These factors motivated an intense research activity on the measurement of local strain fields, with digital image correlation (DIC) as the predominant technique [20]. For Magnesium alloys, there are numerous recent DIC studies, spanning multiple length-scales macroscopic [24], [26-27], [70], optical microscopy [15-16], electron microscopy [17-19], [71-72]. The implementation with optical microscopy (coarse intra-granular resolution for typical grain size and magnification) is well-suited to study the crystallite interactions with

statistical significance. In particular, when the field coverage is extended by area-scanning, a comprehensive ability to characterize the hierarchical organization of the intergranular strain networks is attained. This version of the technique (abbreviated “SMDIC” here—scanning microscopic DIC) can map strains over 10^3-10^6 grains of typical sizes (5-50 μm).

Applying compression in the rolling direction (RD) of a Magnesium AZ31 plate, Aydıner and Telemez [15] utilize SMDIC to show the coordination of few-grain-long bands in a ±45° pattern that further organize into sample-scale shear bands [25,26]. These bands form due to the autocatalytic [21], spatially-coordinated activity of the tensile twin and hereby called the tensile-twin-driven (TTD) bands. Moreover, their study resolves the abrupt stages of the TTD-band progression, owing to the development of an adaptive focusing procedure that allows stepwise in-situ measurement (rare among microscopic DIC efforts that are typically confined to the ex-situ measurement of a single deformation stage.) Recently, in-situ SMDIC has been applied over the opposite (RD-tension) load path as well [16], where the profuse tensile twin activity is suppressed. In this case, the strain fields show another species of shear bands, distinguished with angles that significantly deviate from 45° (“non-45° bands”). These localization bands present limited propagation and rather intensify statically around some micro-texture channels [73-74].

Assuming a level of homogeneity (in their constitutive forms, input morphology and/or interaction) that is not realized by the material, typical polycrystal models for Magnesium overlook the dominant, long-range microstructural strain localization patterns that are presented in these two studies. While aggregate-average predictions are useful, low fidelity at the meso-scale is clearly detrimental to the universality of the models, and more importantly, precludes a more analytical assessment of the damage formation in these materials.

The deficiency in our understanding of the strain localization patterns that underlie the Magnesium deformation, strongly motivates the question of how such structures form and evolve along cyclic load paths, in pertinence to cyclic damage. The problem draws further significance from complementing the extensive literature on the severely-asymmetric cyclic deformation behavior of Magnesium [5], [26], [55], [61], [75-76]. Here, we apply SMDIC over a compression-tension-compression (C-T-C) cycle in RD and ED and, to our

knowledge, report the first full-field, crystallite-resolution strain measurements over a cyclic load path in these materials. Notably, the in-situ quality of the SMDIC measurement gains further prominence, allowing detailing the transitions between the different deformation regimes. While the formation of strain localization patterns in their associated load directions (i.e., TTD bands in compression and non-45° bands in tension) is anticipated, the more critical point of the measurement over the cyclic load path is to show the latent effects of these structures on one another. The study, in particular, investigates the formation of remnant strain heterogeneity that stems from such *historical* interactions.

2.3. Crystal Plasticity Investigations of Hcps

Material modelling is the process of using mathematical and computational techniques to predict the properties and behavior of materials under different conditions. Some of the modelling approaches are: i) Molecular Dynamics (MD) that simulates the motion of individual atoms or molecules in a material and be used to study the behavior of materials at the atomic scale and to predict properties such as mechanical strength, thermal conductivity, and electrical conductivity. ii) Continuum Mechanics that models materials as continuous media, using mathematical equations to describe the behavior of the material. Continuum mechanics can be used to study the behavior of materials under different loading conditions and to predict properties such as stress and strain. iii) Ab initio methods that are quantum mechanical methods and can predict the properties of materials based on the fundamental principles of quantum mechanics. Ab initio methods are used to study the behavior of materials at the atomic scale and can be used to predict properties such as electronic structure, bonding energies, and reaction pathways. iv) Phase-field methods that are numerical techniques with the capability of modelling the evolution of microstructures in materials, such as the growth of grains or the formation of cracks [76,77].

Crystal plasticity modelling is a continuum approach [28], [79] that describes the deformation behavior by treating the material as a continuous medium even though its structure is composed of individual grains or crystals. Crystal plasticity modelling uses a set of equations to describe the relationship between the stress and strain tensors of a crystalline material. These equations take into account the crystal structure and orientation, the interactions between individual crystals, and the effects of defects and dislocations on the

material's mechanical behavior. These models typically incorporate concepts from continuum mechanics, such as stress and strain tensors, and the physics of micromechanisms within crystals. Activity of these micromechanisms, hence their contribution to the plastic deformation under external load is incorporated to the model by considering Schmid tensors. In crystal plasticity, a slip system is a set of planes and directions within a crystal that are most susceptible to plastic deformation under a given external load. The Schmid tensor for a particular slip system represents the direction of the maximum resolved shear stress on the slip plane, which is the direction of greatest deformation. The Schmid tensor can be expressed mathematically as a second-order tensor, which is a matrix that represents the relationship between two vectors. The Schmid tensor for a slip system is a function of the crystallographic orientation of the crystal and the orientation of the external load or stress. It is used to calculate the resolved shear stress on the slip plane, which is the component of the external load that contributes to plastic deformation.

Each crystal plasticity model has its own characteristics and level of complexity. In some approaches, the deformation behavior of a polycrystalline material is described by a single representative crystal or grain, and the constitutive equations are formulated in terms of the orientation of this crystal. The deformation behavior of the other grains is assumed to be similar to that of the representative grain, but with some statistical variations due to differences in orientation and microstructure. The Taylor (deformation of a polycrystalline material can be described as the sum of the deformation of its individual grains) and Sachs (deformation of a polycrystalline material is controlled by the deformation of a single grain) models are examples of these approaches to crystal plasticity. In other approaches on the other hand, the deformation behavior of a polycrystalline material is described by multiple representative crystals or grains, and the constitutive equations are formulated in terms of the orientation of each of these crystals. These approaches consider the variability in orientation and microstructure across the polycrystal e.g., Finite Element Crystal Plasticity (FE-CP), Grain Interaction Model (GRIM), Spectral Method-based Crystal Plasticity (SM-CP). Crystal plasticity modelling can be formulated in all these approaches, and the choice of approach depends on the specific application and the level of accuracy required for the analysis.

Most polycrystal simulations, while admitting crystallite-scale inputs (e.g., the activation criteria of micromechanisms) only target to capture the aggregate-average mechanical response. Clearly, most mean-field models are limited to this task though the advances in the treatment of deformation twinning [45], [59], [80] and stochastic approaches to represent aggregate statistics [81,82] should be duly noted. Faithfully representing the strain fields at a microstructural length-scale, however, is a fundamental outcome that is expected of the new physics-based models of polycrystals to attain (i) improved universality of the predictions over different textures and load paths thanks to the higher physical fidelity, and (ii) predictive ability on crucial local phenomena like damage and failure that are tied to the observed strain localization [14]. The bare requirements of this effort are to apply spatially-resolved full-field models [6, 18, 68] to realistic grain neighborhoods [11-14], [83], and to pose a constitutive model that is consistent with a target length-scale. As for this target, the meso-scale bears practical significance. First, it is the next scale to ensure physical fidelity coming down from the macro-scale. Second, it is the scale where the typical kinematic constructions of crystal plasticity (e.g., plastic strain tensor taken as a linear combination of micromechanism Schmid tensors) pose viable representations. (These constructions entail a homogenization of individual deformation agents inside the crystallite and are not fit to resolve them.) Combined with the fact that ascertaining the physical authenticity of a model at a certain length-scale requires experimental data at the same scale, the generic function of the current effort can be stated: rigorously guiding the new-generation polycrystal models toward meso-scale fidelity with novel experimentation that amplifies the information content with largescale scanning and in-situ measurement.

3. MATERIALS AND METHODS

3.1. Sample Preparation

Two sample sets of alternative crystallographic identity of commercial Mg are prepared for investigations in this thesis. The first set is extracted from hot-rolled magnesium AZ31 (3% Aluminium- 1% Zirconium) plate purchased from Alfa-Aesar Germany[1]. Second set is cut along the extrusion direction of an extruded Mg AZ31 bar (d=20mm) provided by Xi'an Yuchen China. To avoid potential variations of material properties in radial direction due to extrusion process, samples are cut at the center plane of the as-received bar. Wire electrical discharge machining (wire-EDM) is preferred to achieve acceptable cutting surface quality.

Samples are designed according to testing equipment spacious limitations with attention to grant enough measurement surface and resistance to buckling during the compression. Buckling resistance is confirmed by modelling the real-size specimen in Abaqus under compression. The final nominal dimensions in defined coordinate system (Figure 3.1) are ~8 mm (gage length) in rolling direction (RD)/extrusion direction (ED), with a 3x3 mm^2 cross section (after grinding and polishing). Figure 3.1 shows CAD sketch of specimen as well as relevant definitions used in this thesis e.g., coordinate system, surfaces etc.

To identify the crystallographic texture, both sets are probed by X-ray diffraction and pole figure data are collected by a Panalytix X-pert pro MDB four-circle diffractometer. The raw data is translated into pole figures in Matlab Mtex package. Discrete pole figures as well as calculated ODFs are shown in Figure 3.2 for both crystallographic textures.

For rolled sample, the pole figure (Figure 3.2-a) shows a concentrated distribution of basal (001) planes along the ND. Alternatively, for extruded sample, (001) planes are

[1] Stock No: 44915, Lot No: F29W008

symmetrically distributed about ED and orthogonal to it (Figure 3.2-b). Figure 3.3, aids the understanding wrought process directions and how pole figure sphere is aligned accordingly.

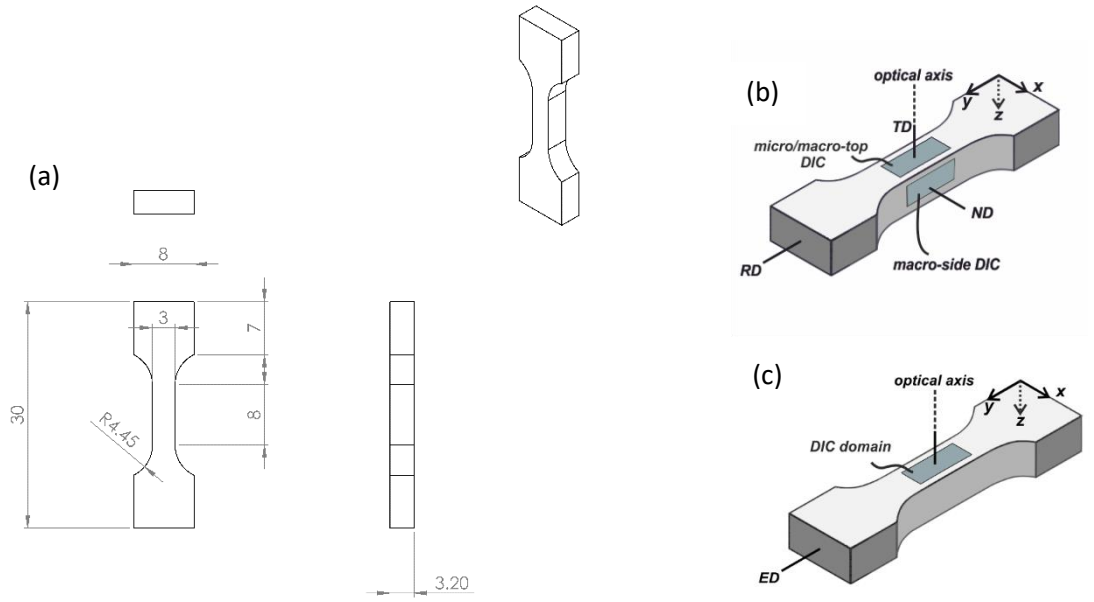

Figure 3.1. Sketch of the Mg AZ31 specimen with 3x3 mm^2 gage cross-section (a), definition of different surfaces and sample coordinate system for rolled (b) and extruded (c) samples; the primary micro-DIC measurement is conducted on the top surface while macro-DIC is conducted on both top and side surfaces.

Samples are cut from raw material by EDM, have fine but inadequate surface quality for measurement method used in this study (Digital Image Correlation: DIC). Additionally, to have a neat interpretation of deformation field over the measurement surface, crystallographic information should be addressed. Hence, a careful process of metallography is utilized to achieve fine-polished surfaces with grain boundary information. This process comprises of coarse-to-fine grinding of sample's x-y surface beginning with P400 grinding paper down to final step by 50 nm colloidal silica polishing solution. Polished surface is etched in a picric acid solution (picric acid: 0.65 gr, 99% Pure ethanol: 15 ml, acetic acid, and distilled water: 1.5 ml each).

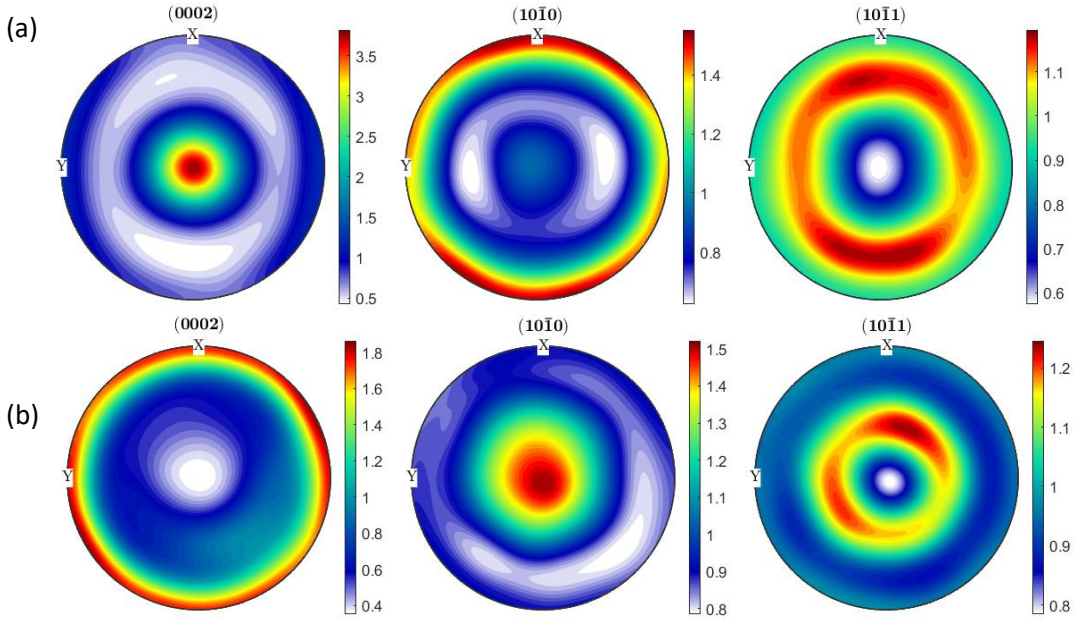

Figure 3.2. Reconstructed pole figure of rolled (a) and extruded (b) bulk Mg AZ31.

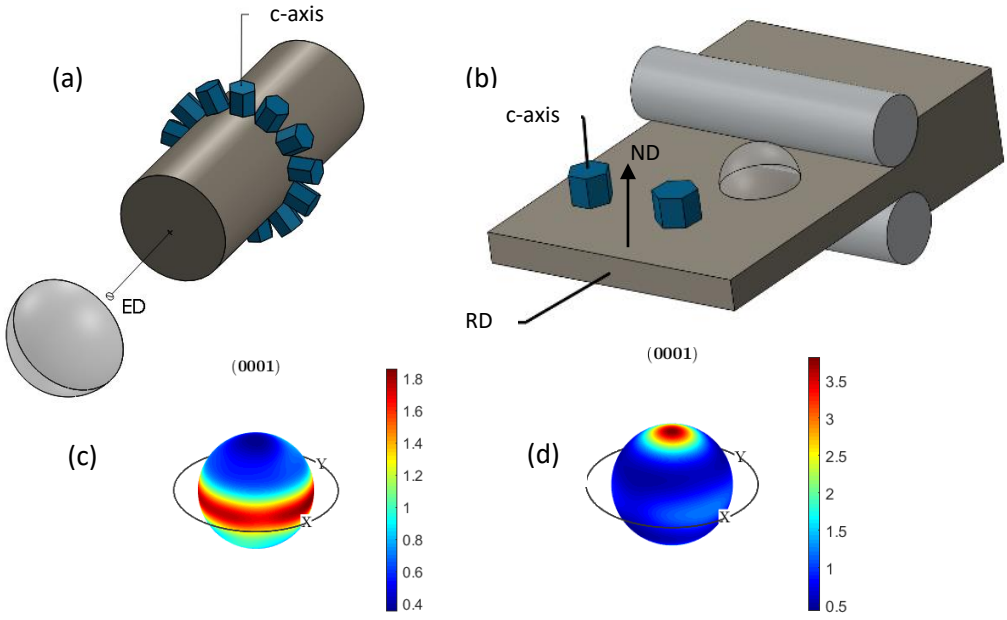

Figure 3.3. Illustration of raw bulk sample form after wrought processes; extrusion (a) and rolling (b). HCP unit cell re-orientation due to these wrought processes and its projection on pole figure sphere for (c) extrusion; transversely distributed HCP crystals around ED and (d) rolling processes; alignment of HCP crystals c-axis with normal direction of the bulk plate.

Specimens are initially fixed in a d=30 mm mount solution before surface metallography. The etched surface is covered by a protective layer, then the specimen is dismounted by resolving the mount material inside acetone. To facilitate demounting, the process is carried out in a thermo-acoustic vibration device. The drawback of this method is that remnants of mount material persist on the specimen and in some case acetone and mount solution penetrate under the protection layer deteriorating the surface quality. To overcome the issue, specimens are mounted with a thin aluminum film around it. Thus, can be separated from mount material easily and efficiently with no need for solvent most of the time. The nominal grain size is measured over micrograph images with lineal intercept method: 11 μm for rolled sample and 14.5 μm for extruded.

3.2. Experimental Setup

To prepare samples for DIC measurements, a fine speckled pattern is applied by spraying black matt paint using an Iwata Custom-B air brush over the x-y plane of both sample sets. Painting is carefully done to preserve clarity of grain boundaries while ensures sufficient inter-grain DIC pattern (applied paint together with surfaces' metallographic features). Side surface is also coated with thin layer of matt white paint overlayed by black speckled pattern in scale of Macro-DIC.

To conduct the experiments, dogbone specimens are fixed in a tensile rig (Kammrath&Weiss) with maximum 10KN load capacity which is a screw-driven mechanism operated by control unit. The load frame itself is assembled on a positioning stage with 3 translational degrees of freedom (x, y, z) which is controlled by computer to address any 3D position in space inside its ranges. Figure 3.4 shows the test setup schematically.

Two optical lines are installed on a rigid bar over the load frame to conduct both Macro and Micro-DIC. For rolled specimens and in both optical lines, images are captured by two 2452 × 2054-pixel Sony ICX625 monochrome CCD detectors. Macro-DIC camera is equipped with an Edmund Optics 0.5x telecentric lens while the line used for micro measurements benefits from a Navitar Ultrazoom 6000 tube fitted with a long working distance (34 mm) Mitutoyo M Plan Apo 10x objective. These combinations result in 0.199

μm/pixel resolution with a 487x408 μm^2 images for micro-DIC setup and 6.8 μm/pixel resolution for Macro-DIC. Later, to conduct experiments on extruded samples, cameras are update to AVT Pike F505B with a 5-megapixel monochrome detector. The resulting field of view for the updated setup is 434 x 364 μm^2 with the optical resolution of 0.177 μm/pixel. The whole setup is installed on a NewPort isolation vibration table to minimize the effect of ambient vibrations.

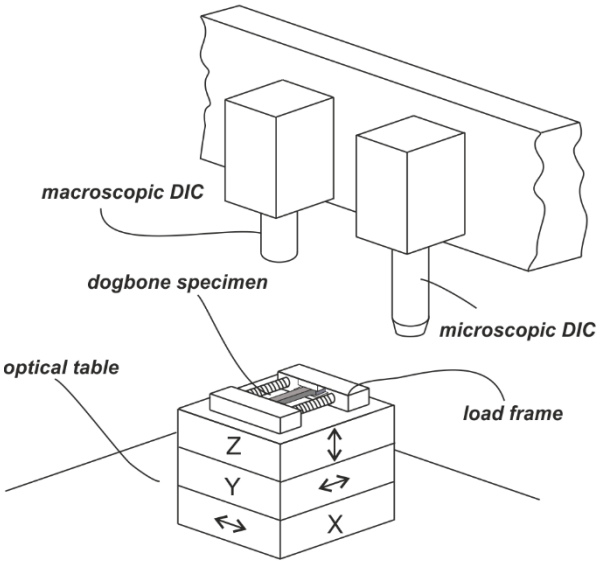

Figure 3.4. Elements of the measurement setup.

The experiment process is controlled by an in-house python code. Load is applied in position-controlled fashion. The loading scenario is designed to cover a full cycle starting with compression and followed by tension and second compression consequently (C-T-C). Fine load increments (0.05% average strain) provided a well-controlled experiment progression. For the undeformed stage at the beginning and then at each successive load points, the specimen is initially placed under macro-DIC optical line in its focal length to capture the image of top surface. Then, z position is changed in a way that the projection of side face on a mirror placed 45° to optical axis in TD-ND (x-z) plane gets in focus and image is captured. Figure 3.5 depicts examples of macro-DIC images; in-focus surfaces are marked with an asterisk.

Macro-DIC images are used to quickly calculate the accumulated average strain over the gage length and aid to construct the stress-strain curve simultaneously at each load point. Subsequently, the stage moves under micro-DIC optical line and matrices of 16x6 overlapping frames for rolled, 16x7 for extruded sample are scanned covering an area of 5.1 x 2.5 mm^2 and 5.1 x 2.8 mm^2, respectively. Before recording the image at each (x, y) and to ensure in-focus image acquisition, an automatized focusing process is performed along z-axis. Several images are taken at a discrete interval and the image with the highest contrast is saved as the final image. The continuity of scanned area is assured by ~400-pixels overlaps in both x and y directions.

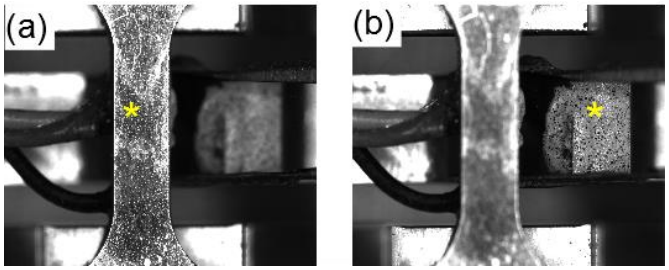

Figure 3.5. Macro-DIC images of sample. (a) top surface in focus, (b) side surface in focus over the 45° mirror.

3.3. DIC Implementation

3.3.1. Basic DIC Algorithm

Digital Image Correlation (DIC) is a non-contacting, non-destructive optical measurement technique that utilizes surface features- usually grayscale random pattern intensity- to calculate deformation over that surface. DIC algorithm compares the subsets between the reference and deformed images to determine their displacements. The algorithm searches for the best match of the subset in the deformed image by comparing the intensity patterns or image features. Various correlation algorithms, such as cross-correlation or pixel intensity-based methods, can be employed to find the best match and the displacement gradients at each measurement point is derived. Strain tensor is then calculated with central difference differentiation of displacement field. It should be noted that small strain formulation is used throughout this thesis. The small strain formulation is expressed as

$$\varepsilon_{xx} = \frac{\partial u}{\partial x}\ ,\ \varepsilon_{yy} = \frac{\partial v}{\partial y}\ ,\ \varepsilon_{xy} = \frac{1}{2}\left(\frac{\partial u}{\partial y} + \frac{\partial v}{\partial x}\right)\ ,\ \omega_{xy} = \frac{1}{2}\left(\frac{\partial u}{\partial y} - \frac{\partial v}{\partial x}\right). \qquad (3.1)$$

3.3.2. Area-Scanning Implementation

The images that are taken during micro-DIC scanning process are stitched together to form a 320/440 Megapixels (rolled/extruded) full-field image containing an overall grain population on the order of 10^5. Details of scanned area are schematically illustrated in Figure 3.6 with example images from both samples.

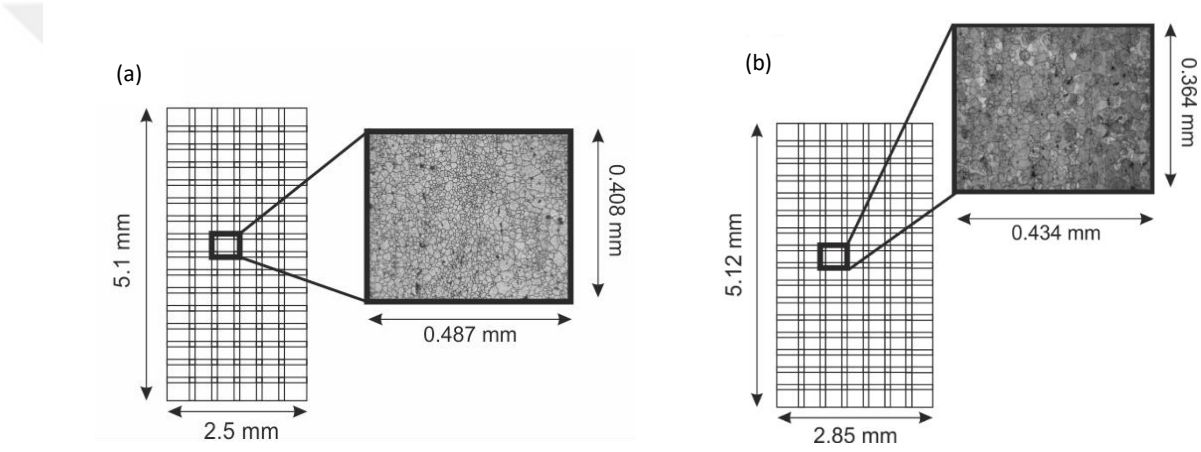

Figure 3.6. Depiction of the micro-DIC area scan with one of the 5 Megapixel frames exemplified in the full-field for rolled (a) and extruded (b) samples.

Here, in this study, DIC is used to map considerably large area in microscopic scale. Each individual micro-DIC frame in Figure 3.6 is divided into 61x61 pixel subsets (12x12 μm^2 for rolled sample and 10.8x10.8 μm^2For extruded one) with 10 pixels grid spacing (1.99 μm in rolled sample and 1.78 μm in extruded one).

3.3.3. Post-Processing of DIC Maps

In the micro-DIC analysis, every frame (I,J) at a load point is by default analyzed with the corresponding frame (I,J) in the reference state. When required (particularly at larger-strain load points where material points shift more noticeably), analysis with surrounding

frames (e.g., deformed frame (I,J) analyzed with respect to reference (I+1,J) at their material intersection) are also conducted to avoid gaps in the full-field.

Additionally, sequential analysis results, which take the DIC reference as the previous load point/points are provided. These are very instrumental in investigating the progression of strain accommodation patterns. When sequential analysis results are referred to, they will be distinguished with "Δ", e.g., $\Delta\varepsilon_{yy}^{a-b}$ will stand for the DIC results obtained by analyzing load-point-b images with respect to load-point-a images.

Further, to single out and illustrate the spatial location of the two sets of pure tensile/compressive shear bands with distinct characteristics when both *coexist*, a binary filter is applied to specific strain maps. A threshold of 0.7% is found to be adequate for revealing the superstructures. Hence ($\varepsilon_{yy} < -0.7\%$) to reveal compressive (strain features with negative sense) and ($\varepsilon_{yy} > 0.7\%$) for tensile population (strain features with positive sense) are applied. The discussion in section 4.1.1 and specifically Figure 4.7 benefits from binary filter on strain maps.

Adding macro DIC (similar subset and grid spacing size; 415 μm , 68 μm), a massive computational load is constructed which is handled by number of remotely connected workstations. All processes starting from sample positioning at desired (x, y) over the surface, autofocusing in z direction, image capturing, data transfer to central storage, recalling saved images, stitching the individual frames to construct the full field images and DIC calculations are done by In-House python codes developed at **M**echanics of **adv**anced material **Lab**oratory (MadvLab) at Boğaziçi University.

As a measure of plastic anisotropy and to have a good understanding of the effect of texture on level of heterogeneity in deforming wrought Mg, apparent Poisson's ratio is exploited. By definition, this dimensionless quantity is expressed as the ratio of average measured strain in transverse direction to the same measure at the loading direction such that

$$\nu_{xy} = -\frac{\bar{\varepsilon}_{xx}}{\bar{\varepsilon}_{yy}} \quad , \quad \nu_{zy} = -\frac{\bar{\varepsilon}_{zz}}{\bar{\varepsilon}_{yy}}. \tag{3.2}$$

3.4. CPFE Implementation

3.4.1. Simulation Workflow and Constitutive Formulation

Crystal Plasticity Finite Elements (CPFE) is a powerful computational framework used to simulate the deformation and mechanical behavior of crystalline materials at a microscopic level. It combines the principles of finite element analysis with the crystal plasticity theory, which considers the interactions between the crystallographic structure of a material and the applied load. Spectral method is a more efficient solver that can implement the analysis in the Fourier domain.

One popular software package used for CPFE as well as spectral simulations is DAMASK (Düsseldorf Advanced Material Simulation Kit), which is an open-source platform for the simulation of microstructures, crystallographic textures, and other related phenomena. DAMASK is a highly versatile tool that can be used to simulate various deformation mechanisms, such as dislocation slip, twinning, and grain boundary sliding, under different loading conditions, including tension, compression, bending, and shear. It provides a flexible framework that includes several pre-implemented models for different crystal structures and loading conditions, as well as the ability to define custom models for specific applications.

Multiscale modelling of deformation in DAMASK is provided through a material point model. The hierarchical structure of the material point model allows for the simulation of material behavior at multiple length scales, from the macroscopic to the microscopic level. This makes it well-suited for studying the effects of microstructural features, such as grain boundaries, defects, and dislocations. This model also allows for the simulation of various types of material behavior, including *elasticity*, *plasticity* (Isotropic, phenomenological crystal plasticity, dislocation density-based crystal plasticity, crystal plasticity including dislocation flux), *damage* (phase field damage, damage driving force), and *thermal* (heat flux, heat generation, thermal expansion), making it a versatile tool for studying the mechanical behavior of materials at the microscale.

The hierarchical structure of material point model includes macro, meso and micro scales; the macro field response is determined from atomic scale behavior that depends on initial field boundary condition values itself. It starts by defining the boundary condition at macroscale in the form of average deformation gradient $\bar{F}$. At next level, applied deformation gradient $\bar{F}$ is decomposed among N_g microstructural constituents of the polycrystal F (partitioning). Then, crystallographic orientation, grain size, and other microstructural features of the material points are taken into account to solve elastoplastic deformation problem at microscale. The constitutive response of each crystal is then averaged out at mesoscale level (homogenization) to form field stress $\bar{P}$ at macroscopic scale such that

$$\bar{F} = \sum_{g=1}^{N_g} \nu^g F^g, \qquad \bar{P} = \sum_{g=1}^{N_g} \nu^g P^g, \tag{3.3}$$

where, F is deformation gradient tensor: $\mathrm{dy} = \frac{\partial \mathrm{y}}{\partial \mathrm{x}} . \mathrm{dx} = \mathrm{Grad\,X}. \mathrm{dx} =: \mathrm{F(x)}. \mathrm{dx}.$ ν is the volume fraction of constituent g.

Full-field modelling and homogenized modelling are two approaches used in computational mechanics to simulate the behavior of materials and structures considering grain interactions. Full-field modelling involves creating a detailed model of the material or structure, with all its microstructural features and defects included. This approach requires a high level of computational power and can be time-consuming, but it provides highly accurate results. Full-field modelling is often used when the microstructure of the material is critical to its mechanical behavior. Homogenized modelling, on the other hand, simplifies the material or structure by assuming it is homogeneous and isotropic, with uniform properties throughout. This approach is much simpler and faster than full-field modelling but can be less accurate, especially in materials with complex microstructures. Homogenized modelling is often used when the macroscopic behavior of the material is more important than its microstructure. DAMASK can utilize various homogenization schemes, e.g., iso-strain, and relaxed grain cluster homogenization schemes.

In case of magnesium, since substantial local deformation gradient is expected [84], a full-field approach is considered. Hence, $N_g = 1$, that means a large set of constituents with each containing only one data point, increasing the accuracy and cost of modeling at the

same time. This statement also holds for stress variants. *Thus, no decomposition or homogenization scheme is introduced in numerical analyses*.

Mechanical behavior of the material is defined by sets of PDEs that are solved with given boundary condition to satisfy the conservation law such as energy, mass, or momentum conservation laws. Customized conservation laws could be introduced into DAMASK in addition to currently supported ones: Mechanical equilibrium, phase field damage and heat conduction. Since damage and heat conduction are not the case for this study, only mechanical equilibrium with linear momentum conservation is considered. This equilibrium for both interconvertible first Piola-Kirchhoff (P) and Cauchy (σ) stresses are mathematically described by

$$\text{Div P} = \rho_0 \ddot{y}, \text{ undeformed medium,} \tag{3.4}$$

$$\text{div } \sigma = \rho_t \ddot{y}, \text{ deformed medium.} \tag{3.5}$$

To solve the PDEs, DAMASK is integrated with several numerical solvers (FEM, FVM, FDM), however, a built-in spectral solver based on Fast Fourier transform (FFT) which is more robust and cost effective compared to FE is used for the purposes of this thesis. A spectral solver is a numerical method for solving partial differential equations (PDEs) that involves expanding the solution in terms of a set of basis functions, typically orthogonal functions such as Fourier or Chebyshev polynomials. The spectral solver then uses the expansion coefficients to approximate the solution of the PDE [79,80].

To start with, deformation gradient goes through multiplicative decomposition. In this approach, the deformation of a polycrystalline material is decomposed into three components: elastic, plastic, and lattice-distorting inelastic component. The elastic deformation component F_e, represents the reversible deformation that occurs when a load is applied to a material, and it returns to its original shape when the load is removed. The plastic (volume-preserving) deformation component F_p, represents the inelastic irreversible deformation that occurs due to the plastic deformation mechanisms activity such as movement of dislocations in the material. The lattice-distorting inelastic component F_i, represents the irreversible deformation that occurs when the crystal structure of the material changes, such as during phase transformations. The total deformation of the material is obtained by multiplying the three components together, giving the general expression as

$$F = F_e F_i F_p. \tag{3.6}$$

The advantage of the multiplicative decomposition approach is that it separates the different deformation mechanisms, allowing each component to be modelled separately. Time evolution of inelastic deformation gradient components could be described as multiplication of corresponding velocity gradient and deformation gradient such that

$$\dot{F}_p = L_p F_p, \tag{3.7}$$

$$\dot{F}_i = L_i F_i. \tag{3.8}$$

Therefore, to obtain deformation gradients, integration is done from initial time t_0 to t followed by backward-Euler integration

$$F_p(t) = F_p(t_0) + \int_{t_0}^{t} L_p(\tau) F_p(\tau) d\tau, \tag{3.9}$$

$$F_i(t) = F_i(t_0) + \int_{t_0}^{t} L_i(\tau) F_i(\tau) d\tau, \tag{3.10}$$

$$\frac{F_p(t) - F_p(t_0)}{\Delta t} = L_p(t) F_p(t), \tag{3.11}$$

$$\frac{F_i(t) - F_i(t_0)}{\Delta t} = L_i(t) F_i(t), \tag{3.12}$$

$$F_p(t) = \left(I - \Delta t\, L_p(t)\right)^{-1} F_p(t_0), \tag{3.13}$$

$$F_i(t) = \left(I - \Delta t\, L_i(t)\right)^{-1} F_i(t_0), \tag{3.14}$$

with I as identity tensor and F_p and F_i known, F_e could be calculated by Equation (3.6). Thus, the Green-Lagrange strain E and its work conjugate, second Piola–Kirchhoff stress S is obtained as follow

$$E := \frac{1}{2} F_i^T (F_e^T F_e - I) F_i. \tag{3.15}$$

Generalized Hook's law is implemented to derive S from E, with C described in Voigt notation as follow considering magnesium crystal symmetry

$$S = C : E, \tag{3.16}$$

$$\begin{bmatrix} C_{11} & C_{12} & C_{13} & 0 & 0 & 0 \\ C_{12} & C_{22} & C_{13} & 0 & 0 & 0 \\ C_{13} & C_{13} & C_{33} & 0 & 0 & 0 \\ 0 & 0 & 0 & C_{44} & 0 & 0 \\ 0 & 0 & 0 & 0 & C_{44} & 0 \\ 0 & 0 & 0 & 0 & 0 & C_{66} \end{bmatrix}, \tag{3.17}$$

where elastic constants C_{11}, C_{12}, and C_{13} are related to the stiffness of the material along the crystallographic axes. C_{33} represents the stiffness in the direction perpendicular to the basal plane, while C_{44} represents the shear stiffness within the basal plane. C_{66} represents the shear stiffness along the diagonal of the basal plane.

For plasticity, a phenomenological crystal plasticity model based on initial work by [87] is implemented. In this approach, plastic velocity gradient L_p is determined as accumulated shear rate of all slip systems:

$$L_p = \sum_{\alpha} \dot{\gamma}^{\alpha} P_{Schmid}^{\alpha} = \sum_{\alpha} \dot{\gamma}^{\alpha} (m_s^{\alpha} \otimes n_s^{\alpha}) , \tag{3.18}$$

where, m and n represent slip direction and plane normal vectors that shear acts on ($P = m \otimes n$ ($P_{ij} = m_i n_j$)). For shear rates due to different phenomena in Mg, L_p could be elaborated as:

$$L_p = L_p^{sl-untw} + L_p^{tw} + L_p^{sl-tw}, \tag{3.19}$$

with, $L_p^{sl-untw}$ accounting for slip in untwined crystal, L_p^{tw} for twining and L_p^{sl-tw} for slip in twinned region that is defined as:

$$\begin{aligned} L_p = \left(1.0 - \sum_{\beta}^{N^{tw}} f^{\beta}\right) \sum_{\alpha}^{N^{s}} \dot{\gamma}^{\alpha} P_{o-sl}^{\alpha} + \sum_{\alpha}^{N^{tw}} \dot{f}^{\alpha} \gamma^{tw} P_{o-tw}^{\alpha} \\ + \sum_{\beta}^{N^{tw}} f^{\beta} \left(\sum_{\alpha}^{N^{s-tw}} \dot{\gamma}^{\alpha} P_{tw-sl}^{\alpha}\right), \end{aligned} \tag{3.20}$$

where P_{o-sl}^{α}, P_{o-tw}^{α} and P_{tw-sl}^{α} are related to slip in untwinned area, twin in untwinned area and slip in twinned region. f is the twin volume fraction. γ^{tw} is the characteristic shear that could be accommodated by twin mechanism. The key element that governs plasticity is resistance ξ on slip and twin systems during the deformation. The rate of shear provided over each slip system depends on the resistance formed over that system:

$$\begin{aligned} \dot{\gamma}^{\alpha} &= (1 - f_{tw}^{tot})\, \dot{\gamma}_0^{\alpha} \left|\frac{\tau^{\alpha}}{\xi^{\alpha}}\right|^{n} sgn(\tau^{\alpha}), \\ sgn(\tau) &= \begin{cases} -1, & \tau < 0 \\ 0, & \tau = 0 \\ +1, & \tau > 0. \end{cases} \end{aligned} \tag{3.21}$$

To take the unidirectional property of twin when slip is produced by twin mechanism, the Equation (3.21) is rewritten as follows:

$$\dot{\gamma} = (1 - f_{tw}^{tot})\dot{\gamma}_0 \left|\frac{\tau}{\xi}\right|^n \mathcal{H}(\tau),$$
$$\mathcal{H}(\tau) = \begin{cases} 1, & \tau > 0 \\ 0, & \tau \leq 0, \end{cases} \tag{3.22}$$

where $\tau^\alpha$is the stress required to provide γ and is a function of second Piola-Kirchhoff S such that: $\tau^\alpha = g(S, P^\alpha_{Schmid})$. It should be carefully noted that for each P, corresponding S is chosen e.g., with P^α_{o-sl}, stress in untwinned and with P^α_{tw-sl} stress in twinned region is used in Equation (3.16). Total twin volume fraction is the summation of volume fractions of all individual twin mechanisms:

$$f_{tw}^{tot} = \sum_{\beta=1}^{N_{tw}} f_{tw}^{\beta} = \sum_{\beta=1}^{N_{tw}} \frac{\gamma^\beta}{\gamma^\beta_{char}}. \tag{3.23}$$

The contribution of each twin system to total twin volume fraction is the ratio of produced shear at the time step by that individual twin γ^β over the characteristic shear that could be characteristically produced by it: γ^β_{char}.

Resistance in Equation (3.21) and Equation (3.22) over each slip system of $\alpha = 1, \ldots, N_s$ and twin set of $\beta = 1, \ldots, N_{tw}$ follow the relations below respectively:

$$\dot{\xi}^\alpha = h_0^{s-s}(1 + c_1(f_{tw}^{tot})^{c_2})(1 + h_{int}^\alpha) \times \sum_{\alpha'=1}^{N_s} |\dot{\gamma}^{\alpha'}| \left|1 - \frac{\xi^{\alpha'}}{\xi_\infty^{\alpha'}}\right|^a sgn\left(1 - \frac{\xi^{\alpha'}}{\xi_\infty^{\alpha'}}\right) h^{\alpha\alpha'} + \sum_{\beta'=1}^{N_{tw}} \dot{\gamma}^{\beta'} h^{\alpha\beta'}, \tag{3.24}$$

$$\dot{\xi}^\beta = h_0^{tw-s}\left(\sum_{\alpha=1}^{N_s} |\gamma^\alpha|\right)^{c_3} \sum_{\alpha'=1}^{N_s} |\dot{\gamma}^{\alpha'}| h^{\beta\alpha'} + h_0^{tw-tw}(f_{tw}^{tot})^{c_4} \sum_{\beta'=1}^{N_{tw}} \dot{\gamma}^{\beta'} h^{\beta\beta'}, \tag{3.25}$$

where, h values (0 or 1) describe the interaction between different slip systems among each other ($h^{\alpha\alpha'}$), with twin systems ($h^{\alpha\beta'}$) or among twin systems ($h^{\beta\beta'}$). h_0^{s-s}, h_0^{tw-tw}, h_0^{tw-s}, h_{int}^α c_1, c_2, c_3, c_4 are the constant parameters used for fitting purposes and $\xi_\infty^{\alpha'}$is the parameter that controls the upper bound for evolving resistance.

Once L_p is calculated through the Equation (3.20) to Equation (3.25), F_p is determined by Equation (3.13). With F as input and F_p known, the elastic deformation gradient in Equation (3.6), is obtained as follow:

$$F_e = F(F_i F_p)^{-1}, \tag{3.26}$$

then, Lagrange strain E and second Piola-Kirchhoff stress S are obtained by Equation (3.15) and Equation (3.16) and a new loop starts until a convergence criterion for $L_p$is satisfied.

3.4.2. Pre-Processing; Input Data, RVE Preparation

To run a simulation, the following information should be provided to DAMASK:

- Material properties such as elastic constants, critical resolved shear stress (CRSS) values for each slip system.
- Specification of the hardening behavior of the material, which describes how the material's strength changes during plastic deformation. This may include parameters for isotropic or anisotropic hardening models.
- Crystallographic texture which is provided by several means like grain generation algorithms to assign orientations randomly or by an actual orientation distribution function (ODF) that is determined through techniques like electron backscatter diffraction (EBSD) or neutron diffraction or X-Ray diffraction.
- Discretized geometry of the simulated sample, like a polycrystalline magnesium sample. DAMASK provides built-in grid generation functions.
- Definition of deformation systems that are active in simulation of material like slip and twin systems.
- The boundary conditions file defines the applied loads, displacements, and constraints for the simulation. It includes information such as: Boundary Types, Applied Loads and Displacements and Constraints.
- Output Options that specify the desired output quantities, including stress, strain, plastic strain, and other variables of interest.

Damask built-in functions are used to produce RVE consisting of 729 (9×9×9) grains. The average grain size is set to be identical to the experimental samples (~11 μm), generating

a RVE with physical size of $99\mu m \times 99\mu m \times 99\mu m$. “seed.from_random” function is used to create 729 grain seeds with given physical dimensions. Then, a built-In Voronoi-Tessellation function is utilized to create 128×128×128 data points inside the cluster ensuring ~(14× 14 × 14) data points inside each single grain in average. The generated geometry is then saved with (.vti) format and could be presented using external software like Paraview (Section 4.2).

Boundary condition is described in a separate file in (.yaml) format. Load case includes solver type (spectral_basic in this thesis), mechanical boundary condition and discretization of load steps. Boundary conditions are generally applied in the form of a 3×3 matrices:

- F: deformation gradient at the end of load step,
- F_dot: rate of deformation gradient during load step,
- L: velocity gradient during load step,
- P: first Piola–Kirchhoff stress at the end of load step,
- P_dot: rate of first Piola–Kirchhoff stress during load step.

A combination of deformation and stress matrices could also be used to define boundary condition, however, the essential rule here is to maintain mutual exclusivity, e.g, by assigning 0 value to (I,j) component in P if (I,j) element in F is needed to be calculated at each increment (is set by assigning x to the element).

In this manuscript deformation is implemented to the cluster with *rate of deformation gradient during load step* (dot_F = -2.0e-3) in y-direction for simple compression simulation. The load is applied in 10 seconds time interval and 20 increments. Average strain reaches 2% along y direction (dot_F×t = -2.0e-3×10) at the end of final step. For CTC simulation, on the other hand, a three-step loading is considered: first compression loading (dot_F = -2.0e-3, 20 seconds) is followed by a reverse load (dot_F = 4.0e-3, 20 seconds) and a second compression (dot_F = -2.0e-3, 10 seconds) to create a full cycle (-2%, +4%, -2%). To create a complete boundary condition, first Piola–Kirchhoff stress (P) at end of load step is also included in load case according to mixed boundary condition rule. Strain and Cauchy stress are exported for all discrete steps to form stress strain curves shown in Section 4.2.

All phase, texture and constitutive parameter information needed for a simulation is gathered in configuration file (material.yaml). This file together with geometry data boundary condition description file explained previously construct the elements to run the simulation. “ConfigMaterial” function is utilized to construct configuration file. First, homogenization is passed by assigning dummy value to it and creating one whole constituent without discretization to certify a full-field simulation. Phase data includes HPC lattice identifier, c/a ratio (1.6235) and Mg density (1740 kg/m^3). Mechanical description comprises of i) output request list e.g., F, P, F_e, L_p, O(orientation), ii) Elastic constants, and iii) plastic parameters for phenomenological constitutive equations including hardening parameters and interaction identifiers. Plasticity related output could also be requested separately here. Examples of a Load case and material configuration files are provided in the Appendix.

Grain orientation information is assigned to grain population by built-In function “damask.Rotation.from_ODF”. This function takes three arguments: i) number of grain population. This number should be identical to the number of grains that is used to generate RVE explained earlier, ii) orientation data in the form of (m×3) list. Three columns are representing ϕ_1, ϕ, ϕ_2 rotating angles in Bunge notation, iii) weight of each orientation. The ODF data here is extracted from actual rolled and extruded sampled pole figures presented in Figure 3.2 processed by MATLAB MTEX toolbar. Initial grain geometry and orientation for rolled and extruded Mg is represented in Section 4.2.1, 4.2.2 respectively.

4. RESULTS AND DISCUSSION

4.1. Experimental Results

4.1.1. Rolled Sample

Macro-DIC is used to construct real-time stress-strain curve evolution. At the end of loading path, this curve represents the full cycle engineering stress (σ) vs average axial strain (ε_M) curve. For ease of reference, four quadrants and micro-DIC load points are labelled. The experiment starts with applying compressive strain up to -2% followed by an unloading to the first zero stress (b). This negative load-negative strain region is labelled as quadrant I. In quadrant II, load is reversed to tension and the compressive strain accumulated along the first quadrant is fully recovered at first zero-average-strain point (d). Tensile straining continues up to 1.65% (f) where the loading direction is reversed once again, and second zero-average stress point is reached (g). This positive-stress, positive-strain part of the curve is marked as quadrant III. Quadrant IV comprises of a second compression cycle and starts beyond point g, continues to second zero strain point (i) where the average tensile strain measured at point g is entirely retrieved. Sample is then unloaded from point I to relieve the stress (j), end of cycle.

Strain evolution at different load points along the full cycle over top ($TD^{\perp}$) and side ($ND^{\perp}$) planes are pictured side by side in Figure 4.2. Orthogonal observation planes are placed side by side for ease of illustration. A 3-D macroscopic shear band developed at point a, projects on TD surface (ND-RD plane) as a ~45° band and forms a horizontal band over ND surface (RD-TD plane). This 2D plain-structured shear band grows perpendicular to it's normal (red arrows) in both directions until it engulfs nearly entire surface at point b. Tensile strain accommodation on the other hand, starts and develops in a much macroscopically homogeneous manner. Since adequate plasticity is introduced at point f (1.65%), to avoid micro-DIC invalidations due to out of surface nature of tensile strain, further loading is halted, and sample is reloaded at this point. The second compression cycle shows somehow convoluted strain accommodations at macroscopic level. To elucidate the mechanism and

nature of this complexity, further details will be discussed with the aid of micro-scale results in upcoming sections.

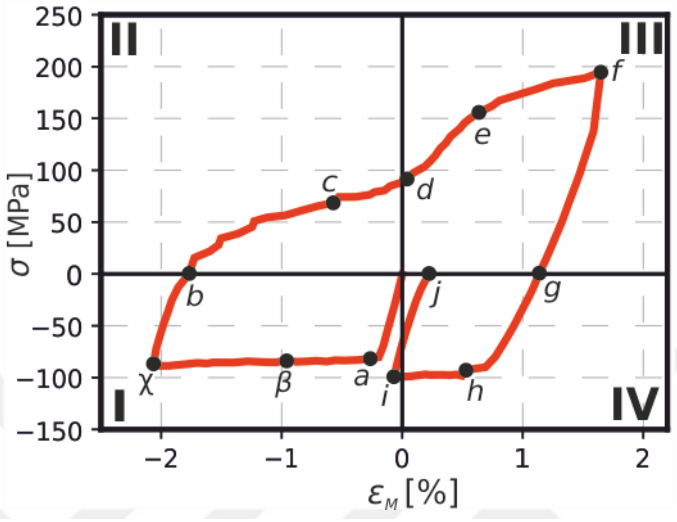

Figure 4.1. Engineering stress-strain curve of the compression-tension-compression cycle obtained using the finely-spaced macro-DIC data. Load points that correspond to micro-DIC area-scans are indicated with letters.

In present study, micro-scale measurement is achieved by acquiring imaging resolution as high as 0.199 $\mu m/mm$ and statistical significance is reached by considering a large grain population (~10^5) with huge set of measurement data points (3x10^6). The combination maps over the full cycle are provided in Figure 4.3 for selected points marked in Figure 4.1.

σ and ε_M stand for the engineering stress and the average axial strain, respectively. Begin with compression in quadrant I, the first sign of non-homogeneous strain accommodation is developed at point *a* ($\varepsilon_M = -0.26\%$) with an abrupt appearance of ±45° TTD shear bands. A highly strained major band forms while the rest of surface is almost strain free. With further straining, the dominant band expands. Successive bursts of TTD bands continue until a significant portion of measurement surface is occupied and at some point, then another major conjugate shear band pops up (shown with white arrows in Figure 4.3b. Although the severe strain accommodation over the surface, specially at the

conjunction of intersecting conjugate bands, the left bottom corner of the measurement surface remains dormant at maximum compression of this cycle ($\chi, \varepsilon_M = 2\%$).

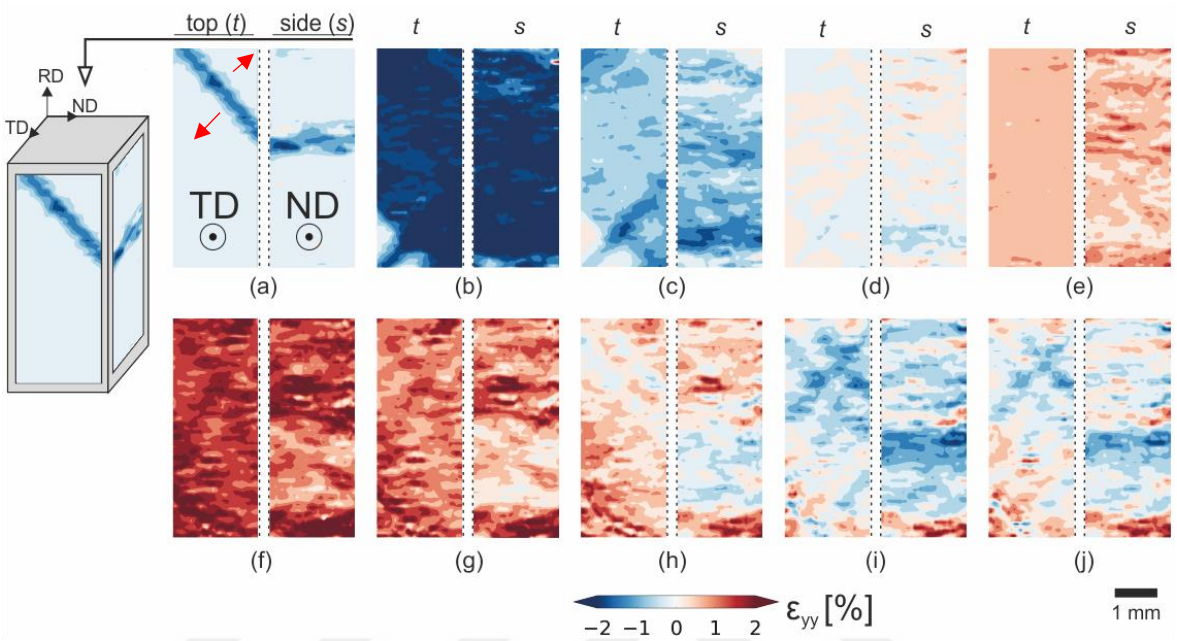

Figure 4.2. (a-j) Macro-DIC axial strain maps for top and side surfaces, presented side by side for load points a-j shown on Figure 4.1. An aid for 3-D visualization is provided for point a.

Entering the quadrant II and upon unloading, the accumulated strain gets recovered homogeneously. The combination map at point c shows that substantial recovery occurs over almost the whole strain field. However, this is not a full recovery since strain features are still present at point d where the average strain is mathematically zero. The subsequently formed conjugate +45° band persists at zero-strain point d enforcing compressive strain content. Hence, to maintain the overall average of zero, the rest of the surface accommodates positive homogeneous-like strain field.

In quadrant III, tensile strain starts to form an utterly different set of shear structures; Narrow local non-45° shear bands with semi-homogeneous distribution over the field along with uniform strain accommodated at the rest of the surface Figure 4.3e). Further straining up to point f ($maximum\ tensile\ strain, \varepsilon_M = 1.67\%$) does not alter the structure of strain accommodation like what observed in compression and only results in much intensified

strain field. Unloading the sample from this point yields another homogeneous strain recovery with substantial resultant strain ($\varepsilon_M = 1.14\%$) at second zero-stress point g. With the complex strain field at the end of quadrant III, the formation of newly accommodating TTD bands over a previously occupied medium is highlighted in this study.

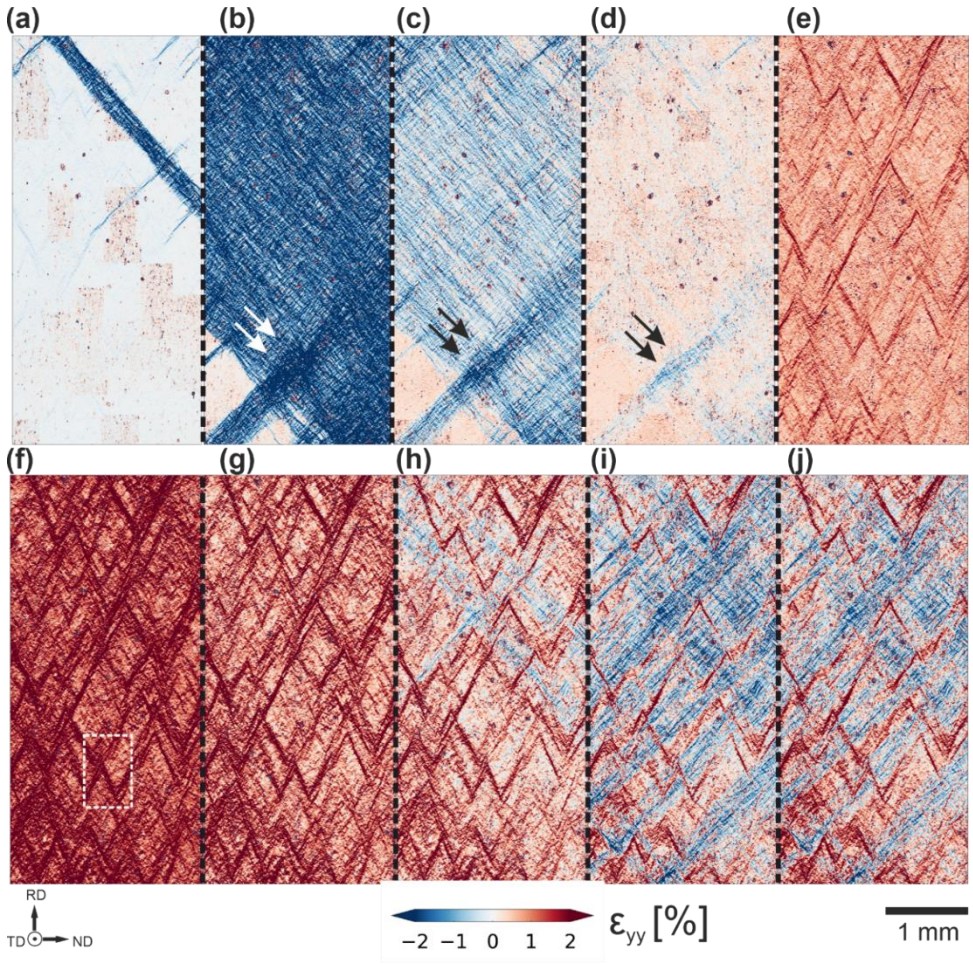

Figure 4.3. Combination micro-DIC maps for axial strain at load points a-j

Second wave of $\pm 45°$ TTD shear bands (SW-TTD) intertwin among the None-45° (h, ε_M = -0.53%). With further compression, the number and intensity of SW-TTD shear features increases. The characteristic similarities/deviations between this set of shear features and the first wave of TTD shear bands (FW-TTD) formed in quadrant I are further investigated in upcoming sections.

At second zero-strain point i, tensile strain features (red) and SW-TTD structure (blue) are intermingled in a way that their average strain contents are identical and opposite in sign. Hence, cancelling each other, the overall zero-strain is maintained. Experiment ends at stress-free point j with another semi-homogeneous strain recovery.

To elaborate the complexity of strain field formed and developed during second compression cycle, all strain variants along with rotation field at point i is depicted in Figure 4.4. To aid the analogy here, strain maps of two other points, β and f, are provided. In former, TTD structures and in the later, non-45° features operate exclusively. The substantial formation of shear bands on the measurement surface (TD), states that in both cases shear plane is strongly yields on observation plane. With 2D nature of shear plane, a simple shear description explaining both structures are provided in Figure 4.5.

In $\pm 45°$ TTD shear bands, the infinitesimal strains ($\varepsilon_{xx}, \varepsilon_{yy}$) for TTD shear bands are principals, hence, ε_{xy} is nearly zero (-a). Following the loading direction (compression) for TTD shear bands, ε_{yy} is negative (Blue) and due to Poisson's effect, ε_{xx} is positive (Red). Rotation, On the other hand, adopts both Red for +45° (CCW) and Blue for -45° (CW) shear families making ω_{xy} map a useful variable for interpretation of deformation field. The dichromatic color bar is preferred to better interpret rotation. With the limited stain that could be accommodated by shear process of twin, the burst of conjugate shear families is inevitable at some point; shown in Figure 4.4a in black dashed circle. The conjugate shear bands, naturally, has the same sign (-) for ε_{yy} and (+) for ε_{xx} , yet opposite color representation for ω_{xy}. This implies, once again, while in both ε_{yy} and ε_{xx}, conjugate shear bands superimposed on top of each other leading to sever local inhomogeneity, for ω_{xy} they cancel each other, eliminating rotation field at intersections (Figure 4.4a, yellow circle). Hence, ω_{xy} should solely be used as an aid for interpretation of deformation, else, it will falsely report strain free domains when opposite rotations coexist.

Same ideal representation is provided for non-45 ° shear structures in (Figure 4.5b). Here, for tension along y direction, $\varepsilon_{yy}/\varepsilon_{xx}$ gets negative/positive values (Blue/Red) and are not principals anymore which means θ is not 45°. As it could be interpreted from Figure 4.5b, ε_{xy} will not be null, noticed by the intense strain features over ε_{xy} in Figure 4.4b. Also,

like ω_{xy}, conjugate bands in ε_{xy} have opposite signs ($+\theta/-\theta$ shears). Rotation senses (Figure 4.5b) are inverted compared to Figure 4.5a due to reverse loading direction.

Shear structures at points β and f, are mostly of the pure form of SW-TTD and non-45°. At point i however, both shear features coexist. Newly forming non-45° bands intermingle among the remnants of previously accommodated SW-TTD shear structures (Figure 4.4c). Examples of formed shear bands are decorated with yellow dashed lines.

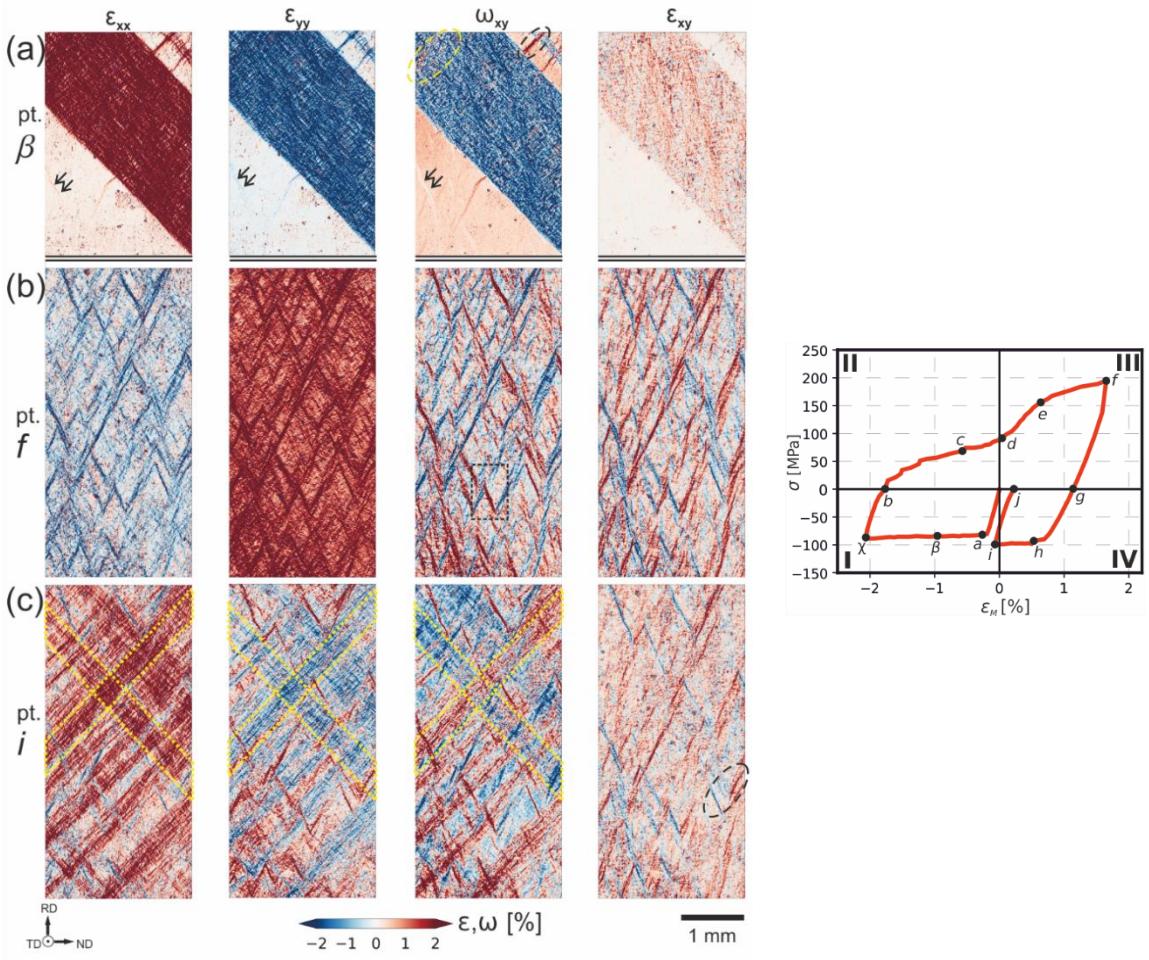

Figure 4.4. Combination micro-DIC maps for in plane strain components (ε_{xx}, ε_{yy}, ε_{xy}) and infinitesimal rotation (ω_{xy}) for (a) point β, (b) point f, and (c) point i.

To focus on quadrant IV, all strain variables and rotation maps are demonstrated over the g-h and h-i increments in Figure 4.6. From point g to h, primary constituents of reversal activity over non-45° structures are followed by accommodation of SW-TTD shear bands. SW-TTD structures on top section of the sample, formed in two -45° and one +45°

identifiable shear bands. Consistent with the sense depictions in Figure 4.5, $\Delta\omega_{xy}^{g-h}$ takes blue/red for -/+ shear structures. $\Delta\varepsilon_{xy}^{g-h}$ shows faint signal and $\Delta\varepsilon_{xx}^{g-h} \cong \Delta\varepsilon_{yy}^{g-h}$is also maintained.

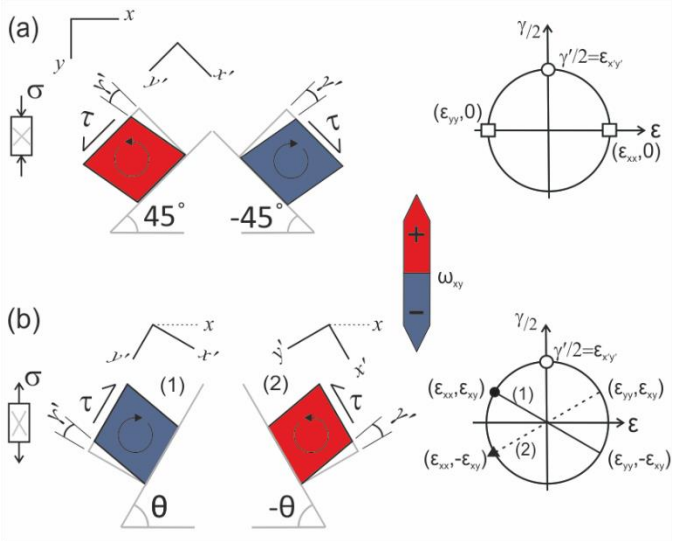

Figure 4.5. Kinematic depiction of simple shear in the x-y plane in terms of infinitesimal strain and rotation components (ω_{xy}) for (a) ±45°compressive and (b) ± θ tensile structures in conjunction with the utilized blue (−), red (+) colorbar. The colors of the sheared elements pertain to ω_{xy}.

Since reversal of shear activity is in the action from g to h, the strain and rotation senses in Figure 4.5a are opposite to Figure 4.5b. The reversal process over non-45° shear bands is started earlier at point f; shown by $\Delta\varepsilon_{yy}^{f-g}$ map in Figure 4.6c. Figure 4.6b depicts strain and rotation accommodation over the second twin plateau from point i to h Several SW-TTD bands form. The incremental strain and rotation maps reveal a major activity over 45° structures exclusively. There is no accommodation or recovery by other activities like non-45° structures at this increment. also, the shear bands formed at g-h increment and indicated by two dashed lines in Figure 4.6a, does not appear in Figure 4.6b. Instead, newly coming same-angled shear structures are formed above the upper dashed line (shown by arrows). This implies that, like first twin plateau, further strain accommodation occurs in the form of expansion of shear structures over the surface rather than overlaying on existing structures.

In h-i increment, on the other hand, there is no evident recovery over non-45° structures since it is already ceased before point h.

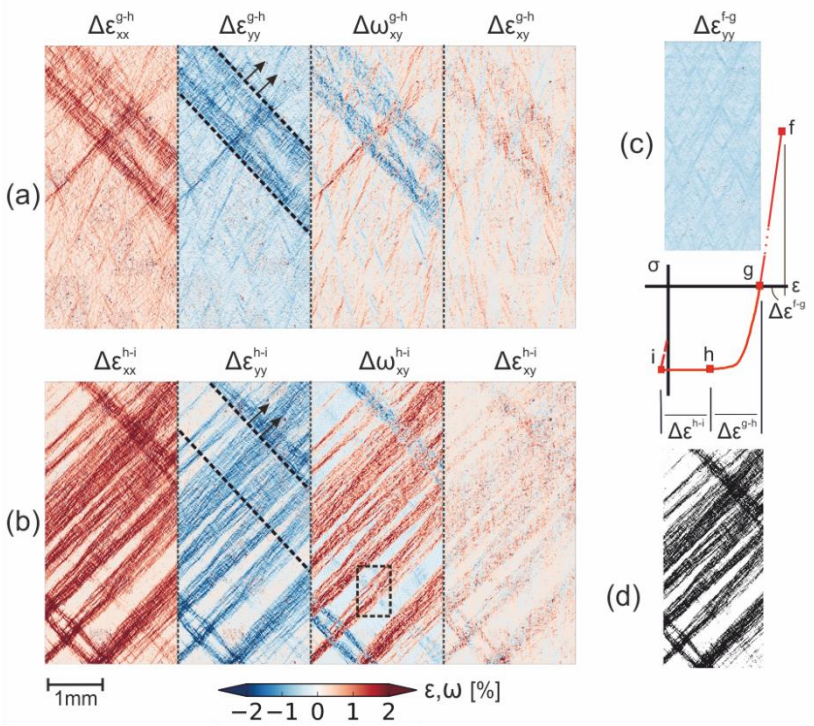

Figure 4.6. Incremental strain/rotation maps that single out deformation from (a) point g to h, (b) point h to i, (c) from point f to g (for only axial strain); (d) binary map of chosen points for the second-wave tensile twin driven bands in stage $h - i$ (part b). Part (c) contains a sketch of the considered increments over the cycle.

To detail the level of heterogeneity, two zero-strain points d and i with different loading path history are picked. The former is reached after applying compression then stretching back to original state and the latter undergoes further stretch then reload until zero-strain state. While at point i there is a very limited variability of strain field, point i shows significant heterogeneity. To show the deviation in statistical terms, strain histograms are provided in Figure 4.7. The statistical distribution of strain at point i is much wider than point d, indicating a higher level of heterogeneity. The state at point d is rather simple; accommodated strain by the tensile twin is recovered by reverse mechanism (detwin). However, at point i, to cancel out the accumulated strain imposed by remnant non-45° structures, highly compressive strain features coexist. The average strain over these two

structures must be equal to maintaining nearly null total average. Spatial location of both structures is extracted by setting a proper threshold (ε_{yy}> 0.7% for tensile and ε_{yy}< -0.7% for compressive structures). Both structures have consistent spatial characteristic with non-45° and TTD strain localization superstructures reported in Figure 4.3. Strain histograms (ε_{yy}) of points f, g, h and i are compared in Figure 4.7b. as mentioned before, the non-45° structures at point i are the persisting ones after limited recovery over the utmost strain field at point from f to i. This limited recovery occurs mostly up to point h beyond which, the progression of strain accommodation under second compression follows a perfectly-plastic-like trend. This stage of deformation is associated with nearly pure SW-TTD over residue of non-45° population. The co-occurrence of fixed-in-place non-45° and SW-TTD shear structures at the same time results in an intense strain heterogeneity at point i.

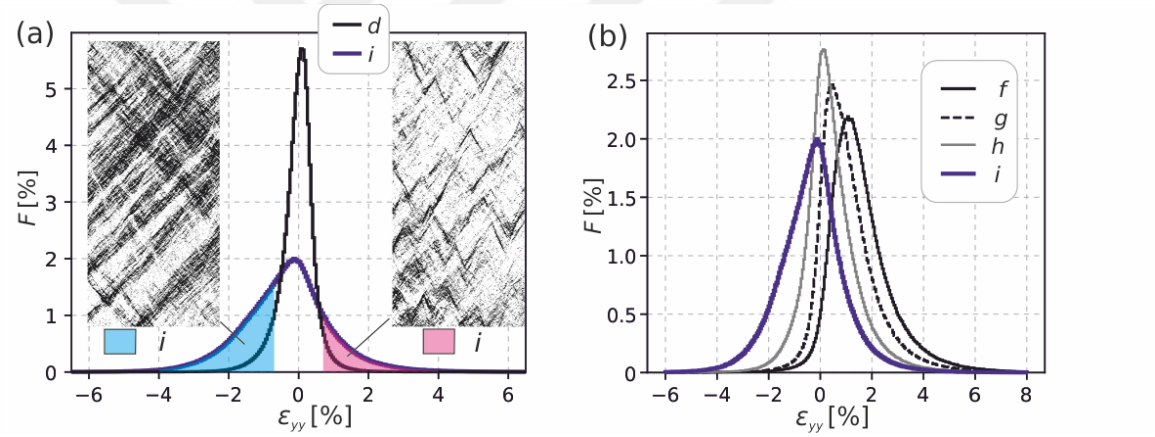

Figure 4.7. Axial strain histograms (a) at the two points (d, i) where strain averages are nominally null, (b) at points f, g, h, i.

Starting from their first appearance at point e, the overall activity in the non-45° bands is entrenched in a fixed rhombic pattern (Figure 4.3 e-j). This trait is a result of their microstructural origins and dissimilar to the TTD bands that propagate over the field. It has been shown that these strain bands coincide with a secondary microstructure that is composed of small grains whose local texture is weaker than that of the overall matrix [16], [73]. This means more favorable Schmid factors for basal slip—the easiest micromechanism by several factors—in these material bands compared to the surrounding matrix where basal slip is geometrically hard [73], [88,89] . The peculiar non-45° shear angles simply derive from the geometric orientation of these formations whose physical origin is dynamic

recrystallization (DRX) in the previous forming operation. In basic terms, these structures are typical since (i) DRX during the forming processes of Magnesium alloys is typical [90], and (ii) it does not occur homogeneously [91,92] (though the specifics will depend on the alloy [91] and processing parameters.) We carefully note that the plate of the study is annealed (as is the case in most investigations) yet annealing proves to have a limited effect on micro-texture [91]. The fact that softer material regions can be inherited through local texture is predicated on the extreme plastic anisotropy of the Magnesium crystal. A more detailed literature account in this topic and further elaboration for the plate of the study with EBSD (selected area orientation and Schmid factor maps) is provided in [16] where the focal point is on detailing the deformation of these structures. Unlike twinning, (basal) slip is not unidirectional and, activity inside these inherent material bands is questioned in the quadrant-I compression as well. The compression-side activity of the non-45° bands is indeed vaguely perceptible (e.g., arrows in Figure 4.4a). Yet, in the restricted stress level ordained by the FW-TTD band regime (~80 MPa), they are strained to a very limited degree before being engulfed by the FW-TTD bands. In contrast, quadrant III deformation that has primary contributions from hard mechanisms (particularly the prism slip, e.g., [32]) exhibits heavy hardening and, by point f, intense strain localization sets in the non-45° bands at a stress level of 190 MPa.

Only a limited Hall-Petch effect is noted in these smaller grain patches [73]. Therefore, if their deformation is solely associated with basal-slip, the apparent deduction (over the quadrant-I deformation) that the stresses required to significantly activate them are higher than that required to activate the tensile-twin would be unexpected. We further supplement this point by an aspect of their cyclic plasticity: The latent hardening imparted in the non-45° band regions by point f are complex and layered, since the band strains recover all through f-g (Figure 4.6c) and g-h (Figure 4.6a), while any further recovery of the final remnants would clearly require a flow stress higher than the 100 MPa level that triggered the SW-TTD bands. Both these observations are consistent with the compound nature of the intergranular strain localization [18]: basal slip is merely the primary mediator, there are grains and interfaces along the transgranular path where hard mechanisms (e.g., prism and type-II pyramidal slip) are activated.

SEM micrographs in Figure 4.8a, Figure 4.8b are provided to portray the morphology of the tensile twin network that underlies the TTD band. These are measured in the first twin plateau over an auxiliary sample cut from the same plate. Their region is purposefully selected around the border between the TTD band and the dormant material (this nominal-45° boundary indicated with dashed lines.) Thus, the fields of coordinated (autocatalytic) twinning are clearly contrasted with the neighboring twin-free fields. While Figure 4.8 substantiates the TTD band morphology for the material of the study, it is already well-established that coordinated twinning leads to large-scale strain localization [22], [24], [26].

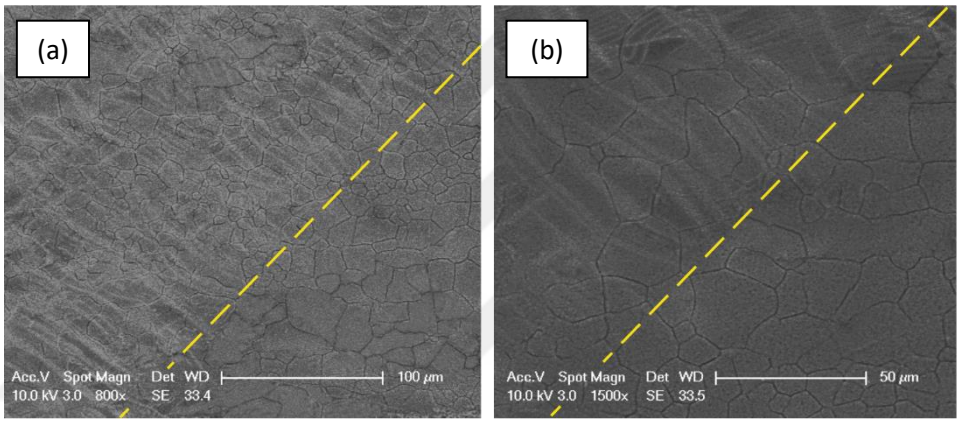

Figure 4.8. Selected-area SEM micrographs in the first twin plateau with (a) 800x, and (b) 1500x magnification recorded at the boundary of a tensile-twin driven band (the separation with dormant fields is indicated with a dashed line).

The adopted name tensile-twin-driven bands, while ascertaining the major constituent and root cause of localization as the tensile twin, also allows for the slip contributions. Note (i) slip is required to accommodate the twins [14], [93], (ii) in Magnesium, the easy basal slip anyways shows appreciable activity in any realistic grain cluster under any load [14]. (In RD compression as well, basal slip is commonly cited as the primary slip mode that accompanies the profuse tensile twin [47], [55], [80].)

However, it is of course the abrupt character of the tensile twin that culminates in the pulsed progression of the TTD bands [15], [25]. In this regime, the initial band forms abruptly with a certain strain distribution—it does not gradually reach that value—and, in further stages, the strain is by and large fixed in the band region unless new band(s) arrive

at the locality [15]. TTD-banding operates in sudden (in this case, also audible) steps where existing bands expand and/or new bands are formed. The spatial evidence of how well this notion is realized in the first twin plateau is shown in Figure 4.9a that shows $\Delta\varepsilon_{yy}^{a-\beta}$ and $\Delta\varepsilon_{yy}^{\beta-\chi}$ fields. Notice the near-null strain accommodation in the incremental $\Delta\varepsilon_{yy}^{a-\beta}$ fields ($\Delta\varepsilon_{yy}^{\beta-\chi}$ fields) at the already-banded regions of point a (point β) shown in Figure 4.3a (Figure 4.4a).

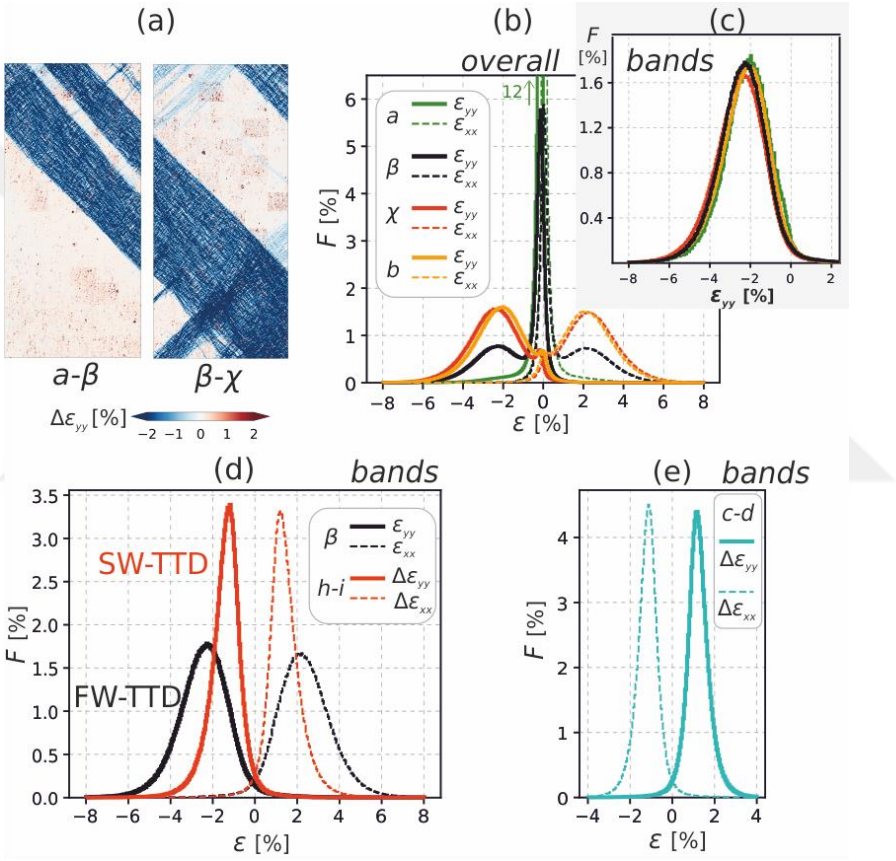

Figure 4.9. (a) Incremental strain maps for stages a-β and β - χ. (b) Strain histograms for points a, β,χ,b in the overall field, (c) exclusively over the band populations. (d) Histograms of the second wave h-i stage bands put in perspective of the first wave bands at point β, (e) Histograms that depict strain recovery over stage c-d.

To elaborate the strain composition of the FW-TTD bands, we first consider the entire-field histograms at points a, β, and χ in Figure 4.9b. (Point b histograms are also included to show that the unload essentially imparts a small shift in the point-χ distributions.) The bimodal strain fields (dormant or shear-banded) lead to a double-peak character in the ε_{yy}

(ε_{xx}) histograms in Figure 4.9b. The central sharp peak of the dormant populations is sequentially replaced by the much wider second peak (FW-TTD points) as the bands spread from a to χ. The mirror-symmetry of ε_{xx} and ε_{yy} distributions is another manifestation of the planar kinematics of the bands ($\varepsilon_{yy} \approx -\varepsilon_{xx}$). The band histograms are shown in Figure 4.9c that only consider the populations in the band areas. The number of selected band points are 133 k, 1.3 m and 2.6 m for points a, β, and χ, and to allow a fair comparison, the y-axis plots the frequency F, namely, the point count in each strain-bin normalized by the total number of selected band points.

In Figure 4.9c, the largely overlapping strain distributions indicate the existence of a characteristic strain distribution in the FW-TTD bands. This agreement is despite a limited systematic disturbance, namely, increase in the area fraction of cross-banded regions that undergo the strain of both +45° and − 45° bands. (Clearly, a physically sensible definition of the characteristic strain distribution should pertain to the activity of singular bands over yet-undisturbed material fields.) For brevity, we finally note that the average FW-TTD axial band strains fall in a small bracket −2.3 ± 0.15% (apart from major band intersections), and proceed to the more crucial evaluation in the cyclic loading context of this study: the change in the composition of the SW-TTD bands in comparison the first wave that progressed over the maiden material. For characterizing the SW-TTD band activity, the fields of the h-i increment are considered where the SW-TTD bands singlehandedly accommodate the specimen strain (Figure 4.6b). The SW-TTD bands that formed in the previous (g-h) increment (where there is interference from strain recovery in the non- 45° bands) are also instrumental, to corroborate that the SW-TTD bands also possess characteristic strain levels. Precisely, the bands that formed in the g-h stage show no activity in the h-i stage, confirming that SW-TTD bands emerge with and maintain a characteristic strain level in analogy to Figure 4.9.

The SW-TTD band points are selected (Figure 4.6d) with a threshold-filtering procedure and Figure 4.9d shows the corresponding $\Delta\varepsilon_{xx}^{h-i}$ and $\Delta\varepsilon_{yy}^{h-i}$ histograms. Point-β FW-TTD band histograms are also shown for comparison. The narrower histograms and smaller average strain (1.4%) of the SW-TTD bands indicate that they form with a significantly more diluted strain network. The difference at the high-strain tails of these SW- and FW-TTD band histograms is also emphasized (0.001 frequency ε_{yy} values are

approximately −4% and − 6%, respectively). This measure of the strain dilution is entirely insensitive to the manner band points are chosen. In fact, the maximal compressive values in TTD-band histograms are also maximal in the entire population, i.e., the left tail of full-field ε_{yy} histograms also coincide with −4% for point-i (Figure 4.7a) and− 6% for point-β (Figure 4.9b).

The symmetry of the $\Delta\varepsilon_{xx}^{h-i}$ and $\Delta\varepsilon_{yy}^{h-i}$ histograms confirm the planar kinematics of the SW-TTD bands. (The same point is also reiterated for point β in Figure 4.9d. Physically, the shear kinematics is aligned with the operative tensile twins in the average orientation [15], [25].) The fact that the plane of shear of the TTD bands strictly align with the TD$^{\perp}$ plane presents an extreme of plastic anisotropy where all transverse expansion occurs along ND (leading to an apparent Poisson's ratio of 1 in the band regions; compare to 0.5 for isotropic plasticity). Effective Poisson's ratio ($-\varepsilon_{xx} = \varepsilon_{yy}$ computed in all the bands-elections considered so far (a, β, χ, h-i) fall in the bracket 0.97 ± 0.02. The implied near exact coplanarity of shear processes is realized in conjunction with the band running through the entire volume of the sample, already noted for the FW-TTD bands (Figure 4.2, the 3-D construction). Figure 4.2i,j side maps reveal the associated horizontal compressive strain patterns of SW-TTD bands, confirming that they are also volumetric formations. The multi-sample, cyclic macro-DIC experiments of Anten and Scholtes [26] on Magnesium AZ31 also provide further decisive data to this effect.

In summary, while the overall kinematics of SW-TTD band formation preserves the nature of the first wave, its operation is more scattered. Clearly, any difference between the quadrant-IV and quadrant-I operation of the TTD bands is due to cyclic hardening, and in this particular case, there is a strong element of spatial heterogeneity with mesoscale coordination: heavily hardened regions are concentrated in the microtextured crystallite network of the non-45° bands. Examining the point-i maps (Figure 4.4c), many non-45° formations can be suspected of fragmenting the SW-TTD bands as well as diluting their individual operation. To exemplify the former effect, note the region (conveniently) encircled in the ε_{xy}-map, Figure 4.4c. The shown intense non-45° bands in proximity seem to forbid SW-TTD band propagation over this corridor (observe over, e.g., the ε_{yy}-map), splitting the band formation.

To provide local insight to the SW-TTD bands, we next consider a zoom-in of the boxed region in Figure 4.4b. The map for the h-i stage singles out the SW-TTD band formation (Figure 4.10a) and these come over the point-h fields that are provided next (Figure 4.10b). Clearly, the major strain localizations at point h are the remnant non-45° structures, and to see how much these receded with respect to their highest values in quadrant-III, point-f fields are also provided (Figure 4.10c). Data is plotted with 50% transparency over the analyzed image fields to reveal the microstructure underneath; ω_{xy} is opted to clearly visualize the shear structures and their operation senses. The dashed lines in Figure 4.10 guide the eye for the locations of particular non-45° bands of +θ and –θ orientations. The structures marked (1) – (3) in Figure 4.10c refer to the three intersection zones where the indicated +θ and –θ bands crudely converge.

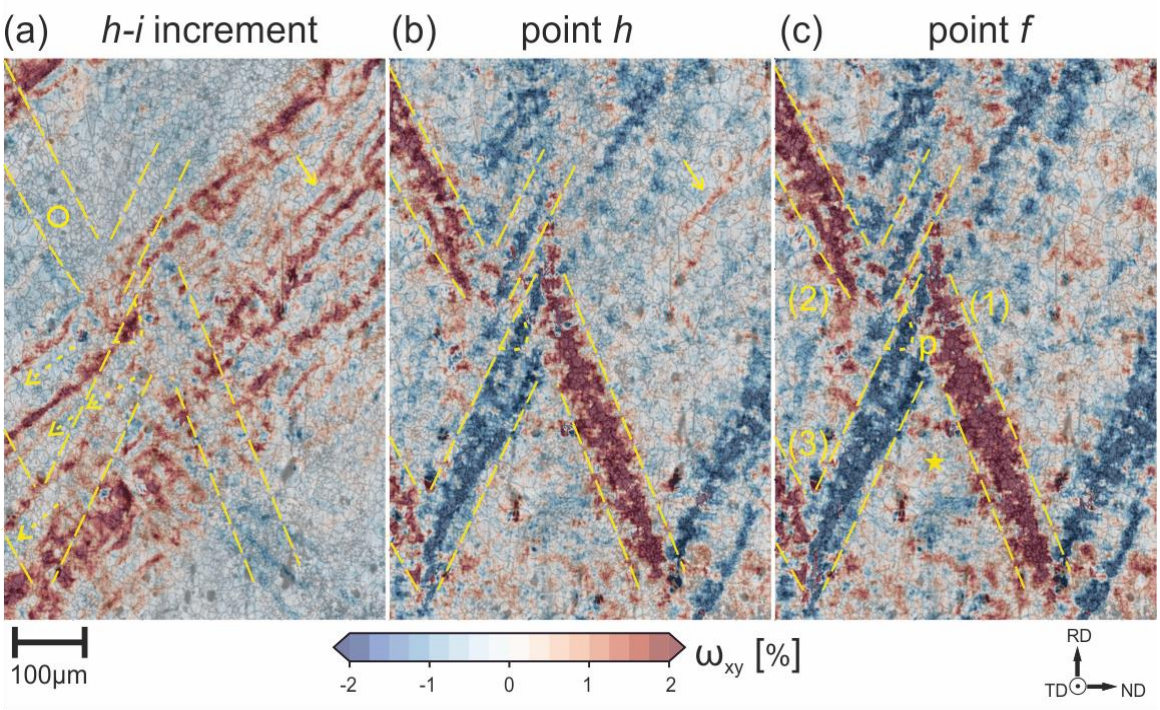

Figure 4.10. Zoom-in map of infinitesimal rotation inside a rectangular region of interest (a) over stage h-i (rectangle indicated on Figure 4.6), (b) at point h, (c) at point f. The contour plot is overlaid over the combined micrographs.

In Figure 4.10a, we first note that the major SW-TTD branch steers below zone (1) and follows the bulk grains that lie below the non-45° bands (marked with a "★" in Figure 4.10c). The corridor that the SW-TTD band avoids inside and to the left of zone 1 is indicated

with back-to-back arrows in Figure 4.10a. Zone 2, similarly, seems to impede the top fiber of the SW-TTD band, leading to a dormant zone to its left (marked with the top arrow). Another dormant zone appears to be associated with the partial avoidance of zone 3 (bottom arrow) as the major SW-TTD branch continues through its bottom tip.

An arrow over the point-h map (Figure 4.10b) shows the precursor of the SW-TTD band formation in this region. The arrow is carried over to Figure 4.10a, by locating its tip at the same grain boundary to show the location of this particular strain localization in the SW-TTD band. In this local setting, it is possible to pinpoint exceptions to the nominally-valid statements on the overall maps, e.g., the large lack of recovery in the non-45° structures in the h-i increment. In Figure 4.10a, limited local recovery in non-45° bands are noted; we exemplify an obvious one inside a pocket p marked with a dashed semi-circle. Note, however, this occurs in conjunction with the SW-TTD activity, since the strain-reversal in zone p further seems to connect to (or perhaps precipitate) a narrow SW-TTD band fiber to its left. In contrast, outside the SW-TTD band activity; recovery in the SW-TTD band segments is virtually absent (e.g., in the region marked with a circle in Figure 4.10a).

Twin-propagation in TTD bands is an abrupt and dynamic event whereas SMDIC is a detailed but slow measurement that scans over the intermediate equilibrium states. Hence, above, the local cause-and-effect relations inside a band propagation have necessarily been discussed with a tentative tone. The more general argument, however, seems evident: The SW-TTD bands negotiate through the spatially-heterogeneous fields of hardening. This appears to be an important factor in the more dilute accommodation of the strain in SW-TTD formations. This is consistent with Anten and Scholtes [41] who reported a similar dilution effect (some differences primarily due to their smaller strain range) in its averaged form, i.e., as it reflects on the macro-scale maps. Here, we resolve microstructural constituents and provide reasoning for the dilution.

It is well-known that detwinning is the dominant micromechanism in quadrant II (e.g., [5], [47]). In this measurement, the spatial manifestation of detwinning on the microstructural strain maps (Figure 4.3b-d) is found to be straightforward: The exact intergranular band patterns that compose the FW-TTD bands gradually release strain. The planar kinematics of the FW-TTD bands should then apply to their reversal, and this is

exemplified in Figure 4.9(e) that presents the mirror symmetry of $\Delta\varepsilon_{yy}^{c-d}$ and $\Delta\varepsilon_{xx}^{c-d}$ histograms (c-d increment values are used to single out the detwinning-dominant operation in this segment). As apparent in Figure 4.3(b-d), detwinning spatially occurs homogeneously over all band structures. The contrast that the TTD bands form in cascades but recover homogenously over all band fields is consistent with previous macro-scale measurements [25,26], further shown here to apply for intergranular fields. The abrupt characteristic strain (Figure 4.9(c)) that is associated with the FW-TTD cascades is also absent in the detwinning-dominated strain recovery. (The strain content of $\Delta\varepsilon_{yy}^{c-d}$ ($\Delta\varepsilon_{xx}^{c-d}$) bands shown in Figure 4.9(e) reflects the strain magnitude of the two chosen micro-DIC points and, in this sense, arbitrary.) These observations are consistent with the considerably more gradual operation of detwinning that is typically associated with the lack of the nucleation step in the reverse transformation [5], [47], [54], [63].

As shown over Figure 4.3(d), the regions that are overstrained in quadrant-I are delayed in recovering their strain and are still mildly compressive by the second zero-mean-strain crossing. The high-density occurrences of the remnant TTD bands coincide with the cross-banded zones in quadrant I. The fact that detwinning proceeds into quadrant III—meaning the recovery strain required to complete detwinning is higher than the strain imposed over the twin plateau) is consistent with previous results (e.g., [47]). Here, for the rolled material, we further note a spatial aspect: detwinning is primarily delayed at the band intersections, which are imposed higher strains at the end of the twin plateau.

The FW-TTD band propagation in quadrant I is a severe case of deformation heterogeneity with abrupt and cascaded activity. As such, the locations and family (+45° or − 45°) of the macroscopic bands clearly depend on stochastic factors (variations in microstructure, tolerance in sample dimensions, etc.). In this study, the macroscopic strain is extended to the −2% level in quadrant I such that the bands roughly cover the gage section, with only a small dormant region in the left bottom corner. Even in a scenario when the entire region is covered with bands, there is no sense of strain homogeneity, since the new bands superimposed over the first-layer are also heterogeneous [15]. Consequently, abrupt banded strain discontinuities will, in general, exist at the end of the twin plateau, while their exact pattern is bound to be sample-specific. The effect of over- and under-strained regions at the end of quadrant-I permeates through the entire cycle. Note, e.g., the dormant region in

the lower left corner that evaded compressive strain in quadrant-I (Figure 4.3b) still maintains a relatively more- tensile strain state at the end of the cycle (Figure 4.3j). The high level of hardening that is provided by tensile plasticity mechanisms, however, helps with a relative homogenization of the strain differentials particularly in quadrant III. A description that utilizes the dormant zone at the end of quadrant I is again useful. Once stress is reversed (quadrant II), this is the first region that is prompted to deform with tensile micromechanisms (primarily a combination of prism and basal slip). The high flow stresses of the tensile deformation limit the extent of further strain accommodation in this zone, prompting the rest of the material to accommodate strain by detwinning. By the first zero-mean-strain crossing (Figure 4.3d), the strain differential between this zone and the rest of the field is eroded significantly. By point e (Figure 4.3e), detwinning is exhausted completely (i.e., FW-TTD remnants are removed everywhere) and a large part of strain homogenization already has taken place.

Aside from stochastic effects, the operation of the TTD bands is clearly influenced by the details of the microstructure. As a reference point, it is useful to contemplate a hypothetical single crystal sample whose orientation matches the nominal orientation of the rolled sample that is best-suited to twin (i.e., $(\bar{1}2\bar{1}0)$ aligned with x-y and [0001] aligned with x). The monolithic twin band that would form in this single crystal would exhibit a transformation strain of $|\ \varepsilon_{yy}\ | = \ \varepsilon_{xx}\ \cong\ 6.5\%$ (half the transformation shear). While the 2-D kinematics of the FW-TTD bands are similar in nature, the nominal value of the band strain (~2.3%) in the rolled polycrystal falls well short of the single crystal value (6.5%). The drop itself is reasonable as the FW-TTD band entails a collaborative propagation of twin bands, describing an incomplete transformation of the region (Figure 4.8). The particular compactness of the band, however, is bound to depend on the exact microstructure. It is noted that TTD bands get more compact (higher-strain-content) with finer grain size [15], [22,23] and sharper textures [25]. The latter is also consistent with the fact that twin transmission is favored among closer orientations [22], [59]. For the rolled material, while the basal-type overall texture is typical, its degree is a process-dependent factor that is bound to influence the TTD-band compactness. Similarly, the non-45° micro-texture elements are typical, but their exact morphology is bound to show dependence on previous thermomechanical steps. This dependence will then translate to the strain localization levels

and the hardening that is imparted to these veins, and over reverse load, influence the next-wave tensile-twin-driven bands (Figure 4.10).

4.1.2. Extruded Sample

It is established with a multitude of experimental techniques (electron microscopy [22], [63], in situ neutron diffraction [4], [21], [54], [94], [95], acoustic emission [21], [63]) that the $\{10\bar{1}2\}\langle\bar{1}011\rangle$ tensile twin is the dominant deformation micro-mechanism for the extruded material under ED-compression. The pronounced spatial coordination of the intergranular twin activity has been more recently elucidated with microscopy [22] and quantitative strain mapping with DIC [15]. We exemplify this mode of deformation in our first point over the twin plateau where the sample is compressed to a nominal -0.5% strain. Over both the macro-DIC map shown in Figure 4.11(a) and the combination micro-DIC map shown in Figure 4.11(b) for this state, the essential character of this Lüders-like deformation [15], [22], [96] is apparent. The sample accommodates strain by discrete strain jumps in localized bands that make a boundary with the yet-undisturbed (dormant) material. In this regime, the increase in the overall deformation of the sample is associated with the advance of the deformed-material front into the dormant fields. For Magnesium alloys under a profuse-twinning load path, the abrupt strain increase in the localized regions is due to coordinated twinning [22], [59]. This essentially means twin formation in one grain making additional twin formation in its locality more likely.

While the macro-DIC map in Figure 4.11(a) crudely distinguishes the deformation band and the dormant fields, it represents near-homogenous strain fields inside the band—also true for macro-DIC studies in the literature [15], [24], [26]. As shown in Figure 4.11 (b), it is the immense resolution (over 4 x 10^6 data points) of the combination micro-DIC strain map that reveals the strain fields in the band are not monolithic. The make-up of the deformation band is rather constituted by an intertwining network of intergranular localization bands. With the limited display dimensions of the combination micro-DIC maps, their inherent resolution cannot be adequately represented with full-field maps. For this reason, we present a zoom-in to the strain field of a 150x150 μm^2 region of interest (ROI) in Figure 4.11c, overlaying the strain contours over the reference image of this locality with a degree of transparency. (This reference image corresponds to the initial (undeformed) state

and is provided in bare form in Figure 4.11d) The most notable intergranular localization bands in Figure 4.11c are marked by dashed lines to aid the eye and one notes a separation distance of about 2-3 grains between them. In likeness to the macroscopic measurement yielding a homogenized version of the strain fields in Figure 4.11b, the fields in Figure 4.11c present a homogenized version of the submicron-scale intragranular strain fields [18], as expected from the multitude of length-scales that govern the material behavior. In summary, the immense length-scale band captured by the micro-DIC combination maps start from an order below the crystallite-scale (on average, about 25 data points per grain) and extend to the full macroscopic length-scale. Commensurate with this precise length-scale band, the findings here are focused on the intergranular strain fields and their spatial-networking characteristics, elucidated with full-field statistics over ~10^5 grains.

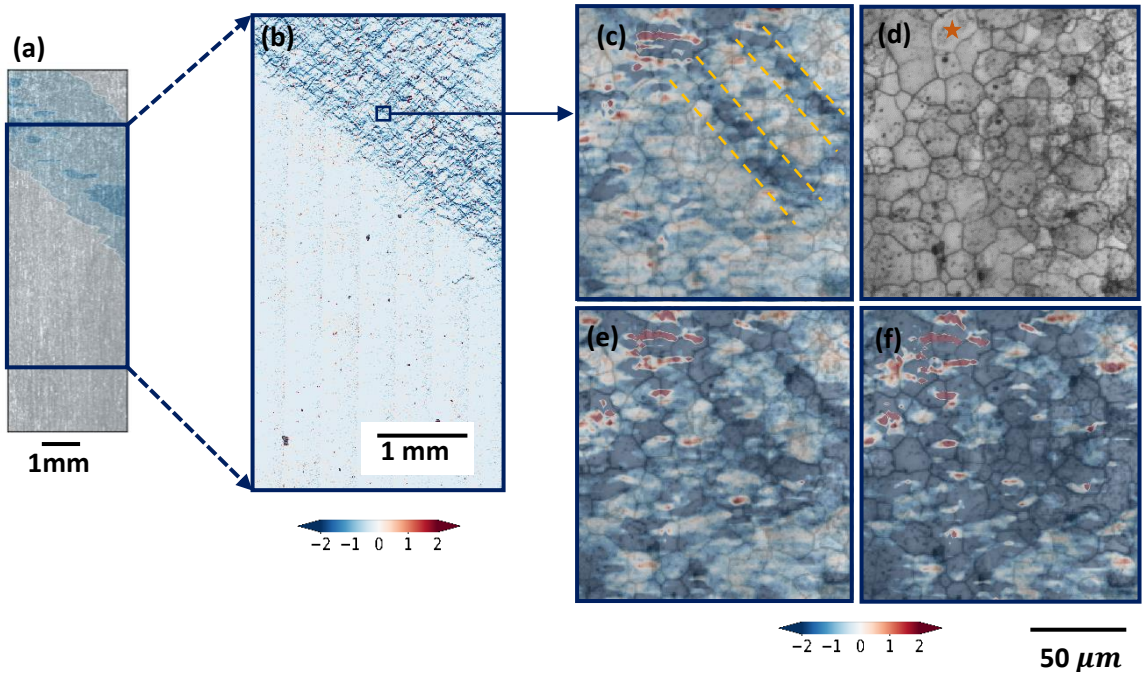

Figure 4.11. (a) Macro-DIC and (b) combination micro-DIC axial strain maps at $\bar{\varepsilon}_{yy} \cong$ -0.5%. A 150x150 μm^2 region is zoomed in to show the crystalline scale resolution of the micro-DIC map at effective strains of (c) $\bar{\varepsilon}_{yy} \cong$ 0.5%, (e) $\bar{\varepsilon}_{yy} \cong$1.2%, and (f) $\bar{\varepsilon}_{yy} \cong$ 2%. The strain contours are shown with a level of transparency of the reference image of this locality whose bare form is provided in (d).

The combination micro-DIC maps are collected in-situ at progressive load points over a non-monotonic load path. The first portion of this path is shown on the stress-strain curve at the bottom of Figure 4.12. Accordingly, the sample is first imposed compressive strain up to a nominal value of -2% followed by an unload and then stretched back to the same gage length (zero sample-average strain). The latter segment (points *i-l*) naturally requires the application of the reverse (tensile) load. Figure 4.12 (a-l) show the combination micro-DIC axial strain maps for every corresponding point *a-l* marked on the stress strain curve.

The initial compressive portion of the stress strain curve (points *a-h*) shows the well-known twin plateau that entails strain accommodation at a near-constant stress level. Figure 4.12 (a,b) maps for points *a* and *b* depict the initial advance of the Lüders-like deformation over the maiden material where part of the field is virtually undeformed. The average strain content of these bands is limited (comparison to rolled material and further discussion in Section 4.2) and thus they spread to the volume rapidly. By point *c* (average -1.1% strain), the entire gage section is covered by intergranular strain bands as shown in Figure 4.12 (c). This doesn't, however, mean the activity of the bands is homogenous over the full-field and the denser activity below the middle section of the sample is noticeable in Figure 4.12 (c). With each strain increment after this point over the twin plateau, strain structures intensify and homogenize. At the local scale, this process is exemplified in Figure 4.11(e) and (f) that corresponds to load points *d* and *h* in Figure 4.12.

Once the load is reversed, the compressive strain localization network that is intensified until point *h* is observed to homogeneously release strain as shown over the maps in Figure 4.12 (i-k). Point *l* is nominally the point where the sample is stretched back to the zero-average strain. The fields have very mild tensile strain at this point (0.1% average) reflected in the light red background of Figure 4.12 (l). More importantly, the strain fields at point *l* appear to be largely homogeneous. In particular, the compressive strain localization network that still was visible in the previous load *k* is fully decayed at this point. To help with the quantitative rationalization of the observations on Figure 4.12, Table 4.1 presents the average transverse and axial strains ($\bar{\varepsilon}_{xx}$, $\bar{\varepsilon}_{yy}$) and standard deviations of transverse and axial strains ($\delta\varepsilon_{xx}$, $\delta\varepsilon_{yy}$) both computed over the entire combination micro-DIC field. The full-field maps of transverse strains, ε_{xx}, provide a largely similar portrayal the intergranular localization networks (of course in the opposite strain sense) and are excluded for brevity. With their field-average value presented in Table 4.1, a column for apparent Poisson's ratio,

$\bar{\nu} = -\bar{\varepsilon}_{xx}/\bar{\varepsilon}_{yy}$ is also included. (Poisson's ratio is an elastic constant and the added term "apparent" stands for the computation of the strain ratio outside the elastic region.) Plasticity is volume-preserving and $\bar{\nu}$ takes the value of 0.5 when plastic processes are effectively isotropic. The values on the $\bar{\nu}$ column over the twin plateau are consistent with this value by less than a 4% deviation for all points *c*-*h*. (The slightly lower values at points *a* and *b* are reasonable since they contain plastically dormant fields.) $\bar{\nu}$=0.5 is consistent with the extruded sample loaded along the ED since the texture ordains transverse isotropy about this axis [15].

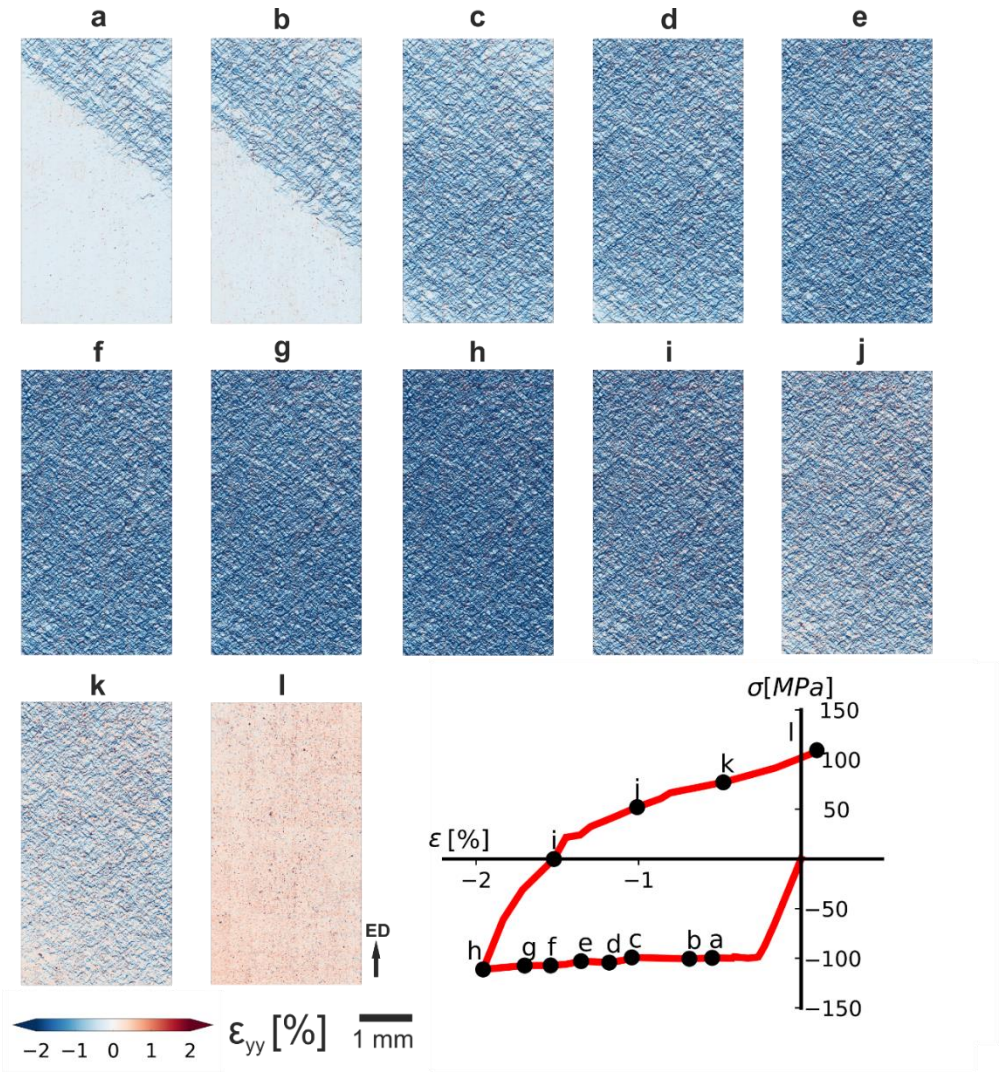

Figure 4.12. (a-l) Micro-DIC combination axial strain maps for load points a-l marked on the stress-strain curve on the bottom right.

Full-field standard deviations ($\delta\varepsilon_{xx}$, $\delta\varepsilon_{yy}$) presented in Table 4.1 are first-order measures of strain heterogeneity and they are sensitive to the measurement length-scale. (Proper field-averages, on the contrary, are mathematically independent of the measurement length scale.) The standard deviations in the current crystallite-scale measurement is much higher than the standard deviation in the macro-DIC measurements (e.g., 3-4 times higher than those presented in [15]). Here, we find that the standard deviation in the transverse and axial strains are comparable ($\delta\varepsilon_{yy}$ only slightly higher than $\delta\varepsilon_{xx}$) and they crudely scale with the effective strain levels as shown in Figure 4.13. In the first segment of the load path depicted in Figure 4.12, the standard deviations rise over the twin plateau making a maximum at point *h*. After point *i* when the load is reversed and increased in tension, the standard deviations exhibit a reverse trend and decay near linearly. Interestingly, the slope of this decay appears equivalent to the slope of the rise over the twin plateau. Checking over Table 4.1, one finds that $\delta\varepsilon_{yy}$ drops to a minimal 0.5% at point *l*, supporting the visual observation of relative homogeneity in Figure 4.12 (l). On Figure 4.13, the horizontal separation between the two linear trends of the twin plateau (points *a*-*h*) and the tensile load segment (points *i*-*l*) seem to be explained by the release of elastic strains during the *h*-*i* unload. We note, despite its notorious plastic anisotropy, Magnesium is near elastically isotropic. Thus, the recovered elastic strains are virtually homogenous, particularly in contrast to the plastic strains that localize over an intergranular network. Thus, the released elastic strains during the unload from points *h* to *i* essentially only shift the strain distributions. This means average values are decreased but the standard deviation of the strain fields is preserved.

In the first portion of the load path depicted on Figure 4.12, we have presented that (i) the intergranular strain localization networks spread and then intensify over the twin plateau and (ii) after load reversal, these strain fields are virtually recovered as the sample is stretched back to zero nominal strain. In the next stage of the loading shown over Figure 4.14, the tensile load on the sample is first increased to impart an appreciable degree of plasticity in the sample, followed by an unload (point n) and a final compression stage. Since the tensile twin is a unipolar mechanism, it is suppressed under tension. Thus, in the tensile part of this segment from point l to m, it is well known (e.g., [10]) that the material deforms with slip plasticity and exhibits rapid hardening. The stress level is 182 MPa (much larger

than the 100 MPa level over the twin plateau) at the maximum tension point of this experiment (point m, strain average about 1.1%).

Table 4.1. Average transverse and axial strains ($\bar{\varepsilon}_{xx}$, $\bar{\varepsilon}_{yy}$), apparent Poisson's ratio ($\bar{\nu} = -\bar{\varepsilon}_{xx}/\bar{\varepsilon}_{yy}$), standard deviations of transverse and axial strains ($\delta\varepsilon_{xx}$, $\delta\varepsilon_{yy}$) derived from the full micro-DIC combination fields for load points a-l in Figure 4.12 . $\bar{\nu}$ is not meaningful after load reversal and not reported for points i-l. All strain quantities shown in percentages.

Load point	$\bar{\varepsilon}_{xx}$	$\bar{\varepsilon}_{yy}$	$\bar{\nu}$	$\delta\varepsilon_{xx}$	$\delta\varepsilon_{yy}$
a	0.195	-0.426	0.457	0.567	0.591
b	0.274	-0.589	0.464	0.818	0.835
c	0.579	-1.110	0.521	1.107	1.193
d	0.659	-1.294	0.509	1.251	1.331
e	0.764	-1.482	0.515	1.379	1.467
f	0.860	-1.700	0.506	1.540	1.600
g	0.962	-1.865	0.515	1.642	1.701
h	1.079	-2.110	0.511	1.801	1.820
i	0.919	-1.683	-	1.773	1.773
j	0.660	-1.147	-	1.440	1.504
k	0.355	-0.554	-	0.997	1.034
l	0.023	0.0962	-	0.550	0.517

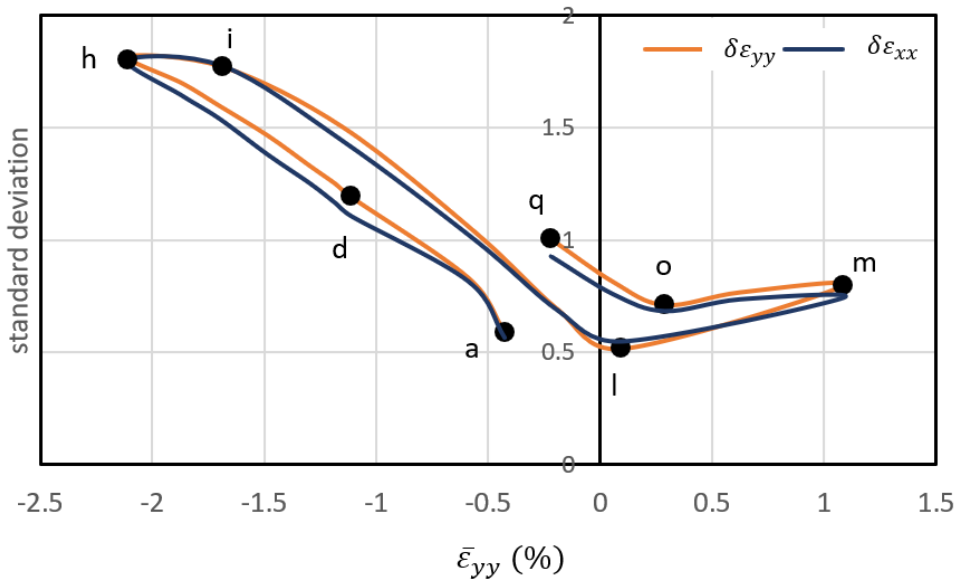

Figure 4.13. Standard deviation of transverse and axial strains ($\delta\varepsilon_{xx}$, $\delta\varepsilon_{yy}$) derived from full-field combination micro-DIC maps plotted against the average axial strain $\bar{\varepsilon}_{yy}$.

Over the unload to point *n*, a notable elastic release is observed (given the limited elastic moduli of Magnesium and coming down from a high stress) that is immediately apparent in the visual comparison of point-*n* and point-*m* strain maps in Figure 4.14. The strain spread as represented by the standard deviations ($\delta\varepsilon_{xx}$, $\delta\varepsilon_{yy}$), however, are nearly unaffected during the unload as shown on the point-*m* and point-*n* rows of Table 4.2. (The reasoning for the stability of the strain spread upon unloads has been provided previously for the *h*-*i* unload.) A network of plastic strain localizations is apparent at points *m* and *n*. Nevertheless, judging by the quantitative values of ($\delta\varepsilon_{xx}$, $\delta\varepsilon_{yy}$) for these points, the overall strain fields are more homogeneous in this slip-plasticity regime compared to the deformation over the twin plateau and its reversal. These values for point *m* and *n* remain under 0.8% showing a modest increase coming from point *l*. This argument is more evident in Figure 4.13 where the increase-rate of the standard deviations from point *l* to point *m* is considerably smaller than the slopes observed among points *a*-*h* or *i*-*l*.

After another load reversal to the final load-stage that is named second compression here, one sees a degree of recovery in the tensile strain structures crudely until point *o*. Aside from the visual evidence in Figure 4.14 (o), this stage is accompanied by a noticeable decrease in the standard deviations from point *n* to point *o* (see Table 4.2). After point *o*, reverse yielding starts judging by the stress-strain curve (Figure 4.14) and the standard deviations once more switch to a heavily increasing trend as shown in Figure 4.13. What we visually observe over the combination micro-DIC maps of points *p* and *q* is an introduction of a second wave of compressive strain localization structures that stand out with their blue color. These are introduced among the permanent tensile structures and quickly lead to a polar strain distribution with discrete tensile and compressive elements. For local inspection, we consider the ROI that we previously introduced (Figure 4.11) for point-*q* strain fields. This field is again overlaid on the reference-configuration microstructure and shown in Figure 4.14 (lower left). The polarity of the strain fields at point-*q* is also reflected to the large spread in its axial strain histogram (Figure 4.14, upper left).

Even by the characteristic shape of the stress-strain curves in Figure 4.12 and Figure 4.14 that show a plateau under first-compression, a huge Bauschinger effect on the reverse load, heavy hardening with further tension into positive strains and another plateau under the second compression, the dominant micro-mechanisms in each segment are very well

known from the extensive field literature (e.g., [7], [15], [41], [54], [80]). The material first undergoes twin-dominated deformation (points *a*-*h*), then releases strain predominantly by detwinning (points *i*-*l*), incurs tensile strain by slip plasticity (points *l*-*m*) and undergoes a second twin-dominated deformation from point *o* to the final point of the experiment *q*.

Nevertheless, twinning activity can occasionally create contrast under bright-field microscopy and become visible on the combination micro-DIC images recorded over the field. Figure 4.15(b) exemplifies the twins evident in the micro-DIC images at the final point of the twin plateau. (The shown region is a subfield of the ROI chosen earlier and the central grain is marked with an asterisk in Figure 4.11(d).) Consistent with detwinning, all these structures are found to disappear by point *l* as shown in Figure 4.15(c).

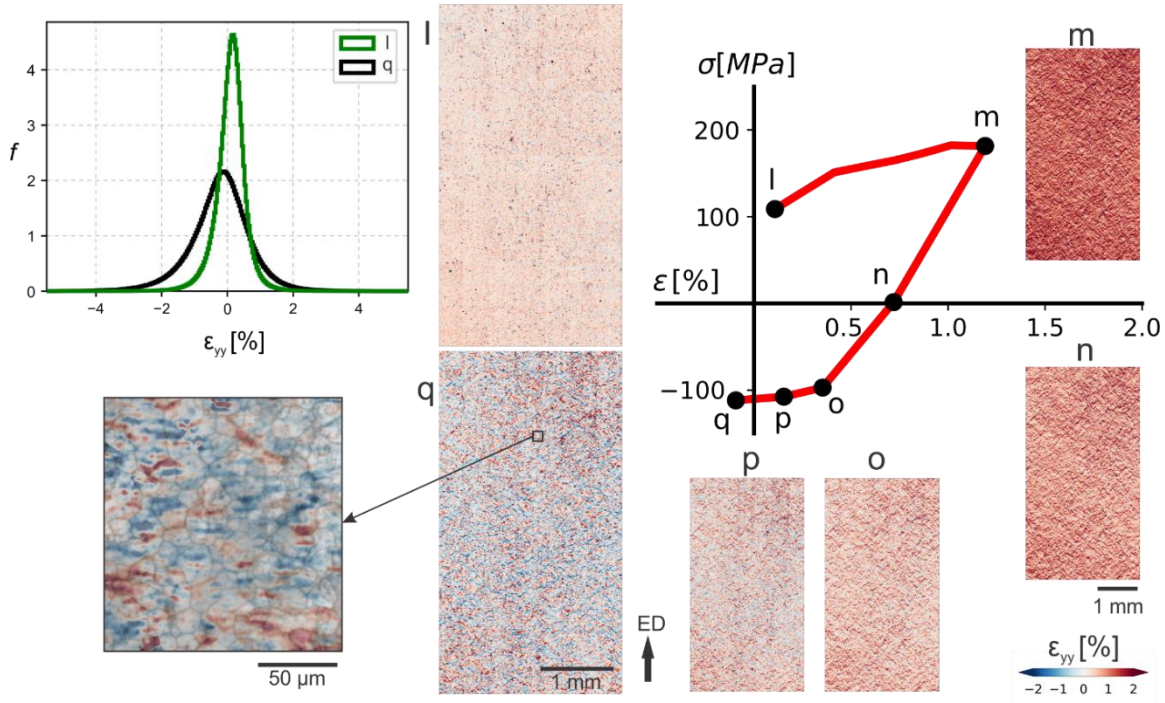

Figure 4.14. (l-q) Micro-DIC combination axial strain maps for load points l-q marked on the stress-strain curve. Comparative axial strain histograms for pints l and q are provided on the left-top where f stands for percent frequency.

The twinning and detwinning processes are visible with a unique signature in Figure 4.13 as well where the standard deviation of the strain fields develops (on twinning) and

decay (on detwinning) with the same slope. A rise with a similar slope at the inflection point at *o* signifies the dominant operation of the tensile twin again under the second-compression.

Table 4.2. Average transverse and axial strains ($\bar{\varepsilon}_{xx}$, $\bar{\varepsilon}_{yy}$), apparent Poisson's ratio ($\bar{\nu} = -\bar{\varepsilon}_{xx}/\bar{\varepsilon}_{yy}$), standard deviations of transverse and axial strains ($\delta\varepsilon_{xx}$, $\delta\varepsilon_{yy}$) derived from the full micro-DIC combination fields for load points l-q. All strain quantities shown in percentages.

Load point	$\bar{\varepsilon}_{xx}$	$\bar{\varepsilon}_{yy}$	$\delta\varepsilon_{xx}$	$\delta\varepsilon_{yy}$
m	-0.428	1.083	0.744	0.797
n	-0.291	0.624	0.737	0.769
o	-0.187	0.288	0.685	0.712
p	-0.065	0.058	0.760	0.815
q	0.087	-0.220	0.929	1.007

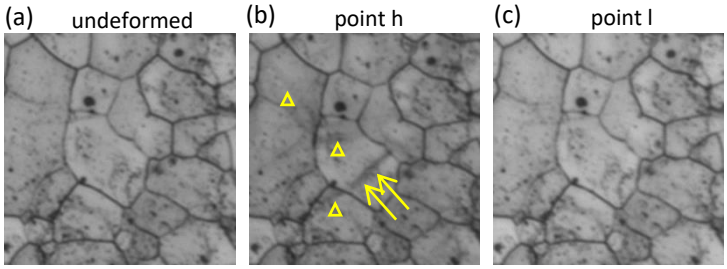

Figure 4.15. Micrographs of a small (70x70 μm^2) region of interest at (a) the reference(undeformed) state, (b) point h at the end of the twin plateau, (c) point l at the end of detwinning. The most obvious twin contrast that formed at point h is marked with arrows. Some other traces are marked with triangles. All these traces disappear in part (c).

The fundamental complexity with the tensile-twin-dominated deformation regime in wrought Magnesium is the fact that Magnesium is also plastically soft. Ascertained numerously with polycrystalline models and, e.g., neutron diffraction measurement, dislocation slip (particularly the very easy basal slip) always accompanies the forming tensile twin networks over the twin plateau (see, e.g., [54], [80] for the micro-mechanism activity rates over the twin plateau of the extruded material). Hence, the intergranular networks that form and spread over the twin plateau (Figure 4.12 (a-h)) are to be interpreted

as the collaboration of coordinated twin activity and accompanying slip. The culprit of heavy strain localization, however, both at the intergranular and macroscopic scales is the tensile twin. We will discuss the Lüders-like strain evolution with much higher detail in the next subsection.

As we have noted previously, the intra-granular resolution with optical-microscopy DIC is limited and it is the role of SEM-DIC [18] to make individual investigations of micro-mechanism activities. (We remind that the DIC strain resolution is 1-2 orders coarser than the image resolution shown in Figure 4.15, since the technique tracks subsets.) The role of this study is rather to resolve the intergranular strain localization network but over the full-field of the sample, providing immense statistics for these patterns and highlighting their long-distance coordination. Resolving the make-up of Lüders-like strain bands is clearly very important (recall Figure 4.11(a,b)). Another emphasis point with regard to the significance of the measurements is point *q*. Here, distinct tensile and compressive strain patterns are resolved with combination micro-DIC (Figure 4.14(q)) whereas these fields are simply averaged out in a macro-DIC observation, giving the appearance of null-strain fields (not shown but described for brevity). The investigated length-scale band is also very relevant for better development/calibration of the crystal-plasticity models since the constitutive framework of these models have a limited intra-grain resolution.

In this section, we discuss the spatial character of the tensile-twin-driven localization bands and their progression over the extruded sample with comparisons to the analogous phenomenon for rolling texture [15], [84]. To investigate the progression of the bands over the maiden material, we bring up the early load points *a* and *b* again in Figure 4.16(a,b) but, in addition, present the strains that are accommodated in between these two points in Figure 4.16 (c). As explained before, these strains incurred in the *a*-*b* interval are denoted $\Delta\varepsilon_{yy}^{a-b}$ and correspond to the DIC calculation among the images of these two load points. Note, so far in the text we used a diverging red-blue colormap that emphasizes *strain senses* (see, e.g., Figure 4.14(q) to see its benefits). In the Figure 4.16 to Figure 4.18 of this subsection, we make a functional switch to a colormap that better differentiates the *magnitudes of compressive strains*.

To guide the eye for the propagation of the strain bands, three sets of dashed lines are drawn on each map in Figure 4.16. The red and purple lines mark the old (point-*a*) and the new (point-b) boundaries of the deformation band in the direction that it advances. The black dashed trace, on the other hand, draws the other boundary of the domain that has been deformed by point *a*. This domain that is enveloped by red and black traces is also marked with an asterisk "*". Now, we bring analogous data from a rolled Magnesium AZ31 sample of comparable grain size (13 μm average) in Figure 4.17 at an equivalent stage over its twin plateau. While the data presented in Figure 4.17 is original and used only in this manuscript, we have previously investigated the twin-plateau behavior of the rolling texture with this technique and the reader is referred to [15], [84] for further details on the deformation of the rolled material. Here, our purpose is to enable a useful comparison with the extruded material. Accordingly, in Figure 4.17 (a-c) we add the red, purple and black boundaries with analogous definitions to Figure 4.16 for the major +45° band in the rolled sample. (For the extent of the arguments here, ignore the minor interaction with the smaller -45° band that appeared in the lower left corner at point *b*.)

Comparing Figure 4.16 and Figure 4.17 for the specifics of Lüders-like propagation of the tensile-twin-driven bands in the extruded and rolled samples, we first note that the intergranular strain mesh in the make-up of the rolled-material band is significantly more compact than that of the extruded material. This factor is visible in all maps in Figure 4.16 and Figure 4.17. The second factor is more subtle: The incremental strain advance ($\Delta\varepsilon_{yy}^{a-b}$) for the band of the rolled material (Figure 4.17 (c)) is constrained to the *expansion region* between red and purple boundary lines. More clearly, there is no sign of activity in the previous domain of the band that is marked with "*" where $\Delta\varepsilon_{yy}^{a-b}$ fields appear to be decidedly null on Figure 4.17 (c). Conversely, with Figure 4.16 (c) considered through this argument, one notes that while the expansion region accommodates the highest levels of strains, the previously deformed fields marked with "*" also incur considerable strains.

Combined with the first observation, one can argue that the extruded material forms diffuse localization networks, and these are *packed* with more activity in addition to the advance into the dormant fields. The rolled material (Figure 4.17) bands are already formed with a much denser network and the strain accommodation only occurs with new advances of the band front with sharp boundaries.

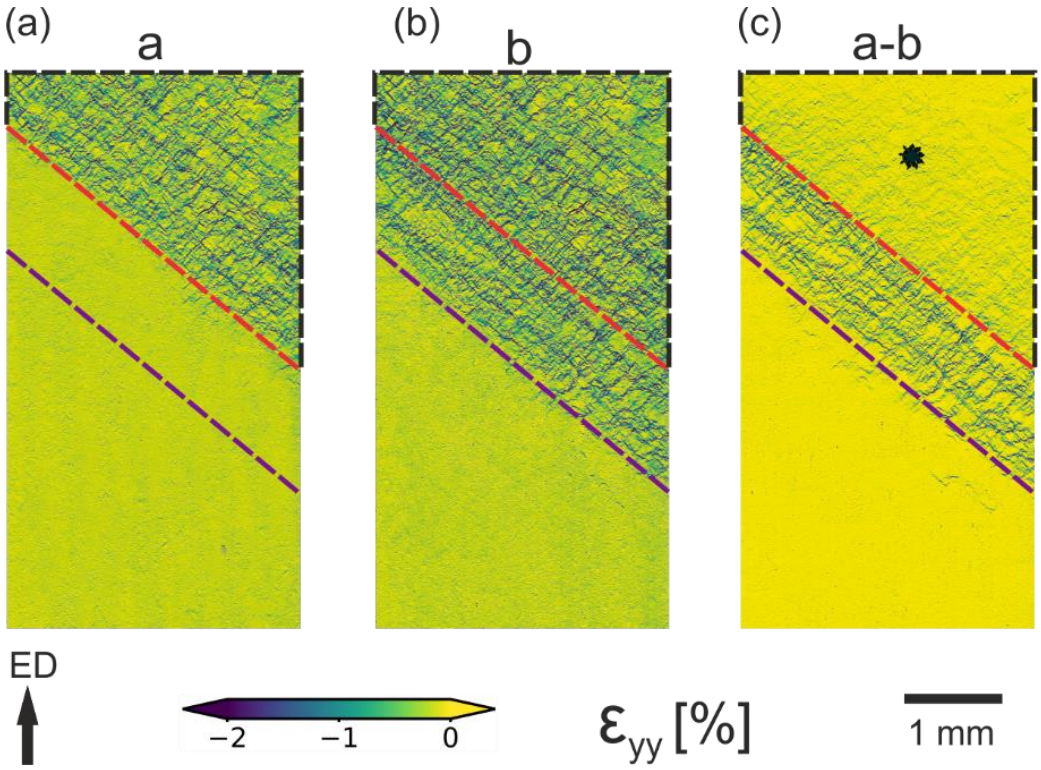

Figure 4.16. For the extruded sample of the study, combination micro-DIC strain maps for (a) point a (full-field average -0.42%), (b) point b (-0.59%), (c) strains accommodated in the a-b interval.

For the extruded material, similar arguments remain valid after the gage volume is covered with the strain network (roughly by point c, Figure 4.12). With the milder average band strains, this coverage happens rapidly but as noted earlier, the fields are not homogeneous. The new localization networks preferentially fill in the regions where the intergranular strain networks are more diffuse. Note for example from Figure 4.12 (c) that the strain network is more diffuse at the top section of the point-*c* strain fields and $\Delta\varepsilon_{yy}^{c-d}$ strains shown in Figure 4.18(a) are preferentially concentrated at the top. Then, in the next increment d-e, the new wave switches to the bottom (Figure 4.18 (b)) and, in the next, again to the top (Figure 4.18 (c)), and so on (Figure 4.18 (d,e)). So, the regions of the strain advances seem to relocate but note their distributions are fuzzy in nature, lacking sharp boundaries.

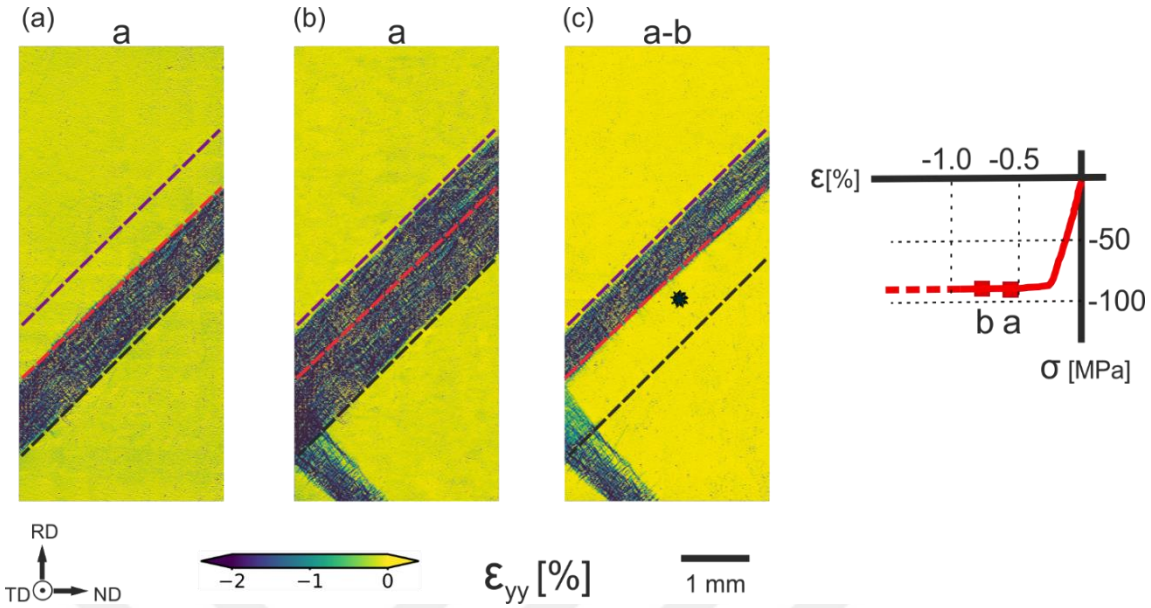

Figure 4.17. For the complementary rolled sample, combination micro-DIC strain maps for (a) point a, (b) point b, (c) strains accommodated in the a-b interval. Macroscopic strains for both points and the stress level of the twin plateau are shown on the right.

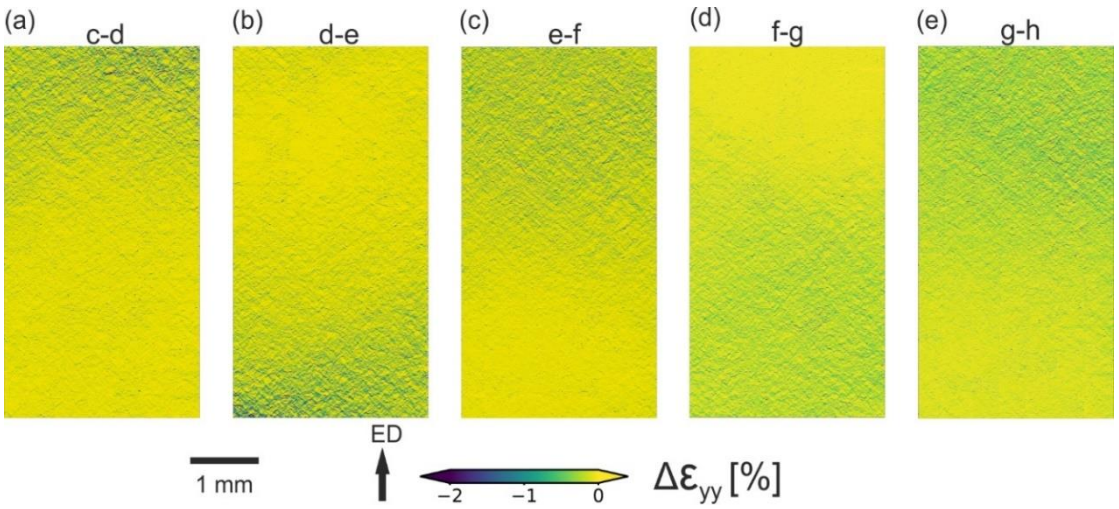

Figure 4.18. Incremental strain maps over the first twin plateau that describe strain accommodation between load points (a) c and d, (b) d and e, (c) e and f, (d) f and g, (e) g and h. See Figure 4.12 for the location of these points on the stress-strain curve as well as their absolute strain maps.

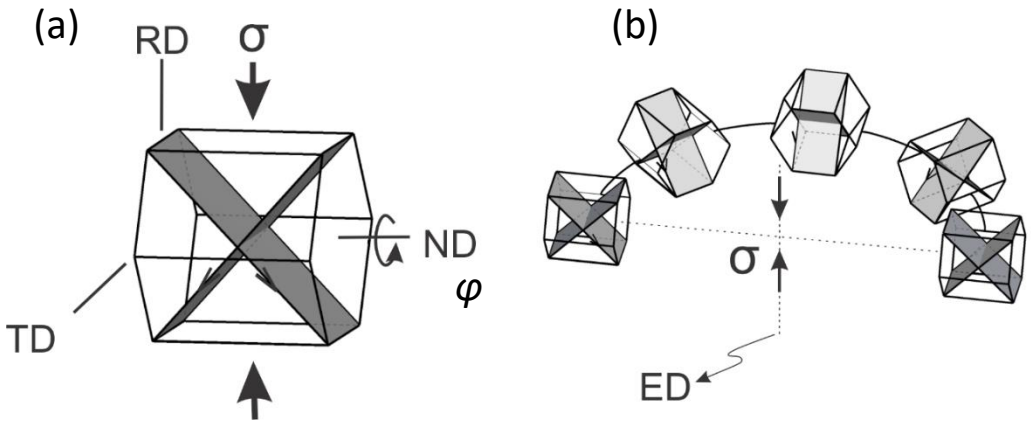

Figure 4.19. Unit cells that sketch the major elements of (a) rolling, and (b) extrusion textures. The operative (highest resolved shear) $\{10\bar{1}2\}\langle\bar{1}011\rangle$ tensile twin system pair is indicated in each unit cell. Note twinning is unipolar and these systems only operate under compressive stress (σ) along (a) RD and (b) ED. This σ-sense is indicated with arrows in the illustrations.

Conversely, the rolled material has been found to accommodate strain with sharp bands even after the spread of the deformation to the entire surface [15]. Figure 4.18 illustrates why the rolling and extrusion textures yield vastly different degrees of strain heterogeneity, depicting unit cells for most abundant orientations in each texture. The operative (highest resolved shear stress) tensile twin pair is also marked inside the unit cells. In the c-axis-aligned texture of the rolled material, the texture can be shown by the single unit cell in Figure 4.18 (a) (note the inclusion of the angle φ that marks the random probability of finding orientations as this unit cell is rotated about its c-axis; due to symmetry this is a ±30° interval). The coordinated twinning activity in the rolling texture is remarkably centred about the twin pair shown in this nominal orientation, creating on-average two-dimensional networks. This means an effective alignment of all shear activity inside the band with the RD-ND plane [15], [26], [84], also implying an effective symmetry of axial and transverse strains with $\bar{\nu}\sim1$ measured on the RD-ND plane (also necessarily ordaining $\bar{\nu}\sim0$ on the RD-TD plane [15]). Conversely, while the c-axis-distributed texture of the extruded material depicted in Figure 4.18 (b) is sharp, the twin activity is axisymmetric, noted over the operative twin pairs in each unit cell. (Also, recall $\bar{\nu}\sim0.5$) What we directly show in this paper is that the broader distribution of operative twin orientations actually instigates a more diffuse localization network. The initial network at any locality, however, is augmented

further as more strain accommodation is prompted over the twin plateau (Figure 4.16(c), Figure 4.18).

To provide quantitative detail on these observations, Figure 4.20 provides comparative strain histograms. The first row considers the evolution of the strain fields over the first twin plateau and Figure 4.20 (a) and (b) present axial and transverse strain distributions, respectively. The data population of these histograms are chosen as the material points of the band-expansion that occurs over interval *a*-*b*. Thus, the first histogram $\Delta\varepsilon_{yy}^{a-b}$ depicts the strain distribution in the expansion zone between red and purple lines in Figure 4.16 (c). The shown $\Delta\varepsilon^{a-b}$ distributions are also representative for point-*b* absolute strain distributions in the selected region (ε^{b} histograms not shown for clarity) aside from the fact that the latter is shifted by the elastic strains at point *b*. ($\Delta\varepsilon_{yy}^{a-b}$ is stripped of the elastic strains since *a* and *b* are under the same stress over the twin plateau. Note the elastic strains explain the slightly darker background of Figure 4.16 (a,b) compared to Figure 4.16 (c).) For consistency in sampling, we utilize the same material points for the histograms of the rest of the loads (points *c*, *f* and *h*). For these, however, this band of material is simply a representative region of abundant statistical significance (still containing close to 10^6 data points). In other words, the full-field histograms for *c*, *f* and *h* are largely equivalent to those shown in Figure 4.20.

The gradual broadening trend of the histograms in Figure 4.20 (a,b) demonstrate the augmentation of the strain fields over the twin plateau as the strain is increased. Note that, as this happens, maximal strains also increase, e.g., in the axial strain results, from the -4% level to the -8% level. Furthermore, as expected from the very close values of $\delta\varepsilon_{xx}$ and $\delta\varepsilon_{yy}$ in Table 4.1, the breadth of the transverse strain histograms in Figure 4.20 (b) are found comparable to those of the axial strains in Figure 4.20 (a).

In Figure 4.20 (c,d) we reproduce $\Delta\varepsilon_{ext}^{a-b}$ (the band-advance strains over the maiden material) and ε_{ext}^{h} (highest strains over the twin plateau) for our extruded sample to put it in reference of the $\Delta\varepsilon_{rolled}^{a-b}$ of the rolled material. The averaged axial strains for these populations are computed to be $\overline{\Delta\varepsilon}_{ext}^{a-b} = -0.49\%$, $\bar{\varepsilon}_{ext}^{h} = -2.11\%$ for the extruded material and $\overline{\Delta\varepsilon}_{rolled}^{a-b} = -2.02\%$ for the rolled material. There are two meaningful comparisons here. The first is $\overline{\Delta\varepsilon}_{rolled}^{a-b}$ versus $\overline{\Delta\varepsilon}_{ext}^{a-b}$, the comparison of the band-expansion

strains over the maiden material. The former is factors higher supporting the visual comparisons of Figure 4.16 and 8. The other builds on the fact that $\bar{\varepsilon}_{ext}^{h} \simeq \overline{\Delta\varepsilon}_{rolled}^{a-b}$. In words, it is the comparison of the rolled and extruded material grain-scale strain distributions in the twin-dominated deformation when mean strains on the *deformed* fields are equivalent. Before, comparing the strain distributions of these two cases (over Figure 4.20 (c,d)) that have near-equal averages, let us note for the rolled material that its histograms do not intensely broaden with deformation as shown for the extruded material in Figure 4.20 (a,b). The distributions for the rolled material remain essentially identical over the banded regions as they cover the gage volume. (The reader is referred to our corresponding study for the rolled material [84]. Yet, we have already demonstrated that strain accommodation doesn't contribute to the already-deformed regions— the lack of activity in the asterisk region on Figure 4.16 (c). This implies that the deformed-field histograms do not broaden.)

We find on Figure 4.20 (c,d) that for the same mean-strain (*that is, we should note, about the Lüders strain of the rolled material*), the extruded material shows higher strain heterogeneity than the rolled material in the deformation bands. Thus, the strain heterogeneity of the rolled material can supersede that of the rolled material at this length-scale, though the rolled material presents a much sharper strain heterogeneity at the macroscopic length-scale.

A final note in this comparison is due for the pronounced separation of the transverse strain peaks ε_{xx}^{h} and $\Delta\varepsilon_{xx}^{a-b}$ (rolled) compared to the more closely-overlapping ε_{yy}^{h} and $\Delta\varepsilon_{yy}^{a-b}$ (rolled). For the rolled material with essentially planar shear $\Delta\varepsilon_{xx}^{a-b}$ is roughly the mirror image (the negative) of $\Delta\varepsilon_{yy}^{a-b}$. For the transversely isotropic extruded material, on the other hand $\bar{\varepsilon}_{xx}^{h} \simeq -0.5\bar{\varepsilon}_{yy}^{h}$ is enforced. That means the center of mass of ε_{xx}^{h} is around +1% whereas the center mass of $\Delta\varepsilon_{xx}^{a-b}$ (rolled) is around +2%. In this section, we finally emphasize the particular scientific value of the length-scale-bridging (with micro-DIC area scan) when it comes to Lüders-like deformation.

In these deformation regimes, if one visualizes a routine micro-DIC test involving a single frame (e.g., consider the single frame) the entire information of the band coordination is missed by the observer. In this frame, the strains would be found to rise and fall (e.g.,

follow the strains of this small region over Figure 4.12), with the observer having no notion of the long-distance coordination of the strain structures.

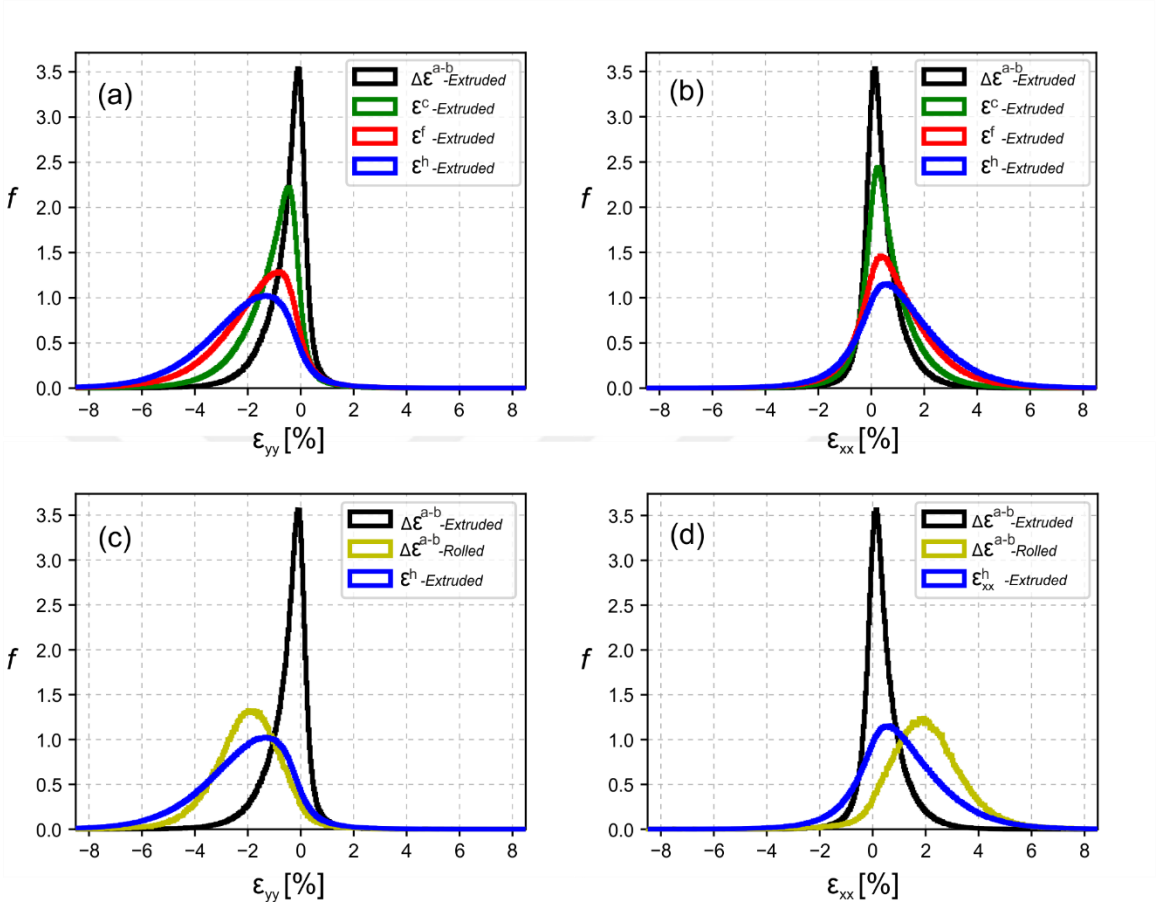

Figure 4.20. (a,b) For the extruded material of the study (a) ε_{yy} and (b) ε_{xx} histograms for load interval a-b, and load points c, f, and h over the twin plateau. The data population belongs to the material points in the band expansion zone in Figure 4.16(c). (c,d) The limiting histograms in part (a) put in perspective of the rolled-material characteristic histogram in twin-driven bands (see Figure 4.17).

Figure 4.14 demonstrates, after a degree of tensile slip plasticity is imparted to the sample (point *m*) and the load is reversed, the twin-driven intergranular bands again come into the mix at a stress akin to the stress level of the first twin plateau (~100 MPa). These are clearly distinguished with their compressive senses (blue in Figure 4.14 (p-q)), however they now appear on the remnant strains from the tensile plasticity stage that appear red in the same maps. The result is a polar strain field at point *q* that is put in contrast of Figure 4.14 (l) that belongs to the previous nominal zero-strain crossing after twinning and

detwinning stages. The much lower strain heterogeneity of point-*l* in the strain maps is also presented in the accompanying axial strain histogram.

While the mechanism of the polar strain formation after the second compression is clarified in this picture; the extent of the strain broadening when the sample is compressed to zero mean-strain will clearly depend on the tensile plastic strain imposed in the previous quadrant. Higher tensile pre-strain is naturally expected to lead to higher strain broadening. As for the second wave of compressive strain structures, we note that they appear essentially over the entire field, not demonstrating the Lüders-like propagation (Figure 4.16) observed at the beginning of the first twin plateau. It can be speculated that the remnant tensile strain localizations have a homogenizing effect and the second-wave twinning events instigate wherever they can within this pre-existing network.

4.2. Numerical Results

RVEs are run with rolling texture as well as extruded texture. In this effort, we will primarily evaluate the adequacy of the crystal plasticity FE DAMASK Magnesium engine with macroscopic (RVE-averaged) parameters. The first comparison point is the sensibility of the stress-strain curve over the cyclic load paths considered in this study. The second point of comparison is the anisotropic strain ratios (apparent Poisson's ratios) under the twinning regime. To recall, rolled Magnesium produces apparent Poisson's ratios of 1 and 0 on orthogonal RD-ND and RD-TD faces, respectively whereas the transversely isotropic extruded material virtually satisfies 0.5 on both faces. The second tier of looking for consistency between model and experimental strain fields is the agreement level of the histograms.

Core elements DAMASK pre-processing and formulations have been provided in Section 3.4. The values that are utilized in these analyses are provided in Table 4.3 and are changed from their original values to fit the stress first-compression leg of the stress strain curve as best as possible. These values are kept common for both cases since the grain sizes are very much comparable (11 and 14.5 μm for rolled and extruded, respectively). In the following grain sizes for both models are kept identical (at 11 μm. Functionally what is

important is that the grain to domain size have been kept identical since DAMASK constitutive formulation is not nonlocal but a classical scalable model.)

For the numerical simulation the number of active mechanisms could be controlled by in the configuration file. Here in this study, 3 basal slip, 3 prismatic, 6 pyramidal <a> and 6 second order pyramidal <c+a> families are considered. Also, only 6 tensile twin variants are considered since compressive twin has not been observed in these materials even in the load sense that favor them (i.e., tension along RD and ED). The DAMASK parameter file employs the compressive twins by default, so the file has been modified to deactivate them. The variants of all considered deformation systems are listed in Table 4.4.

Table 4.3. Elastic and plastic parameters implemented in constitutive equations in section 3.4 for modeling HCP Mg. data are obtained from [28].

Elastic constants			**Slip related parameters**			**Twin related parameters**		
Parameter	Value	unit	Parameter	Value	unit	Parameter	Value	unit
$\boldsymbol{C_{11}}$	59.3	GPa	$\xi_{0,basal}$	10	MPa	$\xi_{0,T1}$	40	MPa
$\boldsymbol{C_{33}}$	61.5	GPa	$\xi_{\infty,basal}$	40	MPa	h_0^{tw-tw}	50	MPa
$\boldsymbol{C_{44}}$	16.4	GPa	$\xi_{0,prism}$	55	MPa	h_0^{tw-s}	150	MPa
$\boldsymbol{C_{12}}$	25.7	GPa	$\xi_{\infty,basal}$	135	MPa			
$\boldsymbol{C_{13}}$	21.4	GPa	$\xi_{0,pyr\langle a\rangle}$	60	MPa			
			$\xi_{\infty,pyr\langle a\rangle}$	150	MPa			
			$\xi_{0,pyr\langle c+a\rangle}$	60	MPa			
			$\xi_{\infty,pyr\langle c+a\rangle}$	150	MPa			
			h_0^{s-s}	500	MPa			
			h_0^{s-tw}	0	MPa			

Table 4.4. Slip and twin variants included in numerical simulation.

Basal slip	Prismatic slip	Pyramidal <a>	Pyramidal <c+a>	Tensile twin
$[2\bar{1}\bar{1}0](0001)$	$[2\bar{1}\bar{1}0](0\bar{1}\bar{1}0)$	$[2\bar{1}\bar{1}0](01\bar{1}1)$	$[2\bar{1}\bar{1}3](\bar{2}112)$	$[1\bar{1}01](\bar{1}102)$
$[\bar{1}2\bar{1}0](0001)$	$[\bar{1}2\bar{1}0](\bar{1}001)$	$[\bar{1}2\bar{1}0](\bar{1}011)$	$[\bar{1}2\bar{1}3](1\bar{2}12)$	$[\bar{1}011](10\bar{1}2)$
$[\bar{1}\bar{1}20](0001)$	$[\bar{1}\bar{1}20](\bar{1}\bar{1}00)$	$[\bar{1}\bar{1}20](1\bar{1}01)$	$[\bar{1}\bar{1}23](11\bar{2}2)$	$[01\bar{1}1](0\bar{1}12)$
		$[11\bar{2}0](\bar{1}101)$	$[\bar{2}113](2\bar{1}\bar{1}2)$	$[\bar{1}101](1\bar{1}02)$
		$[\bar{2}110](0\bar{1}11)$	$[1\bar{2}13](\bar{1}2\bar{1}2)$	$[10\bar{1}1](\bar{1}102)$
		$[1\bar{2}10](10\bar{1}1)$	$[11\bar{2}3](\bar{1}\bar{1}22)$	$[0\bar{1}11](01\bar{1}2)$

4.2.1. Rolled Sample

The production of the representative volume elements (RVEs) in accordance with the realistic texture of the material has been described in Section 3.4.2. Figure 4.21 shows the particular RVE, presenting its rolling texture. The core element of the texture, [0001] || ND, is apparent in the Orientation maps. As mentioned in Section 3.4.2, this RVE contains 729 grains and is loaded in z-direction with the uniaxial test boundary conditions, $\sigma_{yy} = \sigma_{xx} = 0$.

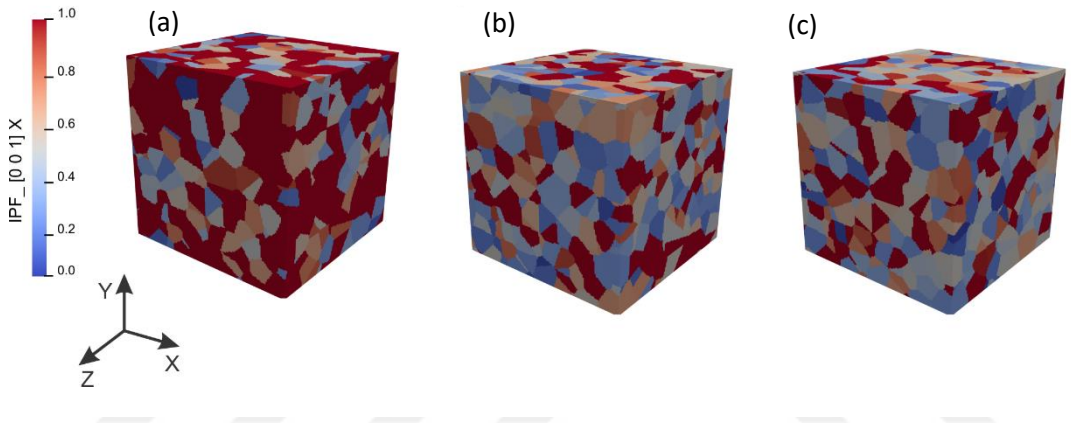

Figure 4.21. Orientation maps of the prepared representative spectral analysis volume (rolled texture) in terms of the cosine of the angle between crystal c-axis [0001] and (a) x-axis (ND), (b) y-axis (TD), (c) z-axis (RD). A value of 1 means alignment and 0 means orthogonality.

The data produced for comparison with the experimental data will only consider the first quadrant of the C-T-C cyclic loading in the experiments. More clearly, this part of the data can be considered as a simple compression test (where twinning is the dominant mechanism). The stress-strain curve of the analysis is shown in Figure 4.22. The twin plateau level of about (90-110 MPa) matches the experiment but the hardening level is a bit high compared to the near perfect plasticity of the actual material. In the model, such a flat plateau is captured for a perfect texture (c-axes || ND exactly) but for the RVEs produced with the realistic texture, a degree of hardening persists. The spatial development of stress at selected points over the stress strain curve is shown in Figure 4.23. While a strain

patterning (inherent to any polycrystal) develops, there is no clear band formation and advance as in the experimental results shown in Section 4.1.

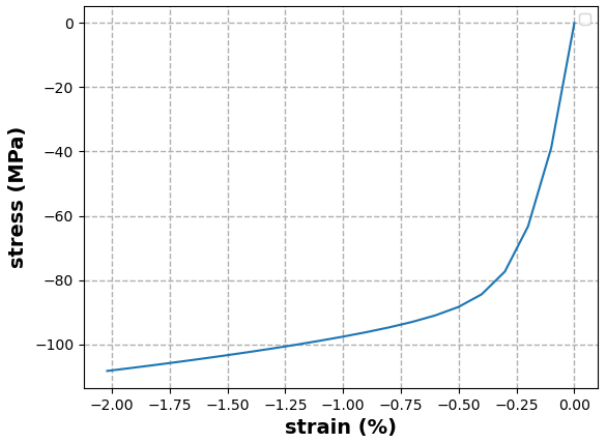

Figure 4.22. DAMASK results: Stress-strain curve for rolled RVE subjected to 2% compression along z-direction (RD) and measured over (TD).

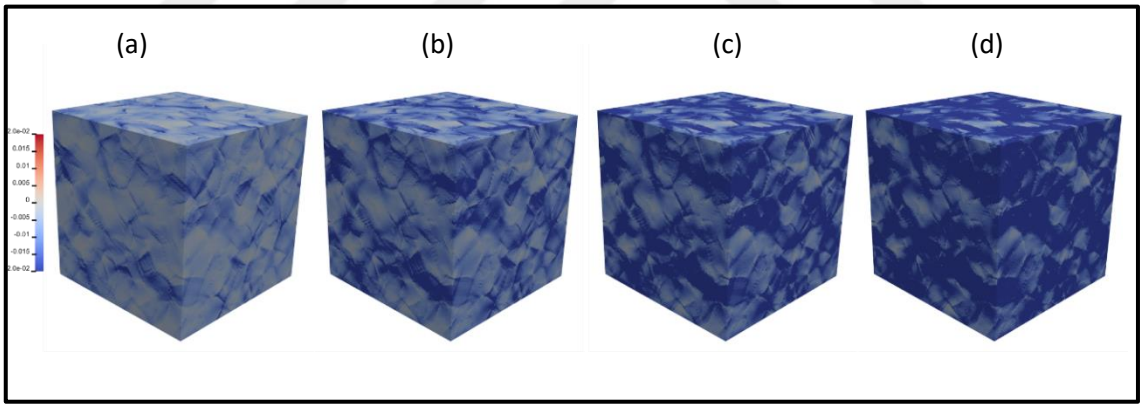

Figure 4.23. DAMASK analysis for rolled RVE and axial stress σ_{zz}. maps at macroscopic strains of (a) -0.8, (b) -1.2, (c) -1.6, (d) -2%.

4.2.2. Extruded Sample

Similar to Rolled RVE, test sample pole figure data is used to generate RVE for numerical simulations. Inverse pole figures for produced RVE are plotted in Figure 4.24. Compared to the sharp distribution of orientation in rolled sample, [0001] || ND, IPF maps

for extruded sample shows mode random orientations in all main directions since sharpness is presumably transverse.

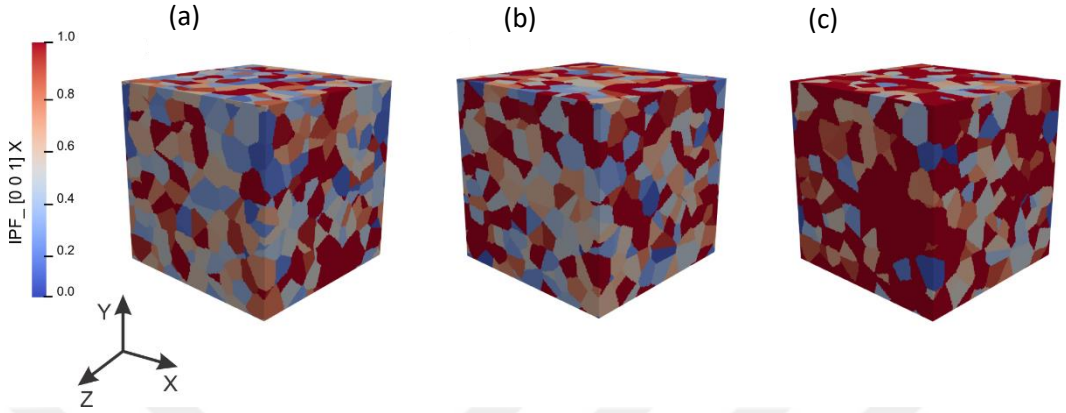

Figure 4.24. Orientation maps of the prepared representative spectral analysis volume (extruded texture) in terms of the cosine of the angle between crystal c-axis [0001] and (a) x-axis (ND), (b) y-axis (TD), (c) z-axis (RD). A value of 1 means alignment and 0 means orthogonality.

Stress strain curve for this simulation is shown in Figure 4.25, and evolution of strain maps (ε_{zz}) are portrayed in Figure 4.26. The predicted stress-strain curve shows very early plasticity with considerable hardening behavior. Again, like rolled RVE, perfect plastic-like twin plateau seen in experiments is not predicted in simulation. Stress level of ~100 MPa is reached at the end of 2% compression in z-direction.

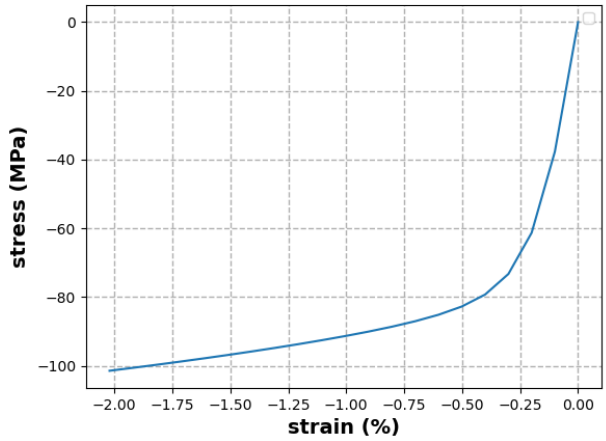

Figure 4.25. DAMASK results: Stress-strain curve for extruded RVE subjected to 2% compression along z-direction (RD) and measured over (TD).

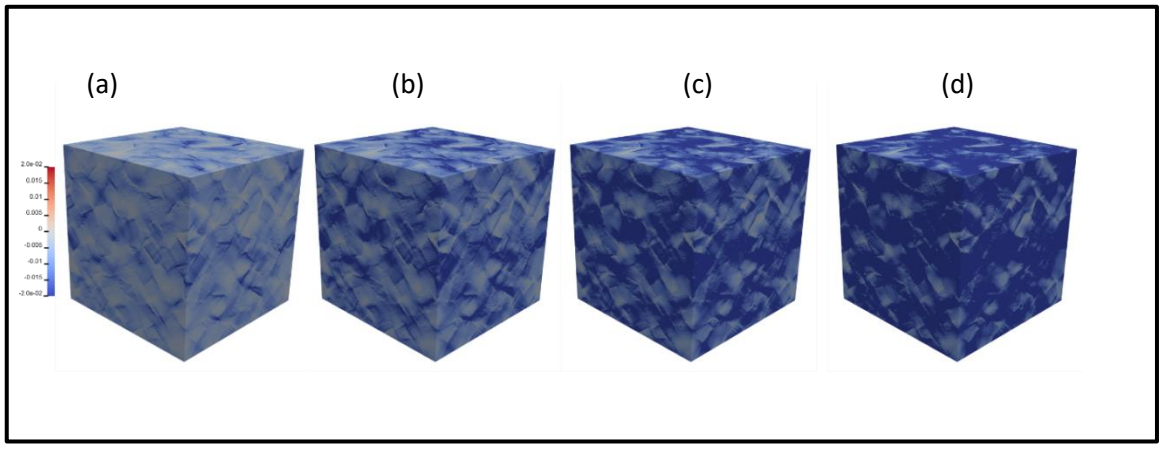

Figure 4.26. DAMASK analysis: extruded RVE and axial stress σ_{zz}. maps at macroscopic strains of (a) -0.8, (b) -1.2, (c) -1.6, (d) -2%.

4.3. Experiment-Model Comparison

The first hard test for the model is on how well it approximates the extreme kinematics of the rolled sample under twin-dominated deformation presented in Section 4.1.1, namely, $\bar{\nu}_{xz} = -\varepsilon_{ND}/\varepsilon_{RD} \sim 0$ and $\bar{\nu}_{yz} = -\varepsilon_{TD}/\varepsilon_{RD} \sim 1$. The two apparent Poisson's ratios for rolled texture are provided in Figure 4.27(a) and (b), respectively. The elastic portion of the graph shows a near isotropic Poisson's ratio (near equal in each subplot and about 0.3), expected from the near elastic isotropy of the Magnesium crystal. We are rather interested in the value after twinning commences. While the values are not fully saturated, it can be safely said that there is a trend that $\bar{\nu}_{yz} > \bar{\nu}_{xz}$ but the extreme values are not at all produced. For extruded RVE, apparent Poison's ratio is deviating from experimental finding even more. While both $\bar{\nu}_{yz}$and $\bar{\nu}_{xz}$ are found to be around 0.5 in experiment representing nearly isotropic deformation, values estimated by simulation Figure 4.29 is found to be consistent with experimental results (0.5).

The level of activity for each tensile twin variant for rolled and extruded RVEs are shown in Figure 4.29 and Figure 4.31 respectively. Accumulated twin shear in rolled sample shows a close agreement with the characteristic twin that could be accommodated by twin mechanism. The slight deviation here could be related to the difference in the twin initiation and progress that is seen to be strongly autocatalytic in experimental results. That is, in actual physical sample deformation preferably accommodates over existing shear bands until

reaching the characteristic twin strain. In simulation, on the other hand, formation of twin shear bands at multiple sites over the surface of sample, results in a less dense shear bands, hence lower twin shear than characteristic twin shear.

For extruded RVE, the level of tensile twin activity is lower than that of rolled sample, meaning a smaller contribution from tensile twin is compensated by slip systems to reach 2% in extruded RVE compared to rolled one. This also means shear per twin mechanism does not easily tend to reach the characteristic value and rather leans toward sharing accommodating strain with other mechanisms or triggering other remote shear formation sites. Also, DAMASK is still uncapable of highlighting the different strain localization mechanisms in rolled and extruded RVEs on strain maps, however, twin activity plots address it in a weak form.

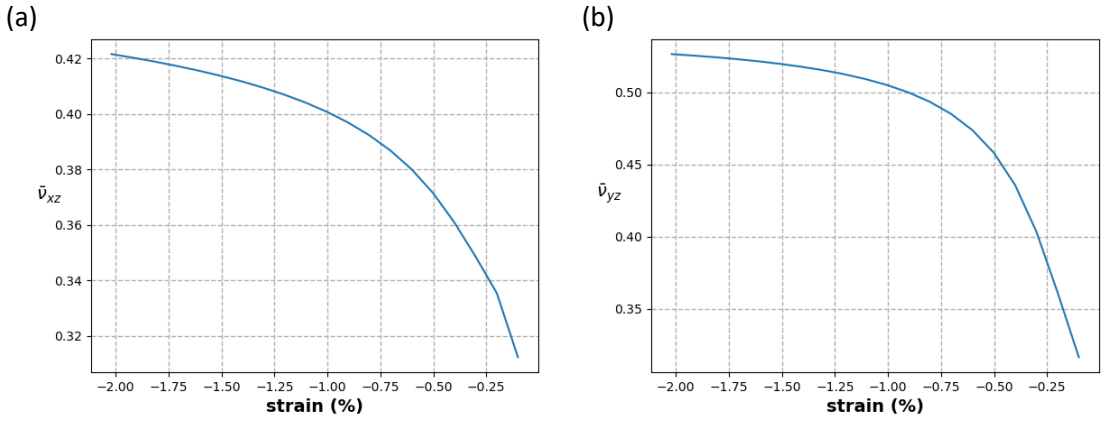

Figure 4.27. DAMASK analysis: effective Poisson's ratio for rolled RVE. (a) $\bar{\nu}_{xz}$, and (b) $\bar{\nu}_{yz}$.

To provide statistical data for what DAMASK has predicted, the progress of strain histograms (normalized for area under the curve to be 1) ε_{xx} and ε_{zz} for load steps $\bar{\varepsilon}_{zz}$ = 0.8, 1.2, 1.6 and 2% for both RVEs are portrayed in Figure 4.31. ε_{zz} is shown with solid lines and ε_{xx} plotted with dashed lines. Like experimental observations, histograms are getting broader for higher strain accommodation. Strain population shows a wider distribution range for extruded sample compared to rolled at identical average strain in Figure 4.31. This is also in agreement with strain histograms obtained experimentally.

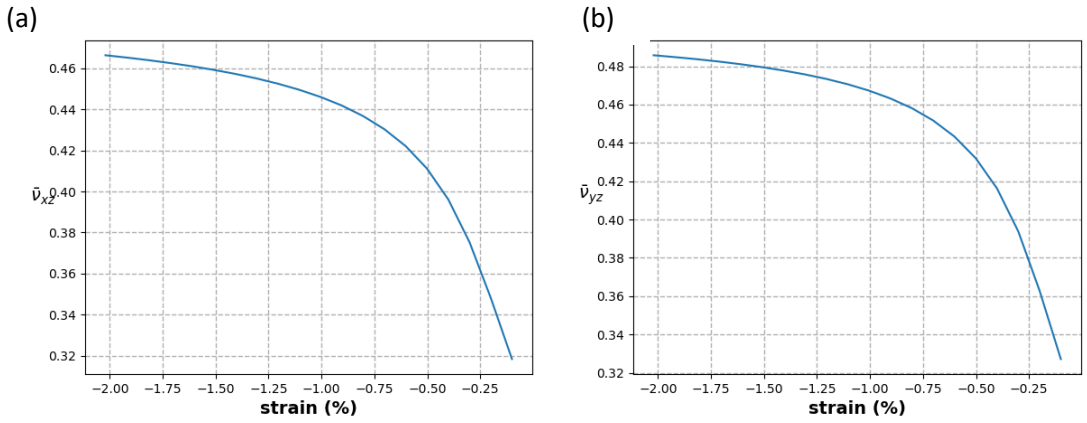

Figure 4.28. DAMASK analysis: effective Poisson's ratio for extruded RVE. (a) $\bar{\nu}_{xz}$, and (b) $\bar{\nu}_{yz}$.

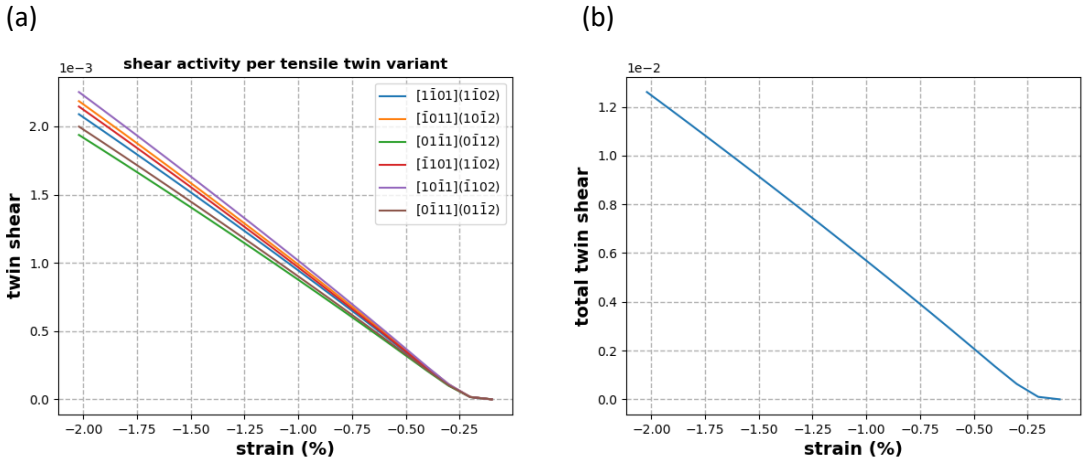

Figure 4.29. DAMASK results: (a) twin shear activity per twin mechanism and (b) accumulative twin shear for rolled RVE.

To examine DAMASK's ability to stablish a sensible bridge between contributing micromechanisms and accommodated strain features, basal slip and tensile twin resistances as the most dominant deformation mechanisms are plotted side by side the ε_{zz} map for both textures in Figure 4.32 and Figure 4.33 respectively. Developing high resistance regions at exact spatial locations of high strain accommodation sites is clearly in agreement with the Equations (3.24) and Equations (3.25).

Shear that is accommodated by each tensile twin variant is shown in Figure 4.29 and Figure 4.30. However, the spatial location of accommodated shear by each twin variant is

missing in these plots. Figure 4.35 and Figure 4.36 and portray the spatial localization of accommodated shear per tensile twin family from a to f. the accumulated shear by all variants is shown side by side the strain maps at 2% to have a clear picture of the contribution of twin shear in the ultimate strain accommodated over the RVE surface. Some examples of the contribution for intragrain and over the grain boundary strain accommodation are highlighted by circles and arrows.

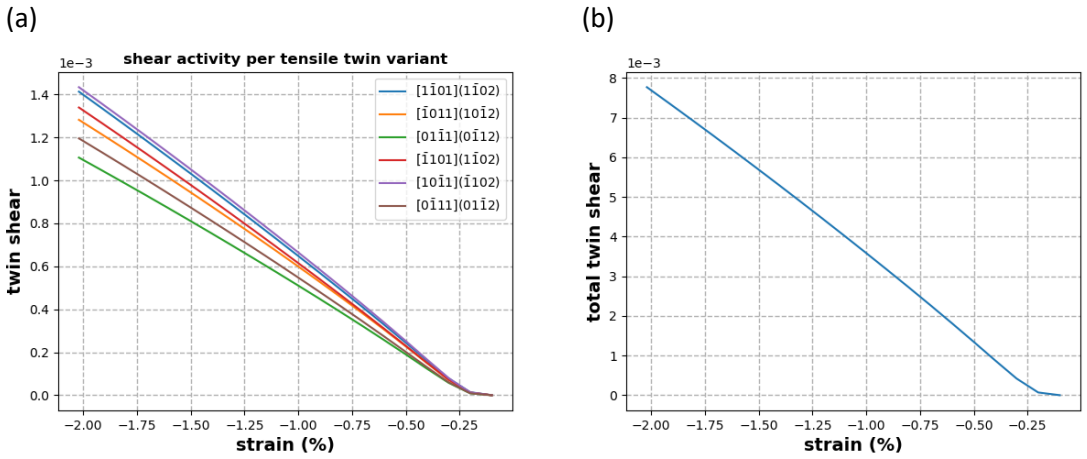

Figure 4.30. DAMASK results: (a) twin shear activity per twin mechanism and (b) accumulative twin shear for extruded RVE.

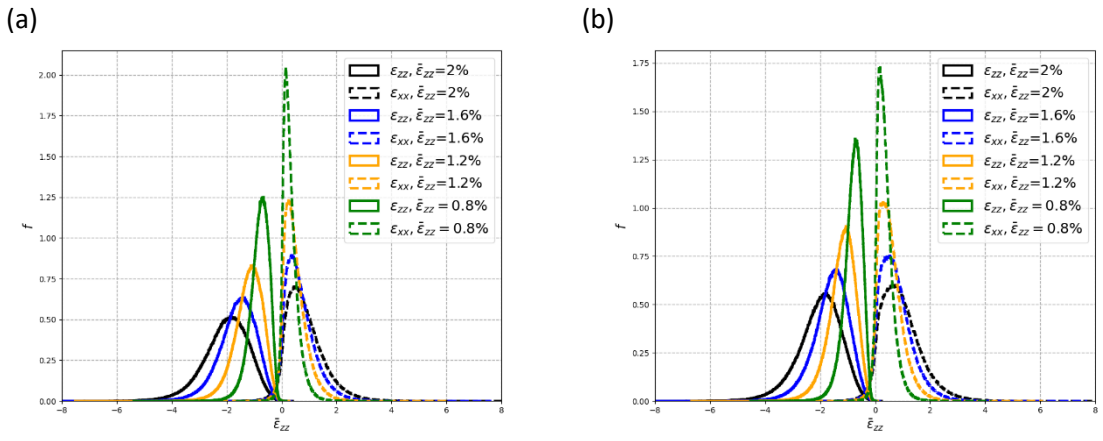

Figure 4.31. DAMASK results: $\varepsilon_{xx}$and ε_{zz} strain histograms at macroscopic strains of (a) Rolled and (b) Extruded RVEs at $\bar{\varepsilon}_{zz}$ = 0.8,1.2, 1.6 and -2%.

Fidelity of the numerical results is examined by comparing the predicted stress-strain curves for both textures at first quadrant to experimental results (Figure 4.36). In both cases transition from elastic region to plastic is predicted at very early stages. While experimental curves enter the plastic deformation at $\bar{\varepsilon}_{zz}$= ~0.25%, this value is predicted to be nearly one third in simulation by DAMASK. In both cases, substantial hardening is reported at twin dominated portion of the curve and nearly perfect plateau observed in experimental results is not achieved by current model. Stress- levels are either slightly under-predicted for rolled RVE (-90 MPa experimentally vs -105 MPa numerically @$\bar{\varepsilon}_{zz}$=2%) or over-predicted for extruded RVE (-115 MPa experimentally vs -100 MPa numerically @$\bar{\varepsilon}_{zz}$=2%).

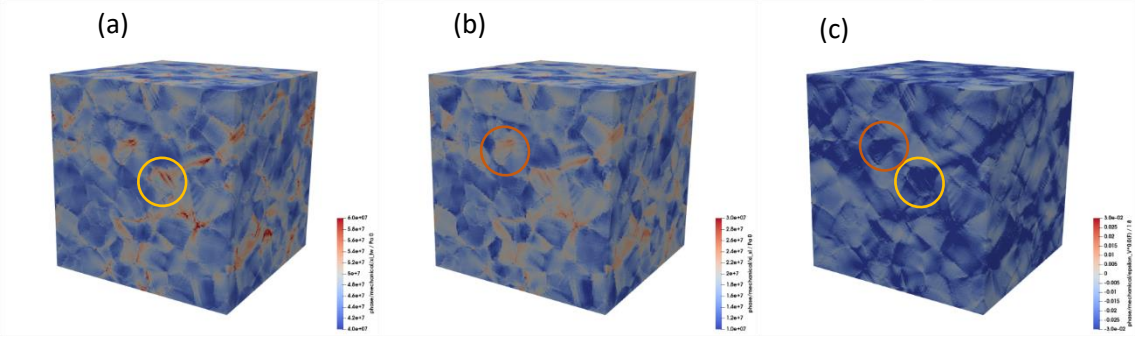

Figure 4.32. DAMASK results: (a) tensile twin and (b) basal slip resistance at $\varepsilon_{zz} = 2\%$ average strain compared to the (c) accumulated strain in rolled RVE.

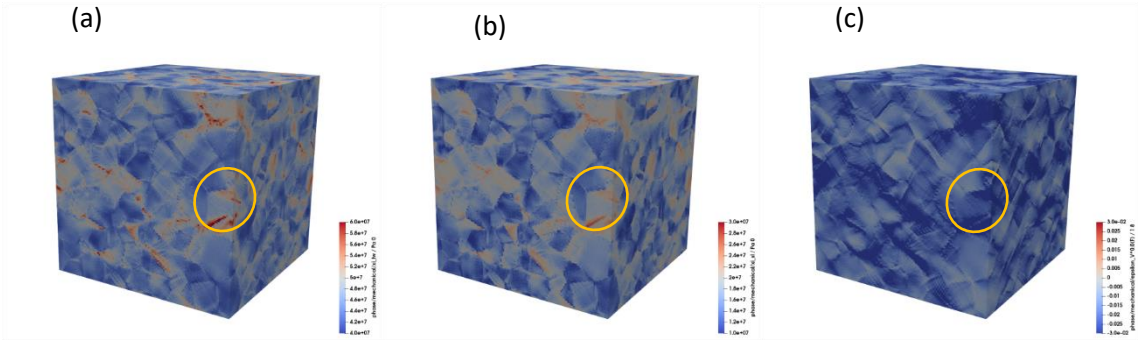

Figure 4.33. DAMASK results: (a) tensile twin and (b) basal slip resistance at $\bar{\varepsilon}_{zz}$= 2% average strain compared to the (c) accumulated strain in extruded RVE.

Numerical results for cyclic load are also compared to experimental data. Main objective here is to assess the capability of model predicting detwinning under reverse load.

Experimental results showed that strain recovery by detwinning is operational at the beginning of quadrant III. In simulation by DAMASK, however, the elastic strain recovery lasts up to ~50 MPa in quadrant III. The strain recovery over detwinning incorporates hardening according to the experimental outcome; another trait that is also missing in the numerical results. This is also shown with the aid of twin activities over the full cycle in Figure 4.37 c-d. All twin variants are inactive during elastic recovery at the beginning of quadrant III (no change in produced twin shear). With the termination of elastic recovery, twin mechanisms demonstrate substantial activities which are unexpected based on experimental results.

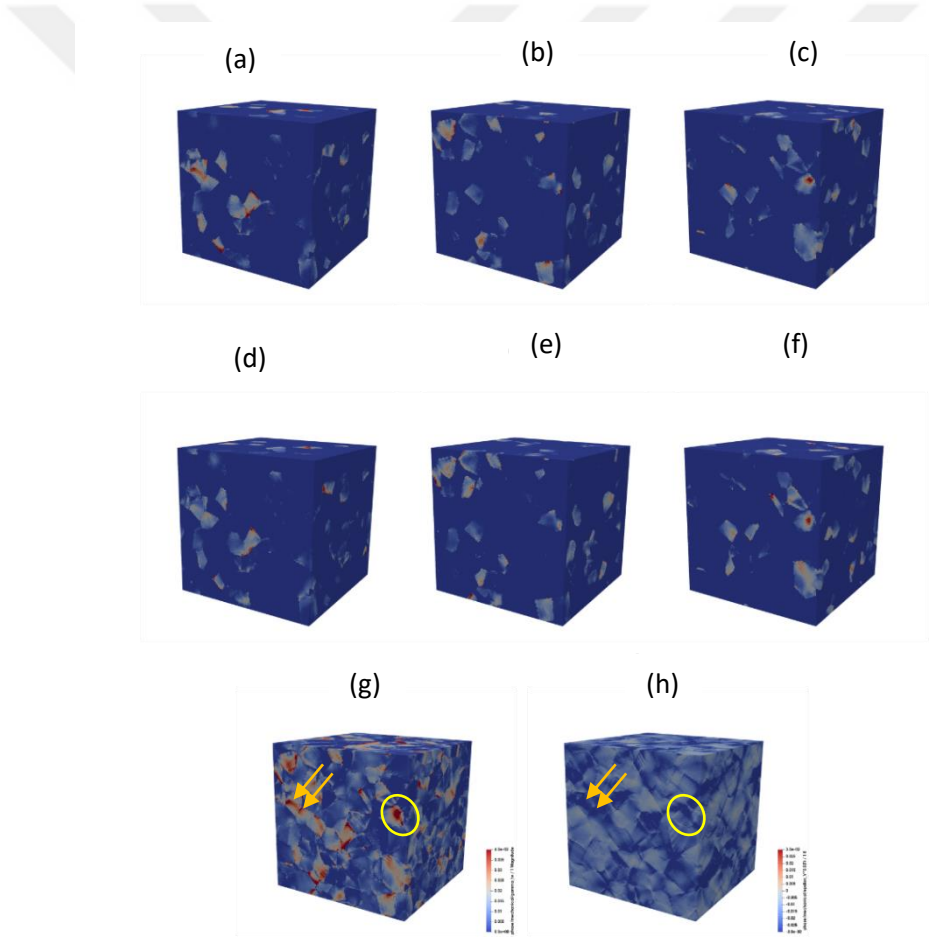

Figure 4.34. Twin shear per tensile twin variants for rolled RVE at $\bar{\varepsilon}_{zz}$ = 2% strain. (a) $[1\bar{1}01](\bar{1}102)$, (b) $[\bar{1}011](10\bar{1}2)$, (c) $[01\bar{1}1](0\bar{1}12)$, (d) $[\bar{1}101](1\bar{1}02)$, (e) $[10\bar{1}1](\bar{1}102)$, (f) $[0\bar{1}11](01\bar{1}2)$, (g) accumulated shear by all tensile twin variants, (h) strain map ε_{zz}.

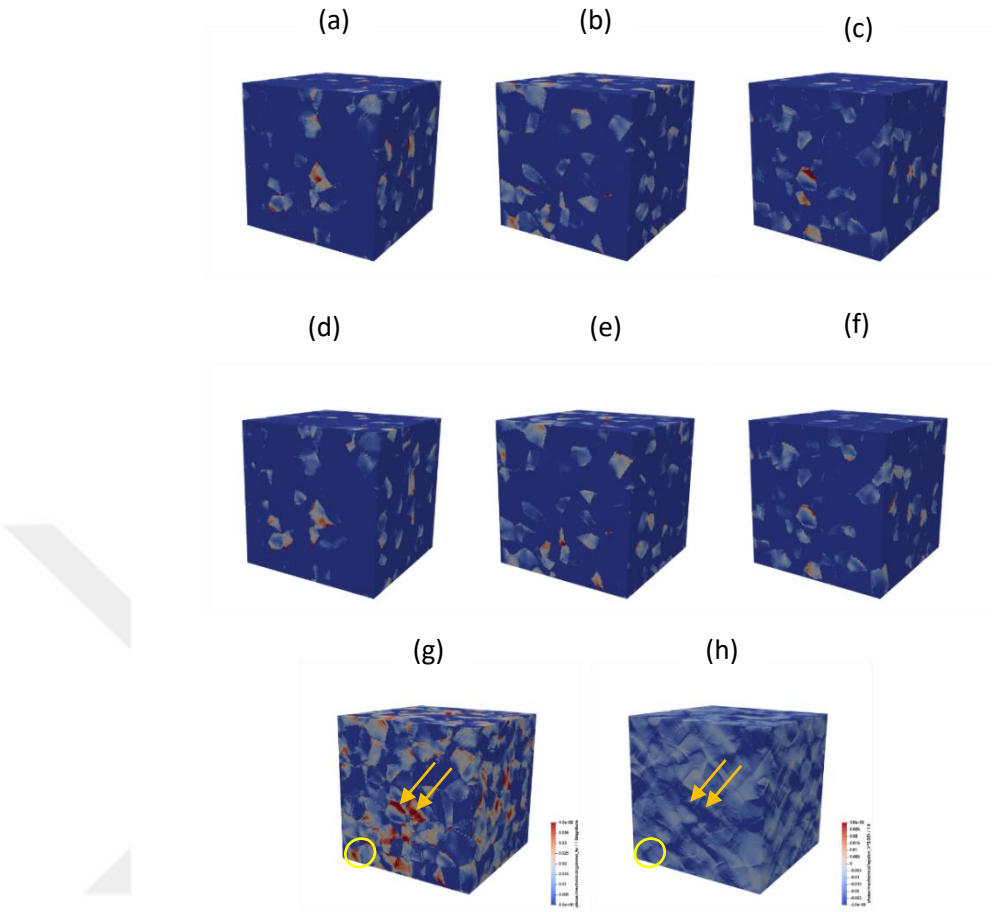

Figure 4.35. Twin shear per tensile twin variants for extruded RVE at $\bar{\varepsilon}_{zz}$ = 2% strain. (a) $[1\bar{1}01](\bar{1}102)$, (b) $[\bar{1}011](10\bar{1}2)$, (c) $[01\bar{1}1](0\bar{1}12)$, (d) $[\bar{1}101](1\bar{1}02)$, (e) $[10\bar{1}1](\bar{1}102)$, (f) $[0\bar{1}11](01\bar{1}2)$, (g) accumulated shear by all tensile twin variants, (h) strain map ε_{zz}.

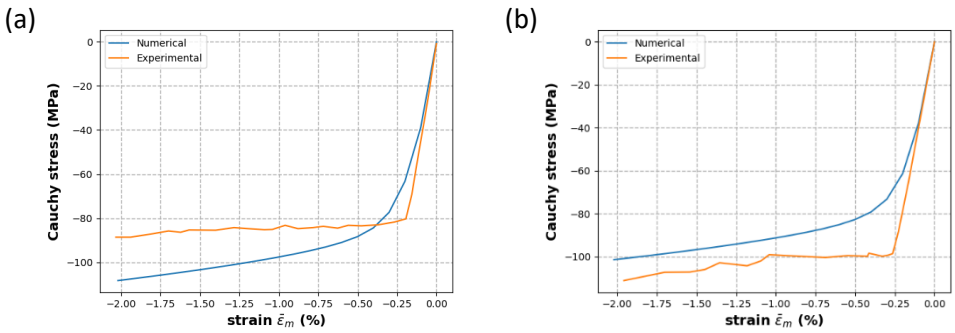

Figure 4.36. Experimentally constructed stress-strain curve compared to numerical estimation: (a) rolled RVE simulation predicts higher stress level compared to experimental result and (b) extruded RVE simulation underpredicts stress level.

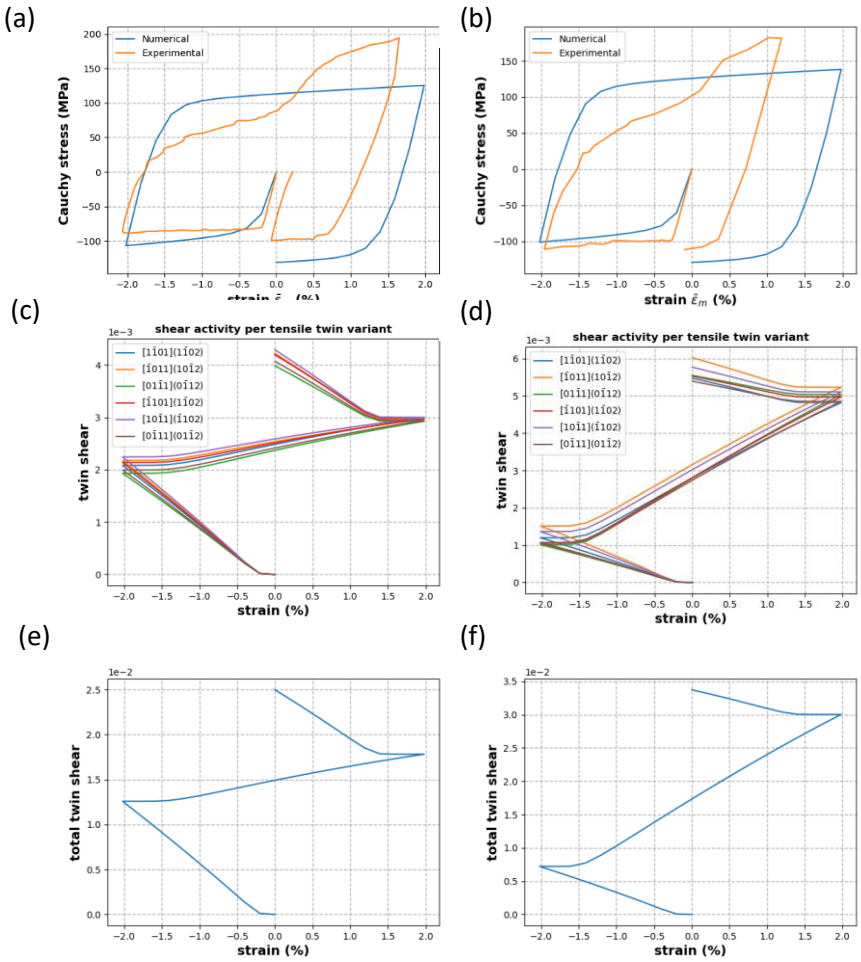

Figure 4.37. Experimental and numerical comparison of C-T-C stress strain curves for rolled (a) and extruded (b) samples. Tensile twin shear activity per variant under cyclic load for rolled (c) and extruded (d) RVEs. Total twin shear for rolled (e) and extruded (b) RVEs.

4.3.1. Reflection on Modeling

In-situ measurements for rolled Magnesium present extraordinary challenges for the models toward the goal of reproducing the mesoscale fields. To be precise, the simulations to-date are typically not equipped for either of the two major strain localization forms that are shown to govern the strain heterogeneity in these materials.

Out of these, the micro-texture (non-45°) bands do not pose particular difficulty in terms constitutive behavior (perhaps aside from the need to account for varying grain size

[40],[97],[81],[13]). Being a morphological effect, the obvious remedy is to faithfully incorporate them into a sufficiently large representative volume element—nevertheless a considerable effort in pre-characterization and pre-processing. The practice so far typically ignores them by assigning a single orientation distribution function (ODF) to the in-reality bimodal aggregate. This can be involuntary, e.g., in the case of bulk-diffraction measurement of texture, where the micro-texture grains are merely counted as off-texture grains. The ignored spatial coordination, however, is the actual factor that underlies their substantial influence from a limited volume fraction. This omission has been noted to limit prediction ability even for macroscopic kinematics of plasticity leading to large errors in r-ratio [50].

While the knowledge of such bands, with their effects on in-plane anisotropy [69], date back to Couling et al. [98], their inherited existence in annealed samples [91] still appears to be poorly established—more confined to the thermal processing literature [99]. This is partly interesting since, while strains on these bands are not properly resolved in macroscopic strain mapping [25],[26], their deformation traces typically become visible on macrographs [26],[100].We already commented on their influence on macroscopic measures, however clearly, their effect on local strain heterogeneity is much more pronounced and central to the cyclic damage that the material suffered at the end point of the current experiment. A dominant effect of inherited long-range microstructural heterogeneity has also recently been detailed for alpha-beta Titanium [101,102], supporting the common conclusion that a pivotal step toward mesoscale fidelity in complex materials is the spatially resolved characterization of initial the microstructure.

The other primary strain localization form, TTD localization bands, conversely, pose extreme difficulty in terms of constitutive behavior [82] and geometric implementation. The physical fidelity has been gradually improved by accounting for the nucleation, growth, and propagation stages of deformation twinning [93],[13] and surpassing the unrealistic homogenization of the twins (“pseudo-slip models”, e.g.,[39],[103]) with the newer discrete-twin implementations [12,13]. These are now viable for reproducing twin transmission phenomena in realistic grain neighborhoods [14].

We emphasize the case-specific critical role of the utilized area-scanning for rolled Magnesium, in conjunction to these two strain superstructures that proceed through

numerous grains. In a more regular polycrystal, representative area/volume size can be few-to-several grains large [14] and, in that case, the strain fields in the individual-frames of the area-scan would be essentially equivalent. As such, the benefit of the area-scan would not be as critical (only a confirmation that the representative area size is smaller than the frame size). For rolled Magnesium, on the other hand, the stitched frames spatially construct the full nature of the deformation. This is incidentally why the proper characterization of these structures can remain elusive to typical measurement tools that entail a strict compromise between field coverage and spatial resolution. (A typical microscopic measurement lacks sufficient coverage whereas a macroscopic measurement doesn't have the required resolution.) SMDIC, on the other hand, provides an optimal length-scale range to study both the overall character and the grain-scale detail of these structures.

5. CONCLUSION

In the span of multiple length-scales that govern the structure property relations of polycrystalline aggregates, a blind spot (that macroscopic measurements average over and microscopic measurements zoom into) can lie in the long-range collaborative strain accommodation across grains. We detail the dominant effect of such strain coordination in rolled Magnesium over a compression-tension-compression cycle, using a novel in-situ implementation of area-scanning microscopic DIC. The primary conclusions are as follows:

- The material exhibits little strain heterogeneity at midcycle (first zero-mean strain) whereas a burst of strain heterogeneity after the full C-T-C cycle.
- The burst after C-T-C has a strong microstructural component: In the tension (T) step, preferential slip and heavy latent hardening occurs in the inherent micro-texture channels. Under final compression, the tensile strain recovers only partially in these when the sudden introduction of compressive-strain SW-TTD bands freezes them in place, leading to a compound strain field with discrete compressive/tensile elements.
- The limited remnant strains at the first zero-mean strain are concentrated at the TTD-band intersections. Overall, detwinning operates uniformly over the intergranular-strain-localization fabric of the TTD bands.
- The characteristic compactness of the TTD-band fabric shows a marked decrease after cyclic hardening. It is postulated that the bands are scattered by the heterogeneous latent hardening fields of the non-45° micro-texture veins.
- The results clearly show the elevated importance of measuring and accounting for the spatial details of strain accommodation in Magnesium at multiple length-scales.
- The macroscopic coordination of the tensile-twin-driven strain localization structures lead to Lüders-like macroscopic strain bands over the twin plateau. These are, however, less dense (in terms of strain) compared to the rolled structure and their propagation boundaries have a diffuse character. After the gage section is covered with an intergranular strain network, diffuse strain advances keep augmenting the fields by favoring the less dense locations.
- Once the average strain over the field of the extruded material is increased to the high Lüders-strain of a rolled sample (with comparable grain size), the strain heterogeneity

of the extruded sample supersedes the strain heterogeneity of the rolled sample at this measurement length-scale.

- Detwinning has a straightforward signature in the standard deviation plots (a decay that follows a near parallel line compared to the increase over the twin plateau).
- A second compression, after inducing tensile plasticity in tension, results in polar strain localization structures with tensile and compressive elements.

The numerical approach included in DAMASK and tested against this data yielded the following conclusions:

- For monotonic compression along RD and ED directions in rolled and extruded RVEs, stress-strain curves are predicted to be in a close range of experimental results. However, in both cases, plastic deformation begins earlier in simulations and twin plateau shows significant hardening that is not the case in experimental results.
- The formation of major shear band with high strain content that is seen in rolled sample result under compression in experiment, is not reproduced by DAMASK. Several shear bands are formed instead in simulation. Although Lüders-like shear band progression could be marked at some levels, it does not lead to formation of a major shear band.
- Apparent Poison's ratios of rolled textures is consistent with experimental finding however, for rolled texture, these values deviate from test results.
- DAMASK with the current constitutive model is not capable of projecting detwinning when load is reversed after initial compression with excessive introduction of twining. Twin mechanisms are still operational during the reverse load according to twin activity plots.

6. FUTURE WORKS

With all the valuable efforts done till day, the clearest calibration target that numerical models can derive from measurement is the characteristic strains of the twin bands. Note this viable objective doesn't depend on the macroscopic location of the band (which is stochastic). From relaxed to stringent, the models should strive to satisfy the average strain, the strain statistics, and the spatial strain distribution measured over the TTD band for their precise microstructural parameters. True fidelity will also require the models to meet all strain components, and in this sense, matching the extreme plastic anisotropy of the bands is already an interesting target. Obviously, trying to meet the strain distributions all through the cycle is a loftier objective. Particularly, the dilution in SW-TTD activity can only be targeted with RVEs that account for the secondary microstructure. In general, there would be tremendous confidence in the universality of a model that can represent the nominal character of strain distributions at all load points in the cycle. Derivation of geometric measures like mean free spacing of twin meshes will also provide more twin related characteristics that could also feed the numerical models to achieve more precise prediction of twin driven shear formation and propagation. From the modelling perspective, even higher fidelity models with discrete twin formulations are required. More comprehensive constitutive formulations with the capability to model different deformation phenomena (like detwinning in cyclic loading) are essential to extend versatility and accuracy of the models.

REFERENCES

1. Song, G., “Recent Progress in Corrosion and Protection of Magnesium Alloys”, *Advanced Engineering Matererials*, Vol. 7, No. 7, pp. 563–586, 2005.

2. Landkof, B., *Magnesium Alloys and Their Appllications*, Wiley, New York, 2000.

3. Christian, J. W. W. and S. Mahajan, “Deformation Twinning”, *Progress in Materials Science*, Vol. 39, No. 1–2, pp. 1–157, 1995.

4. Clausen, B., C. N. Tomé, D. W. Brown, and S. R. Agnew, “Reorientation and Stress Relaxation Due to Twinning: Modeling and Experimental Characterization for Mg”, *Acta Materialia*, Vol. 56, No. 11, pp. 2456–2468, 2008.

5. Lou, X. Y., M. Li, R. K. Boger, S. R. Agnew, and R. H. Wagoner, “Hardening Evolution of AZ31B Mg Sheet”, *International Journal of Plasticity*, Vol. 23, No. 1, pp. 44–86, 2007.

6. Kleiner, S. and P. Uggowitzer, “Mechanical Anisotropy of Extruded Mg–6% Al–1% Zn alloy”, *Materials Science and Engineering. A*, Vol. 379, No. 1–2, pp. 258–263, 2004.

7. Guillemer, C., M. Clavel, and G. Cailletaud, “Cyclic Behavior of Extruded Magnesium: Experimental, Microstructural and Numerical Approach”, *International Journal of Plasticity*, Vol. 27, No. 12, pp. 2068–2084, 2011.

8. Song, L. H., B.L. Wu, L. Zhang, X.H. Du, Y.N. Wang, Y.D. Zhang, C. Esling, “Cyclic Deformation Behaviors of AZ31B Magnesium Alloy in Two Different Asymmetric Loading Manners”, *Materials Science and Engineering A*, Vol. 689, pp. 134–141, 2017.

9. Lee, S. Y. and M. A. Gharghouri, “Pseudoelastic Behavior of Magnesium Alloy

During Twinning-Dominated Cyclic Deformation", *Materials Science and Engineering A*, Vol. 572, pp. 98–102, 2013.

10. Wang, H., P. D. Wu, and J. Wang, "Modeling Inelastic Behavior of Magnesium Alloys During Cyclic Loading-Unloading", *International Journal of Plasticity*, Vol. 47, pp. 49–64, 2013.

11. Vidyasagar, A., A. D. Tutcuoglu, and D. M. Kochmann, "Deformation Patterning in Finite-Strain Crystal Plasticity By Spectral Homogenization With Application to Magnesium", *Computer Methods in Applied Mechanics and Engineering*, Vol. 335, pp. 584–609, 2018.

12. Abdolvand, H. and M. R. Daymond, "Multi-Scale Modeling and Experimental Study of Twin Inception and Propagation in Hexagonal Close-Packed Materials Using a Crystal Plasticity Finite Element Approach; Part II: Local Behavior", *Journal of the Mechanics and Physics of Solids*, Vol. 61, No. 3, pp. 803–818, 2013.

13. Cheng, J. and S. Ghosh, "Crystal Plasticity Finite Element Modeling of Discrete Twin Evolution in Polycrystalline Magnesium", *Journal of the Mechanics and Physics of Solids*, Vol. 99, pp. 512–538, 2017.

14. Cheng, J., J. Shen, R. K. Mishra, and S. Ghosh, "Discrete Twin Evolution in Mg Alloys Using a novel Crystal Plasticity Finite Element Model", *Acta Materialia*, Vol. 149, pp. 142–153, 2018.

15. Aydıner, C. C. and M. A. Telemez, "Multiscale Deformation Heterogeneity in Twinning Magnesium Investigated with In Situ Image Correlation", *International Journal of Plasticity*, Vol. 56, pp. 203–218, 2014.

16. Üçel, İ. B., E. Kapan, O. Türkoğlu, and C. C. Aydıner, "In Situ Investigation of strain Heterogeneity and Microstructural Shear Bands in Rolled Magnesium AZ31", *International Journal of Plasticity*, Vol. 118, pp. 233–251, 2019.

17. Chen, Z. and S. Daly, “Deformation Twin Identification in Magnesium Through Clustering and computer Vision”, *Materials Science and Engineering A*, Vol. 736, No. July, pp. 61–75, 2018.

18. Orozco-Caballero, A., D. Lunt, J. D. Robson, J. Q. da Fonseca, “How Magnesium Accommodates Local Deformation Incompatibility: A High-Resolution Digital Image Correlation Study”, *Acta Materialia*, Vol. 133, pp. 367–379, 2017.

19. Martin, G., C. W. Sinclair, W. J. Poole, and H. Azizi-Alizamini, “Local Plastic-Strain Heterogeneities and Their Impact on the Ductility of Mg”, *The Journal of the Minerals, Metals & Materials Society*, Vol. 67, No. 8, pp. 1761–1773, 2015.

20. Efstathiou, C., H. Sehitoglu, and J. Lambros, “Multiscale Strain Measurements of Plastically Deforming Polycrystalline Titanium: Role of Deformation Heterogeneities”, *International Journal of Plasticity*, Vol. 26, No. 1, pp. 93–106, 2010.

21. Muránsky, O., M. R. Barnett, D. G. Carr, S. C. Vogel, and E. C. Oliver, “Investigation of Deformation Twinning in a Fine-Grained and Coarse-Grained ZM20 Mg Alloy: Combined in Situ Neutron Diffraction and Acoustic Emission”, *Acta Materialia*, Vol. 58, No. 5, pp. 1503–1517, 2010.

22. Barnett, M. R., M. D. Nave, and A. Ghaderi, “Yield Point Elongation Due to Twinning in a Magnesium Alloy”, *Acta Materialia*, Vol. 60, No. 4, pp. 1433–1443, 2012.

23. Muránsky, O., M. R. Barnett, V. Luzin, and S. Vogel, “On the Correlation Between Deformation Twinning and Lüders-Like Deformation in an Extruded Mg Alloy: In Situ Neutron Diffraction and EPSC.4 Modelling”, *Materials Science and Engineering A*, Vol. 527, No. 6, pp. 1383–1394, 2010.

24. Hazeli, K., J. Cuadra, P. A. A. Vanniamparambil, and A. Kontsos, “In Situ Identification of Twin-Related Bands Near Yielding in a Magnesium Alloy”, *Scripta Materialia*, Vol. 68, No. 1, pp. 83–86, 2013.

25. Kapan, E., N. Shafaghi, S. Uçar, and C. C. Aydıner, "Texture-Dependent Character of Strain Heterogeneity in Magnesium AZ31 Under Reversed Loading", *Materials Science and Engineering A*, Vol. 684, No. December 2016, pp. 706–711, 2017.

26. Anten, K. and B. Scholtes, "Formation of Macroscopic Twin Bands and Inhomogeneous Deformation During Cyclic Tension-Compression Loading of the Mg-Wrought Alloy AZ31", *Materials Science and Engineering A*, Vol. 746, No. August 2018, pp. 217–228, 2019.

27. Mo, C. and A. Kontsos, "Twinning Contributions to strain Localizations in Magnesium Alloys", *Materials Science and Engineering A*, Vol. 722, No. March, pp. 206–215, 2018.

28. Roters, F., M. Diehl, P. Shanthraj, P. Eisenlohr, C. Reuber, S.L. Wong, T. Maiti, A. Ebrahimi, T. Hochrainer, H.-O. Fabritius, S. Nikolov, M. Friák, N. Fujita, N. Grilli, K.G.F. Janssens, N. Jia, P.J.J. Kok, D. Ma, F. Meier, E. Werner, M. Stricker, D. Weygand, D. Raabe, "DAMASK – The Düsseldorf Advanced Material Simulation Kit for Modeling Multi-Physics Crystal Plasticity, Thermal, and Damage Phenomena from the Single Crystal up to the Component Scale", *Computational Materials Science*, Vol. 158, pp. 420–478, 2019.

29. Brown, D. W., S. R. Agnew, M. A. M. M. Bourke, T. M. Holden, S. C. Vogel, and C. N. Tomé, "Internal Strain and Texture Evolution During Deformation Twinning in Magnesium", *Materials Science and Engineering A*, Vol. 399, No. 1–2, pp. 1–12, 2005.

30. El Kadiri, H., C. D. Barrett, J. Wang, and C. N. Tomé, "Why Are {10-12} Twins Profuse in Magnesium?", *Acta Materialia*, Vol. 85, pp. 354–361, 2015.

31. Agnew, S. R., D. W. Brown, and C. N. Tomé, "Validating a Polycrystal Model for the Elastoplastic Response of Magnesium Alloy AZ31 Using In Situ Neutron Diffraction", *Acta Materialia*, Vol. 54, No. 18, pp. 4841–4852, 2006.

32. Agnew, S. R., C. N. Tomé, D. W. Brown, T. M. Holden, and S. C. Vogel, “Study of Slip Mechanisms in a Magnesium Alloy by Neutron Diffraction and Modeling”, *Scripta Materialia*, Vol. 48, No. 8, pp. 1003–1008, 2003.

33. Jiang, L., J. J. Jonas, R. K. Mishra, A. A. Luo, A. K. Sachdev, and S. Godet, “Twinning and Texture Development in Two Mg Alloys Subjected to Loading Along Three Different Strain Paths”, *Acta Materialia*, Vol. 55, No. 11, pp. 3899–3910, 2007.

34. Keshavarz, Z. and M. R. Barnett, “EBSD Analysis of Deformation Modes in Mg-3Al-1Zn”, *Scripta Materialia*, Vol. 55, No. 10, pp. 915–918, 2006.

35. Koike, J., “Enhanced Deformation Mechanisms by Anisotropic Plasticity in Polycrystalline Mg Alloys at Room Temperature”, *Metallurgical and Materials Transactions A*, Vol. 36, No. July, pp. 1689–1696, 2005.

36. Wu, L., S.R. Agnew, Y. Ren, D.W. Brown, B. Clausen, G.M. Stoica, H.R. Wenk, P.K. Liaw, “The Effects of Texture and Extension Twinning on the Low-Cycle Fatigue Behavior of a Rolled Magnesium Alloy, AZ31B”, *Materials Science and Engineering A*, Vol. 527, No. 26, pp. 7057–7067, 2010.

37. Hazeli, K., H. Askari, J. Cuadra, F. Streller, R.W. Carpick, H.M. Zbib, A. Kontsos, “Microstructure-Sensitive Investigation of Magnesium Alloy Fatigue”, *International Journal of Plasticity*, Vol. 68, pp. 55–76, 2015.

38. Wang, Y. N. and J. C. Huang, “Texture Analysis in Hexagonal Materials”, *Materials Chemistry and Physics*, Vol. 81, No. 1, pp. 11–26, 2003.

39. Zhang, J. and S. P. Joshi, “Phenomenological Crystal Plasticity Modeling and Detailed Micromechanical Investigations of Pure Magnesium”, *Journal of the Mechanics and Physics of Solids*, Vol. 60, No. 5, pp. 945–972, 2012.

40. Oppedal, A. L., H. El Kadiri, C.N. Tomé, G.C. Kaschner, Sven C. Vogel, J.C. Baird, M.F. Horstemeyer, “Effect of Dislocation Transmutation on Modeling Hardening

Mechanisms by Twinning in Magnesium", *International Journal of Plasticity*, Vol. 30–31, pp. 41–61, 2012.

41. Wu, L., A. Jain, D.W. Brown, G.M. Stoica, S.R. Agnew, B. Clausen, D.E. Fielden, P.K. Liaw, "Twinning–Detwinning Behavior During the Strain-Controlled Low-Cycle Fatigue Testing of a Wrought Magnesium Alloy, ZK60A", *Acta Materialia*, Vol. 56, No. 4, pp. 688–695, 2008.

42. Yin, S. M., F. Yang, X. M. Yang, S. D. Wu, S. X. Li, and G. Y. Li, "The Role Of Twinning-Detwinning on Fatigue Fracture Morphology of Mg-3%Al-1%Zn alloy", *Materials Science and Engineering A*, Vol. 494, No. 1–2, pp. 397–400, 2008.

43. Zhang, J., Y. Cai, W. Ye, and T. X. Yu, "On the Use of the Digital Image Correlation Method for Heterogeneous Deformation Measurement of Porous Solids", *Optics and Lasers in Engineering*, Vol. 49, No. 2, pp. 200–209, 2011.

44. Zhang, J., Q. Yu, Y. Jiang, and Q. Li, "An Experimental Study of Cyclic Deformation of Extruded AZ61A Magnesium Alloy", *International Journal of Plasticity*, Vol. 27, No. 5, pp. 768–787, 2011.

45. Proust, G., C. N. Tomé, A. Jain, and S. R. Agnew, "Modeling the Effect of Twinning and Detwinning During Strain-Path Changes of Magnesium Alloy AZ31", *International Journal of Plasticity*, Vol. 25, No. 5, pp. 861–880, 2009.

46. Vinogradov, A., D. Orlov, A. Danyuk, and Y. Estrin, "Deformation Mechanisms Underlying Tension–Compression Asymmetry in Magnesium Alloy ZK60 Revealed by Acoustic Emission Monitoring", *Materials Science and Engineering A*, Vol. 621, pp. 243–251, 2015.

47. Hama, T., T. Suzuki, S. Hatakeyama, H. Fujimoto, and H. Takuda, "Role of Twinning on the Stress and Strain Behaviors During Reverse Loading in Rolled Magnesium Alloy Sheets", *Materials Science and Engineering A*, Vol. 725, No. January, pp. 8–18, 2018.

48. Hama, T., N. Kitamura, and H. Takuda, “Effect of Twinning and Detwinning on Inelastic Behavior During Unloading in a Magnesium Alloy Sheet”, *Materials Science and Engineering A*, Vol. 583, pp. 232–241, 2013.

49. Hutchinson, B., J. Jain, and M. R. Barnett, “A Minimum Parameter Approach to Crystal Plasticity Modelling”, *Acta Materialia*, Vol. 60, No. 15, pp. 5391–5398, 2012.

50. Jain, A., O. Duygulu, D. W. Brown, C. N. Tomé, and S. R. Agnew, “Grain Size Effects on the Tensile Properties and Deformation Mechanisms of a Magnesium Alloy, AZ31B, Sheet”, *Materials Science and Engineering A*, Vol. 486, No. 1–2, pp. 545–555, 2008.

51. Lee, S. Y., H. Wang, M.A. Gharghouri, G. Nayyeri, W. Woo, E. Shin, P.D. Wu, W.J. Poole, W. Wu, K. An, “Deformation Behavior of Solid-Solution-Strengthened Mg–9 wt.% Al Alloy: In Situ Neutron Diffraction and Elastic–Viscoplastic Self-Consistent Modeling”, *Acta Materialia*, Vol. 73, pp. 139–148, 2014.

52. Máthis, K., G. Csiszár, J. Čapek, J. Gubicza, B. Clausen, P. Lukáš, A. Vinogradov, S.R. Agnew, “Effect of the Loading Mode on the Evolution of the deformation Mechanisms in Randomly Textured Magnesium Polycrystals – Comparison of Experimental and Modeling Results”, *International Journal of Plasticity*, Vol. 72, pp. 127–150, 2015.

53. Muránsky, O., D. G. Carr, M. R. Barnett, E. C. Oliver, and P. Šittner, “Investigation of Deformation Mechanisms Involved in the Plasticity of AZ31 Mg Alloy: In Situ Neutron Diffraction and EPSC Modelling”, *Materials Science and Engineering A*, Vol. 496, No. 1–2, pp. 14–24, 2008.

54. Qiao, H., S. R. Agnew, and P. D. Wu, “Modeling Twinning and Detwinning Behavior of Mg Alloy ZK60A During Monotonic and Cyclic Loading”, *International Journal of Plasticity*, Vol. 65, pp. 61–84, 2015.

55. Wang, H., B. Clausen, L. Capolungo, I. J. J. Beyerlein, J. Wang, and C. N. N. Tomé,

"Stress and Strain Relaxation in Magnesium AZ31 Rolled Plate: In-Situ Neutron Measurement and Elastic Viscoplastic Polycrystal Modeling", *International Journal of Plasticity*, Vol. 79, pp. 275–292, 2016.

56. Wu, W., H. Qiao, K. An, X. Guo, P. Wu, and P. K. Liaw, "Investigation of Deformation Dynamics in a Wrought Magnesium Alloy", *International Journal of Plasticity*, Vol. 62, pp. 105–120, 2014.

57. Abdolvand, H., Marta Majkut, Jette Oddershede, Søren Schmidt, Ulrich Lienert, Bradley J. Diak, Philip J. Withers, Mark R. Daymond, "On the Deformation Twinning of Mg AZ31B: A Three-Dimensional Synchrotron X-Ray Diffraction Experiment and Crystal Plasticity Finite Element Model", *International Journal of Plasticity*, Vol. 70, pp. 77–97, 2015.

58. Barnett, M. R., A. Ghaderi, J. Quinta da Fonseca, and J. D. Robson, "Influence of Orientation on Twin Nucleation and Growth at Low Strains in a Magnesium Alloy", *Acta Materialia*, Vol. 80, pp. 380–391, 2014.

59. Beyerlein, I. J. J., L. Capolungo, P. E. E. Marshall, R. J. J. McCabe, C. N. Tome, and C. N. Tomé, "Statistical Analyses of Deformation Twinning in Magnesium", *Philosophical Magazine*, Vol. 90, No. 16, pp. 2161–2190, 2010.

60. Wang, F., S. Sandlöbes, M. Diehl, L. Sharma, F. Roters, and D. Raabe, "In Situ Observation of Collective Grain-Scale Mechanics in Mg and Mg–Rare Earth Alloys", *Acta Materialia*, Vol. 80, pp. 77–93, 2014.

61. Wu, W., P. K. Liaw, and K. An, "Unraveling Cyclic Deformation Mechanisms of a Rolled Magnesium Alloy Using In Situ Neutron Diffraction", *Acta Materialia*, Vol. 85, pp. 343–353, 2015.

62. Gharghouri, M. A., G. C. Weatherly, J. D. Embury, and J. Root, "Study of the Mechanical Properties of Mg-7.7at.% Al by In-Situ Neutron Diffraction", *Philosophical Magazine A*, Vol. 79, No. 7, pp. 1671–1695, 1999.

63. Drozdenko, D., J. Bohlen, S. Yi, P. Minárik, F. Chmelík, and P. Dobroň, “Investigating a Twinning–Detwinning Process in Wrought Mg Alloys by the Acoustic Emission Technique”, *Acta Materialia*, Vol. 110, pp. 103–113, 2016.

64. Baird, J. C., S. Yazdan Parast, S.J. Horstemeyer, L.G. Hector Jr., P.T. Wang, M.F. Horstemeyer, “Localized Twin Bands in Sheet Bending of a Magnesium Alloy”, *Scripta Materialia*, Vol. 67, No. 5, pp. 471–474, 2012.

65. Ando, D., J. Koike, and Y. Sutou, “Relationship Between Deformation Twinning and Surface Step Formation in AZ31 Magnesium Alloys”, *Acta Materialia*, Vol. 58, No. 13, pp. 4316–4324, 2010.

66. Ando, D., J. Koike, and Y. Sutou, “The Role of Deformation Twinning in the Fracture Behavior and Mechanism of Basal Textured Magnesium Alloys”, *Materials Science and Engineering A*, Vol. 600, pp. 145–152, 2014.

67. Sun, D. K., C. P. Chang, and P. W. Kao, “Microstructural Study of Strain Localization in Hot Compressed Mg-3Al-1Zn Alloy”, *Materials Science and Engineering A*, Vol. 527, No. 26, pp. 7050–7056, 2010.

68. Koike, J., N. Fujiyama, D. Ando, and Y. Sutou, “Roles of Deformation Twinning and Dislocation Slip in the Fatigue Failure Mechanism of AZ31 Mg Alloys”, *Scripta Materialia*, Vol. 63, No. 7, pp. 747–750, 2010.

69. Lv, F., F. Yang, Q.Q. Duan, Y.S. Yang, S.D. Wu, S.X. Li, Z.F. Zhang, “Fatigue Properties of Rolled Magnesium Alloy (AZ31) Sheet: Influence of Specimen Orientation”, *Int. J. Fatigue*, Vol. 33, No. 5, pp. 672–682, 2011.

70. Kapan, E., N. Shafaghi, S. Uçar, and C. C. Aydiner, “Strain Localization Structures in Textured Magnesium AZ31 Under Reversed Loading via Microscopic Digital Image Correlation”, *TMS 2017 146th Annual Meeting & Exhibition Supplemental Proceedings*, San Diego, California, pp. 183–190, 2017.

71. Martin, G., C. W. Sinclair, and J. H. Schmitt, “Plastic Strain Heterogeneities in an Mg-1Zn-0.5Nd Alloy”, *Scripta Materialia*, Vol. 68, No. 9, pp. 695–698, 2013.

72. Chen, Z., W. Lenthe, J. C. Stinville, M. Echlin, T. M. Pollock, and S. Daly, “High-Resolution Deformation Mapping Across Large Fields of View Using Scanning Electron Microscopy and Digital Image Correlation”, *Experimental Mechanics*, Vol. 58, No. 9, pp. 1407–1421, 2018.

73. Barnett, M. R. and N. Stanford, “Influence of Microstructure on Strain Distribution in Mg–3Al–1Zn”, *Scripta Materialia*, Vol. 57, No. 12, pp. 1125–1128, 2007.

74. Sandlöbes, S., S. Zaefferer, I. Schestakow, S. Yi, and R. Gonzalez-Martinez, “On the Role of Non-Basal Deformation Mechanisms for the Ductility of Mg and Mg-Y Alloys”, *Acta Materialia*, Vol. 59, No. 2, pp. 429–439, 2011.

75. Wu, Y. J., R. Zhu, J. T. Wang, and W. Q. Ji, “Role of Twinning and Slip in Cyclic Deformation of Extruded Mg-3%Al-1%Zn Alloys”, *Scripta Materialia*, Vol. 63, No. 11, pp. 1077–1080, 2010.

76. Park, S. H., S. G. Hong, W. Bang, and C. S. Lee, “Effect of Anisotropy on the Low-Cycle Fatigue Behavior of Rolled AZ31 Magnesium Alloy”, *Materials Science and Engineering A*, Vol. 527, No. 3, pp. 417–423, 2010.

77. a Curtin, W. and R. E. Miller, “Atomistic / Continuum Coupling in Computational Materials Science”, *Modelling and Simulation in Materials Science and Engineering*, Vol. 11, pp. R33–R68, 2003.

78. Suquet, P. and N. Lahellec, “Elasto-Plasticity of Heterogeneous Materials at Different Scales”, *Procedia IUTAM*, Vol. 10, pp. 247–262, 2014.

79. Roters, F., P. Eisenlohr, L. Hantcherli, D. D. Tjahjanto, T. R. Bieler, and D. Raabe, “Overview of Constitutive Laws, Kinematics, Homogenization and Multiscale

Methods in Crystal Plasticity Finite-Element Modeling: Theory, Experiments, Applications", *Acta Materialia*, Vol. 58, No. 4, pp. 1152–1211, 2010.

80. Wang, H., P. D. Wu, J. Wang, and C. N. Tomé, "A Crystal Plasticity Model for Hexagonal Close Packed (HCP) Crystals Including Twinning and De-Twinning Mechanisms", *International Journal of Plasticity*, Vol. 49, pp. 36–52, 2013.

81. Beyerlein, I. J. J., R. J. J. McCabe, and C. N. N. Tomé, "Effect of Microstructure on the Nucleation of Deformation Twins in Polycrystalline High-Purity Magnesium: A Multi-Scale Modeling Study", *Journal of the Mechanics and Physics of Solids*, Vol. 59, No. 5, pp. 988–1003, 2011.

82. Niezgoda, S. R., A. K. Kanjarla, I. J. Beyerlein, and C. N. Tomé, "Stochastic Modeling of Twin Nucleation in Polycrystals: An Application in Hexagonal Close-Packed Metals", *International Journal of Plasticity*, Vol. 56, pp. 119–138, 2014.

83. Mareau, C. and M. R. Daymond, "Micromechanical Modelling of Twinning in Polycrystalline Materials: Application to Magnesium", *International Journal of Plasticity*, Vol. 85, pp. 156–171, 2016.

84. Shafaghi, N., E. Kapan, and C. C. Aydıner, "Cyclic Strain Heterogeneity and Damage Formation in Rolled Magnesium Via In Situ Microscopic Image Correlation", *Experimental Mechanics*, Vol. 60, No. 6, pp. 735–751, 2020.

85. Eisenlohr, P., M. Diehl, R. A. Lebensohn, and F. Roters, "A Spectral Method Solution to Crystal Elasto-Viscoplasticity at Finite Strains", *International Journal of Plasticity*, Vol. 46, pp. 37–53, 2013.

86. Willot, F., "Fourier-Based Schemes for Computing the Mechanical Response of Composites with Accurate Local Fields", *Comptes Rendus Mécanique*, Vol. 343, No. 3, pp. 232–245, 2015.

87. Kalidindi, R., "Incorporation of Deformation Twinning in Crystal Plasticity Models",

Journal of the Mechanics and Physics of Solids, Vol. 46, No. 2, 1998.

88. Wang, Y., Y. Xin, H. Yu, L. Lv, and Q. Liu, "Formation and Microstructure of Shear Bands During Hot Rolling of a Mg-6Zn-0.5Zr alloy Plate with a Basal Texture", *Journal of Alloys and Compounds*, Vol. 644, pp. 147–154, 2015.

89. Yim, C. D., Y. M. Seo, and B. S. You, "Effect of the Reduction Ratio Per Pass on the Microstructure of a Hot-Rolled AZ31 Magnesium Alloy Sheet", *Metals and Materials Internationa*, Vol. 15, No. 4, pp. 683–688, 2009.

90. Kaibyshev, R., "Dynamic Recrystallization in Magnesium Alloys", *Advances in Wrought Magnesium Alloys*, Woodhead Publishing, Sawston, United Kingdom, pp. 186–225, 2012.

91. Bach, F.-W., M. Rodman, A. Rossberg, B.-A. Behrens, and G. Kurzare, "Macroscopic Damage by the Formation of Shear Bands During the Rolling and Deep Drawing of Magnesium Sheets", *The Journal of the Minerals, Metals & Materials Society*, Vol. 57, No. 5, pp. 57–61, 2005.

92. Bohlen, J., M. R. Nürnberg, J. W. Senn, D. Letzig, and S. R. Agnew, "The Texture and Anisotropy of Magnesium–Zinc–Rare Earth Alloy Sheets", *Acta Materialia*, Vol. 55, No. 6, pp. 2101–2112, 2007.

93. Arul Kumar, M., A. K. Kanjarla, S. R. Niezgoda, R. A. Lebensohn, and C. N. Tomé, "Numerical Study of the Stress State of a Deformation Twin in Magnesium", *Acta Materialia*, Vol. 84, pp. 349–358, 2015.

94. Muránsky, O., D. G. Carr, P. Šittner, and E. C. Oliver, "In Situ Neutron Diffraction Investigation of Deformation Twinning and Pseudoelastic-Like Behaviour of Extruded AZ31 Magnesium Alloy", *International Journal of Plasticity*, Vol. 25, No. 6, pp. 1107–1127, 2009.

95. Wu, L., S.R. Agnew, D.W. Brown, G.M. Stoica, B. Clausen, A. Jain, D.E. Fielden,

P.K. Liaw, “Internal Stress Relaxation and Load Redistribution During the Twinning–Detwinning-Dominated Cyclic Deformation of a Wrought Magnesium Alloy, ZK60A”, *Acta Materialia*, Vol. 56, No. 14, pp. 3699–3707, 2008.

96. Van Rooyen, G., “Basic Factors Which Influence the Lüders Strain During Discontinuous Yielding”, *Materials Science and Engineering*, Vol. 7, No. 1, pp. 37–48, 1971.

97. Jain, A. and S. R. Agnew, “Modeling the Temperature Dependent Effect of Twinning on the Behavior of Magnesium Alloy AZ31B Sheet”, *Materials Science and Engineering A*, Vol. 462, No. 1–2, pp. 29–36, 2007.

98. Couling, S. L. L., J. F. F. Pashak, and L. Sturkey, “Unique Deformation and Aging Characteristics of Certain Magnesium-Base Alloys”, *Transactions of American Society for Metals*, Vol. 51. pp. 94–107, 1959.

99. Ion, S. E., F. J. Humphreys, and S. H. White, “Dynamic Recrystallisation and the Development of Microstructure During the High Temperature Deformation of Magnesium”, *Acta Metallurgica*, Vol. 30, No. 10, pp. 1909–1919, 1982.

100. Barnett, M. R., “The Challenge of Inhomogeneous Deformation in Mg and Its Alloys”, *Matererial Science Forum*, Vol. 618–619, pp. 227–232, 2009.

101. Echlin, M. P., J. C. Stinville, V. M. Miller, W. C. Lenthe, and T. M. Pollock, “Incipient Slip and Long Range Plastic Strain Localization In Microtextured Ti-6Al-4V titanium”, *Acta Materialia*, Vol. 114, pp. 164–175, 2016.

102. Kasemer, M., M. P. Echlin, J. C. Stinville, T. M. Pollock, and P. Dawson, “On Slip Initiation in Equiaxed α / β Ti-6Al-4V”, *Acta Materialia*, Vol. 136, pp. 288–302, 2017.

103. Graff, S., W. Brocks, and D. Steglich, “Yielding of Magnesium: From Single Crystal to Polycrystalline Aggregates”, *International Journal of Plasticity*, Vol. 23, No. 12, pp. 1957–1978, 2007.

APPENDIX

A.1. Single Crystal Runs on CPFE Software.

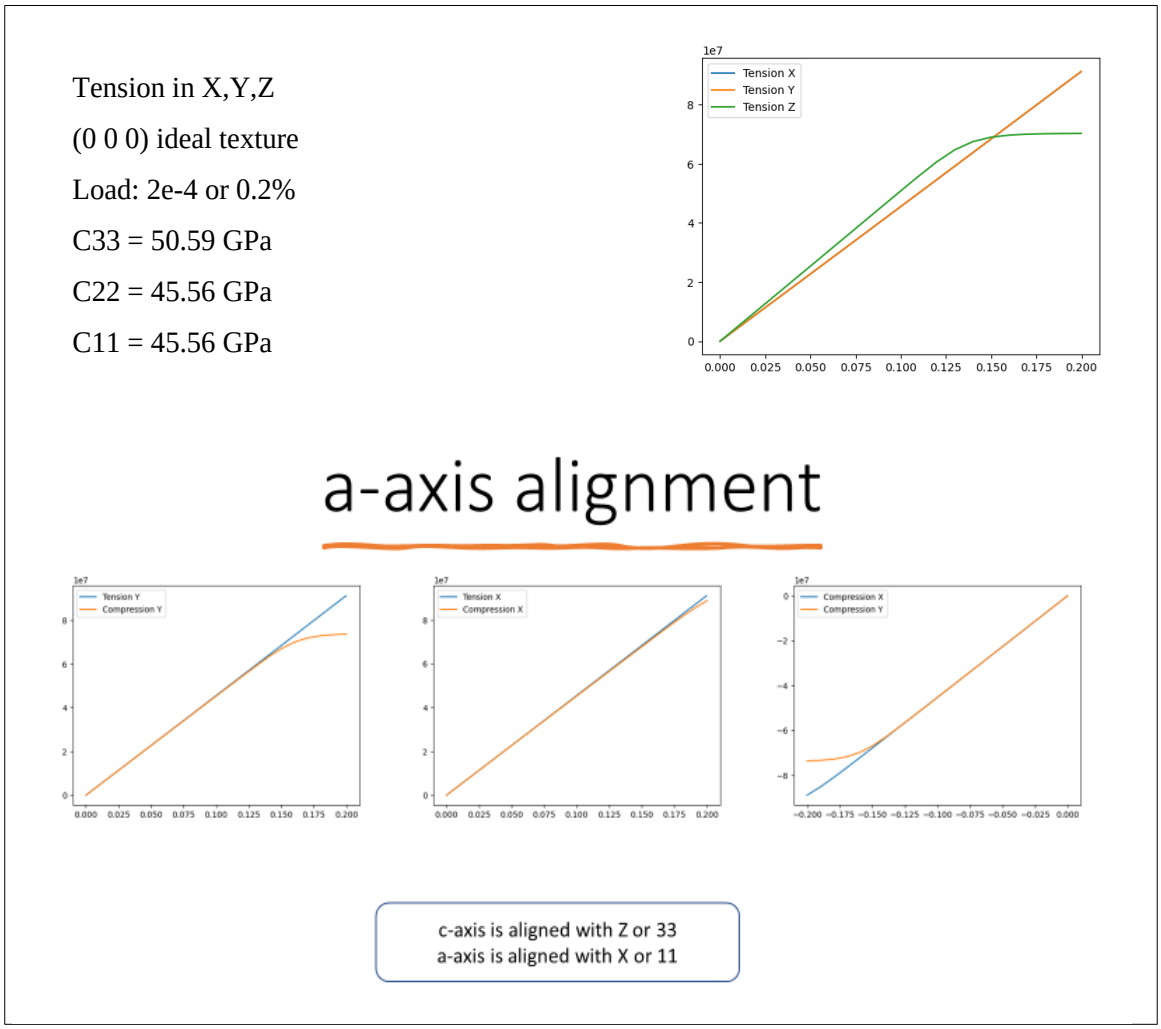

Figure A.1. Determination of DAMASK coordinate system (correlation of DAMASK coordinate directions compared to HCP crystal axes for ideal rolled texture with all crystals c-axis || ND).

A.2. Configuration and Loadcase Files Used in DAMASK

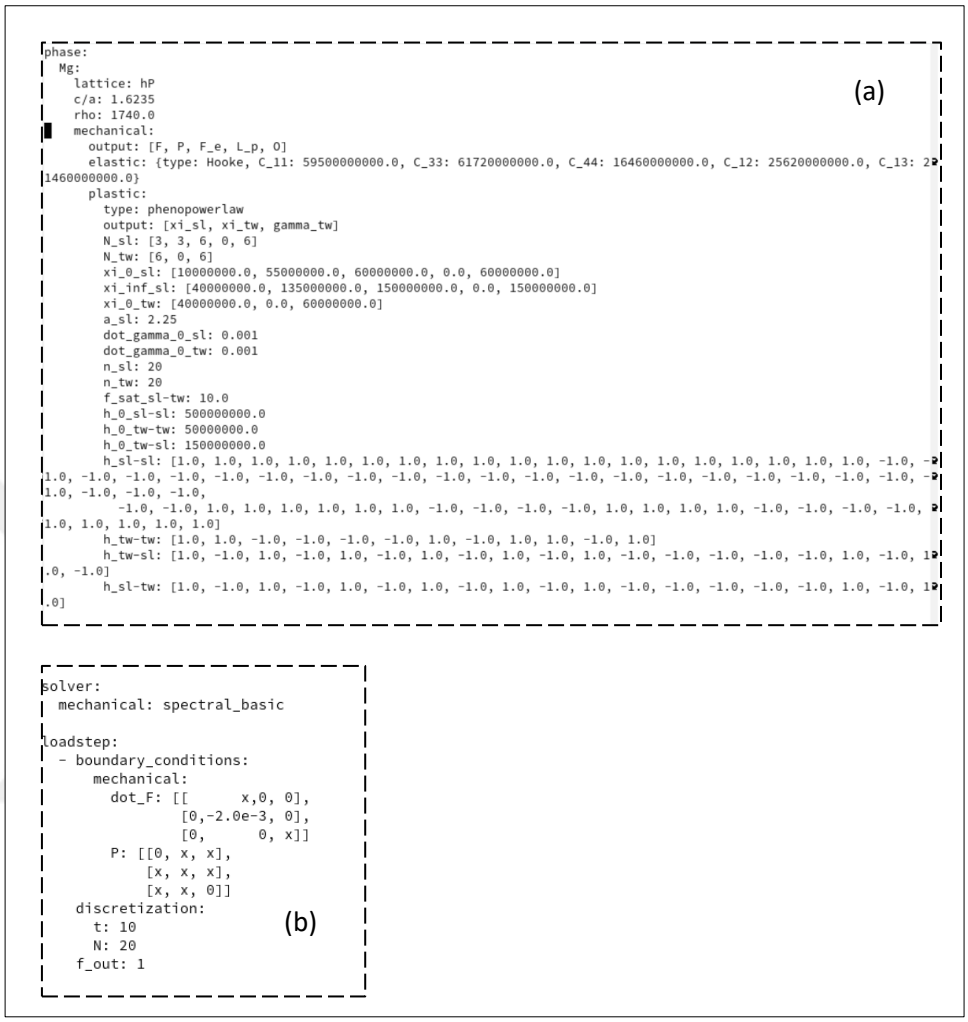

Figure A.2. (a) configuration file example and (b) loadcase definition for 2% compression along y direction.

A.3. Parameter Sensitivity in Cyclic Load.

Parameter/iteration	S0 basal	S0 prism	S0 pyramid (a)	S0 pyramid(c+a)	S_inf basal	S_inf prism	S_inf pyramid (a)	S_inf pyramid(c+a)
1	5000000.0	55000000.0	60000000.0	60000000.0	40000000.0	135000000.0	150000000.0	150000000.0
2	200000000.0	55000000.0	60000000.0	60000000.0	40000000.0	135000000.0	150000000.0	150000000.0
3	10000000.0	20000000.0	60000000.0	60000000.0	40000000.0	135000000.0	150000000.0	150000000.0
4	10000000.0	70000000.0	60000000.0	60000000.0	40000000.0	135000000.0	150000000.0	150000000.0
5	10000000.0	55000000.0	60000000.0	60000000.0	20000000.0	135000000.0	150000000.0	150000000.0

Parameter/iteration	S0 twin	S0 twin
6	20000000.0	60000000.0
7	80000000.0	60000000.0

Parameter/iteration	h0, sl-sl	h0, twintwin	h0, twinslip
8	250000000.0	50000000.0	150000000.0
9	800000000.0	50000000.0	150000000.0
10	500000000.0	25000000.0	150000000.0
11	500000000.0	100000000.0	150000000.0
12	500000000.0	50000000.0	75000000.0

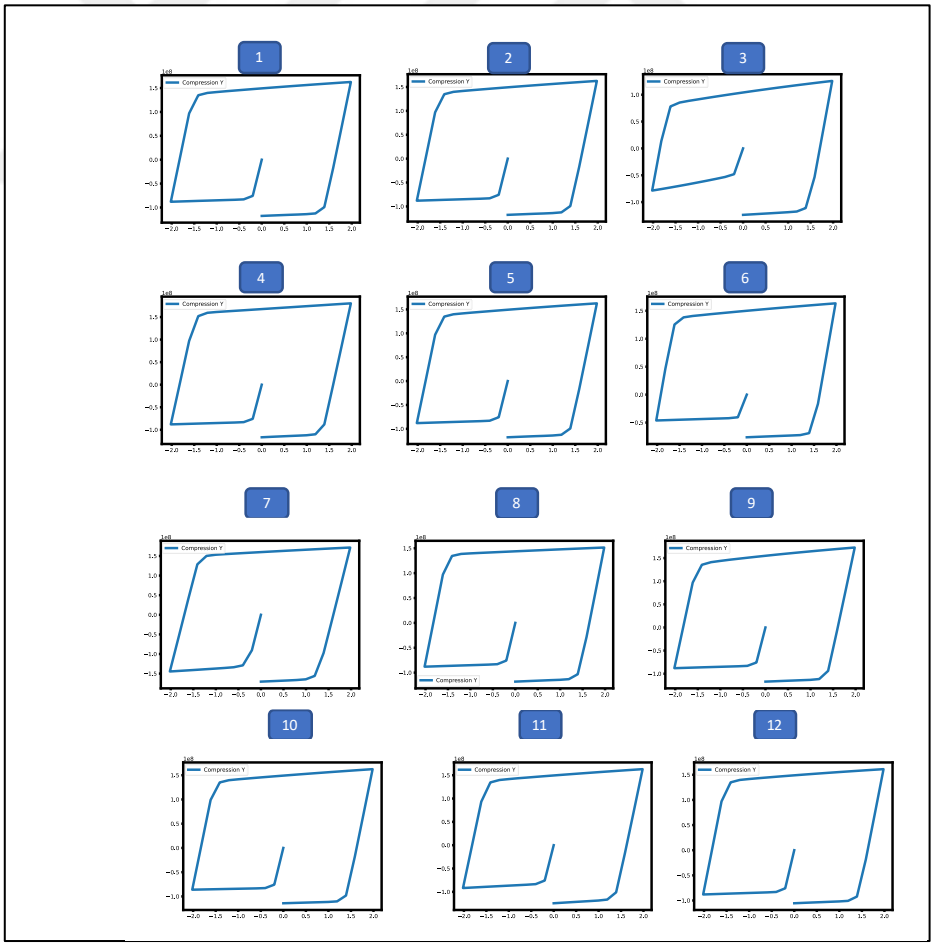

Figure A.3. Parameter sensitivity study on ideal rolled texture under cyclic load.

A.4. Pre-Process Script (Run in Jupyter-Lab).

```
seeds = damask.seeds.from_random([0.99e-4,1.98e-4,0.11e-4],162)

g = damask.Grid.from_Voronoi_tessellation(np.array([128,256,14]),np.array([0.99e-4,1.98e-4,0.11e-4]),seeds)

g.save('162grains128x256x14.vti')


config_material= damask.ConfigMaterial()

config_material['homogenization']['dummy'] = {'N_constituents':1, 'mechanical':{'type':'pass'}}

config_material['phase']['Mg']  = damask.ConfigMaterial.load('material_phase_phenopowerlaw.yaml')

A = np.array([array of three Bunge orientations ϕ1, ϕ, ϕ2])

weights = np.array([weight of each set of orientations])


O_Mg = damask.Rotation.from_ODF(weights,A, shape=162, degrees=True)


config_material = config_material.material_add(homogenization='dummy', phase='Mg', O=O_Mg)

config_material.save()


run the simulation

DAMASK_grid –geom '162grains128x256x14.vti' –load compression.yaml


Post Process

import damask

result_file = '162grains128x256x14_compressionY.hdf5'

r = damask.Result(result_file)

r.add_stress_Cauchy()

r.add_strain()

r.export_VTK()
```

Figure 6.4. Scripts used to create configuration file, run the simulation and post-process the results.

A.5. IPF Representation

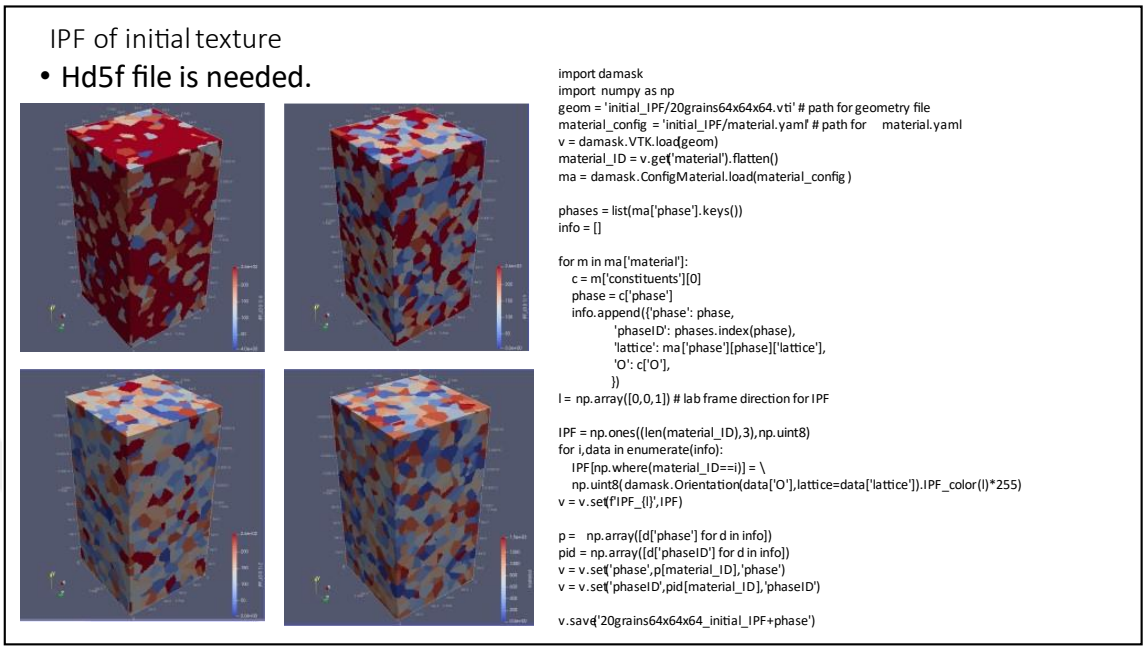

Figure A.5. Creating IPF results in DAMASK. Results are visualized in ParaViwe.

A.6. Copyright Details

The images that emerged within the scope of this thesis work and whose copyrights were transferred to the publishing house were used in this thesis in accordance with the "valid publishing policy for the reuse of the text and graphics produced by the author" on the website of the publisher. All figures, tables and sketches are either taken from the published journal paper of the same author of this thesis (Shafaghi et al., 2020) or created by the author himself.